Title
Metamaterial composites with tunable electromagnetic properties

Permalink
https://escholarship.org/uc/item/0w51q0mk

Author
Wheeland, Sara Ruth

Publication Date
2013

Peer reviewed|Thesis/dissertation

UNIVERSITY OF CALIFORNIA, SAN DIEGO

Metamaterial Composites with Tunable Electromagnetic Properties

A dissertation submitted in partial satisfaction of the requirements for the degree

Doctor of Philosophy

in

Engineering Sciences (Mechanical Engineering)

by

Sara Ruth Wheeland

Committee in charge:

> Sia Nemat-Nasser, Chair
> Alireza V. Amirkhizi
> Prabhakar Bandaru
> Hyonny Kim
> Xanthippi Markenscoff
> Daniel Sievenpiper

2013

The Dissertation of Sara Ruth Wheeland is approved, and it is acceptable in quality and form for publication on microfilm and electronically:

_____

_____

_____

_____

_____
Chair

University of California, San Diego

2013

DEDICATION

To my daughter Anja;

To my son Oliver;

To my husband Cody;

To my family and friends;

This dissertation is for you.

Thank you all for your love and support.

Man's mind stretched
to a new idea
never goes back
to its original dimensions.

Oliver Wendell Holmes

TABLE OF CONTENTS

LIST OF ABBREVIATIONS

BFGS	Broyden-Fletcher-Goldfarb-Shanno numerical method
CEAM	Center of Excellence for Advanced Materials
EM	Electromagnetic
GRIN	Gradient index
GUI	Graphic user interface
HFSS	High Frequency Structural Simulator
MEMS	Microelectromechanical systems
PCB	Printed circuit board
PDMS	Polydimethylsiloxane
PML	Perfectly matched layer
PTFE	Polytetrafluoroethylene
RF	Radio frequency
SRR	Split-ring resonators
TE	Transverse electric
TM	Transverse magnetic
TR	Transmit/reflect
TRL	Thru, reflect, line
VNA	Vector Network Analyzer

LIST OF FIGURES

LIST OF TABLES

ACKNOWLEDGEMENT

2007   Bachelor of Science in Mechanical Engineering, Franklin W. Olin College of Engineering, Needham, MA

2009   Master of Science in Engineering Sciences, Mechanical Engineering, University of California, San Diego

2013   Doctor of Philosophy in Engineering Sciences, Mechanical Engineering, University of California, San Diego

PUBLICATIONS

JOURNAL ARTICLES

Wheeland, S., A.V. Amirkhizi, and S. Nemat-Nasser. 2012. Soft-focusing in anisotropic indefinite media through hyperbolic dispersion. *Progress in Electromagnetics Research.* **132**: 389-402.

Wheeland, S., F. Bayatpur, A.V. Amirkhizi, and S. Nemat-Nasser. 2013. Elastomeric composites with tuned electromagnetic characteristics. *Smart Materials and Structures.* **22** 015006.

Bayatpur, F., S. Wheeland, A.V. Amirkhizi, and S. Nemat-Nasser. 2013. A varactor-tuned helix-based chiral layer. *IEEE Microwave and Wireless Components Letters.* (submitted for publication)

PROCEEDINGS

Wheeland, S., F. Bayatpur, A.V. Amirkhizi, S. Nemat-Nasser. 2011. Chiral braided and woven composites: design, fabrication and electromagnetic characterization. *Proceedings of SPIE Smart Structures and Materials & Nondestructive Evaluation and Health Monitoring, 18th Annual International Symposium.* **7978**: 797812.

Wheeland, S., A.V. Amirkhizi, and S. Nemat-Nasser. 2010. Mechanically-tunable composite filter at low frequencies. *Proceedings of SPIE Smart Structures and Materials & Nondestructive Evaluation and Health Monitoring, 17th Annual International Symposium.* **7644**: 76441N.

Marshall, S., A.V. Amirkhizi, and S. Nemat-Nasser. 2009. Focusing and negative refraction in anisotropic indefinite permittivity media. *Proceedings of SPIE Smart Structures and Materials & Nondestructive Evaluation and Health Monitoring, 16th Annual International Symposium.* **7287**: 72870.

ABSTRACTS

Wheeland, S., A.V. Amirkhizi, and S. Nemat-Nasser. 2012. Microwave gradient index lens design with mechanically tunable permittivity. *Proceedings of the ASME 2012 International Mechanical Engineering Congress & Exposition.*

FIELDS OF STUDY

Major Field: Engineering Sciences (Mechanical Engineering)

        Studies in Mechanical and Electromagnetic Behavior of Materials
        Professor Sia Nemat-Nasser

ABSTRACT OF THE DISSERTATION

Metamaterial Composites with Tunable Electromagnetic Properties

by

Sara Ruth Wheeland

Doctor of Philosophy in Engineering Sciences (Mechanical Engineering)

University of California, San Diego, 2013

Professor Sia Nemat-Nasser, Chair

A broadening application range has increased demand for advanced RF control. Recent research has identified several metamaterials to provide this control. This work seeks to expand this idea through several novel metamaterials with enhanced electromagnetic properties. First copper wires braided with Kevlar and nylon to form conductive coils are woven among structural fiber to create a fabric. This yielded a composite with all coils possessing the same handedness, producing a chiral material. The measured scattering parameters showed considerable chirality within the 5.5-8GHz frequency band, agreeing with simulation results.

Electronic chirality tuning is investigated by integrating varactor diodes into an array of helical elements on a printed circuit board. Applying a varied reverse bias voltage across the sample effectively tunes the chiral behavior of the material. The measurements demonstrate the feasibility of creating a rigid helix composite with tuned chirality in the 5.5-12.4GHz frequency band.

Chirality can be further tuned mechanically through the deformation of an array of conductive coils. Parallel, metallic helices embedded in a polyurethane matrix are subjected to mechanical stretching for pitch adjustment. This change in pitch directly affects the overall chirality of the composite. Repeatable elastic deformation is achieved up to 50% axial strain. Over the 5.5-12.5GHz frequency range, an increase of 30% axial strain yields an ~18% change in axial chirality.

Hyperbolic microwave focusing is explored through an indefinite medium with anisotropic permittivity. An array of 12-gauge brass wires is embedded in Styrofoam and scanned over the 7-9GHz frequency band to establish focusing patterns. A soft-focusing spot is observed at 7.6GHz with a relative gain of ~7dB over averaged background.

Applying an axial refractive gradient to a coil composite creates a lens capable of fine adjustment in the microwave range. The gradient required to achieve sharp focusing, and the extent of this effect, is calculated through an anisotropic ray-tracing analysis. A composite is created using coils of opposite handedness to minimize chiral effects. Through extension of these coils, the refractive index can effectively be fine-tuned to achieve the desired result. Measurements and full-wave simulations confirm a gain of 6-8dB over averaged background at the predicted focal frequencies.

Chapter 1

Introduction

1.1 Motivation and Background

There are a growing number of applications that make use of the C and X bands of the radio spectrum (4-12GHz). These applications range from advanced high-resolution radar systems to satellite communications to commercial terrestrial networks. With the expanding usage of this frequency range, demand exists for more control of the radio frequency (RF) signals. For instance, frequency can be controlled through filtering, polarization can be controlled by the chirality of a material, and strength can be controlled by focusing the signal. Recent research has identified several types of metamaterials that can be used to provide this control, including negative index materials, indefinite media, and chiral media. This research attempts to extend the functionality of these materials in three ways: by making the materials structural, by allowing for easier manufacture and by enabling mechanical or electrical tuning of the properties.

The integration of copper wire into a structure induces an electromagnetic response in the material. An array of straight wires acts as a high pass filter at microwave frequencies. At a certain frequency the electric permittivity, which quantifies the ease with which a material transmits electric flux, is equal to zero. Such a frequency is termed the plasmon, or turn-on, frequency f_p. Below this frequency, the permittivity is negative. As a result, EM waves are reflected at the surface of the medium. Above this frequency, the permittivity becomes positive and the material becomes transparent to incident waves. The turn-on frequency can be adjusted via the geometry of the array. Such a phenomenon is useful for filters in which the transmission of higher frequencies is desired.

Negative refraction is traditionally achieved through negative index materials. Negative index, or left-handed, media typically consist of complex microstructures. If the permittivity tensor contains elements of opposite sign, the medium is considered indefinite. An indefinite material yields negative refraction through the structure due to anisotropy. Such anisotropic behavior facilitates the fabrication of negative refraction metamaterials by simplifying the microstructure of the material.

By introducing an array of coils instead of straight wires, the permittivity of the composite can be tuned via mechanical strain. Rather than fabricating several samples with different properties, one sample can be fabricated and tuned accordingly to achieve the desired effect. This extends the use of the sample to multiple applications. Controlling the permittivity in this manner also controls higher-level properties, such as the plasmon frequency mentioned above and the chirality discussed below.

Chirality exists when the coils within the array share the same handedness. This couples the electric and magnetic field components. For a generalized medium, the electric flux density $\boldsymbol{D}$ and the magnetic flux density $\boldsymbol{B}$ have the following form:

$$\boldsymbol{D} = \varepsilon_0 \boldsymbol{\varepsilon} \cdot \boldsymbol{E} + \boldsymbol{\xi} \cdot \boldsymbol{H} \qquad (1.5)$$

$$\boldsymbol{B} = \mu_0 \boldsymbol{\mu} \cdot \boldsymbol{H} + \boldsymbol{\zeta} \cdot \boldsymbol{E} \qquad (1.6)$$

where $\boldsymbol{\varepsilon}$ and $\boldsymbol{\mu}$ denote relative electric permittivity and magnetic permeability, respectively, and ε_0 and μ_0 denote the permittivity and permeability of free space. Electric polarization $\boldsymbol{\xi}$ and magnetic polarization $\boldsymbol{\zeta}$ couple the electric and magnetic fields in a chiral material. In non-chiral media, $\boldsymbol{\xi}$ and $\boldsymbol{\zeta}$ equal zero since the fields are uncoupled in a linear material. This coupling allows for more control of the material properties. As a plane wave propagates through a chiral medium, left- and right-circularly polarized waves are absorbed differently and the polarization of the wave rotates

according to the strength of the coupling. Through mechanical strain of the coil array, chirality can be tuned to achieve the desired effect.

One can also tune the chirality electrically through the use of varactors. Varactor diodes behave as capacitors when reverse-biased, with the capacitance dependent on the reverse bias voltage. These diodes are placed between adjacent helical elements of same handedness on a printed circuit board (PCB). By varying the capacitance of the varactors the chirality can be precisely controlled.

The work presented here investigates each of the above characteristics through the use of metamaterial composites. The ultimate objective is to create a multifunctional material that can be tuned to filter unwanted frequencies while simultaneously focusing desired frequencies using a flat lens with a gradient index of refraction $n = \sqrt{\varepsilon\mu}$. This lens can then be mechanically tuned as necessary depending on the application. Though not presented in this work, such a material could also include mechanically tunable chiral behavior with the addition of coils of the same handedness. This behavior could be enhanced and electrically tuned with the use of varactors between coils. Further investigation in this area is necessary.

The electromagnetic response present in each of the presented experiments is measured through the use of scattering, or S-, parameters. Each S-parameter is a ratio of the transmitted and received power of the waves. For a two-port measurement system, the scattering matrix consists of four parameters: S_{11}, S_{12}, S_{21}, and S_{22}. The first subscript denotes the receiving port, and the second subscript denotes the transmitting port. Therefore, S_{11} represents the ratio of the reflected power sent from and received at port 1, whereas S_{12} represents the ratio of the transmitted power sent from port 2 and received at port 1.

1.2   Structure of the Dissertation

Most of the chapters in this dissertation are designed to stand alone. As a result, some fundamental concepts are repeated for clarity. Chapter 2 investigates the chiral behavior of a Kevlar-copper wire composite. Kevlar and nylon fibers are braided with a strand of copper wire then woven with plain Kevlar fiber to create a 2D fabric that exhibits chirality. Chapter 3 explores the electronic tunability of chirality. Varactor diodes are incorporated into an array of rectangular helices of same handedness printed on a circuit board. The resulting composite exhibits chirality that can be tuned by varying the input voltage.

Chapter 4 presents a material consisting of copper coils of same handedness embedded in a polyurethane matrix. The elastomer provides a means to mechanically tune both the chirality and the plasmon frequency of the composite. Chapter 5 investigates the focusing effect of hyperbolic dispersion exhibited in a Styrofoam-wire composite. An array of thin straight wires is incorporated into a block of Styrofoam to create a medium with an indefinite permittivity tensor. The resulting material softly focuses incident microwaves at a specific frequency.

This dissertation culminates in Chapter 6 with a composite that combines concepts from the previous chapters. An array of alternate-handedness beryllium copper coils with a specific pitch gradient is placed within a wooden frame. The pitch gradient corresponds to a permittivity gradient within the composite, which more strongly focuses incident plane waves. The non-chiral material can be stretched to mechanically adjust its permittivity, thus creating a GRIN lens that can be tuned to focus at different frequencies.

Chapter 2

Braided and Woven Chiral Composites

2.1 Introduction

Composites made from braided and woven fibers have received a great deal of attention due to their superior mechanical properties over traditional laminates. Such materials have found use in a variety of industries, including aerospace and automobiles[1]. Numerical models have been conducted on these composites using numerous techniques[1-4]. Experimental work characterized various configurations of both 2D and 3D woven fabric[5,6]. These studies have demonstrated the mechanical strength and complexity of this type of composite.

This work seeks to extend the functionality of braided and woven composites beyond purely structural strength. By integrating conductive coils into the structure, the fabric possesses both mechanical and electromagnetic properties. One way to achieve this is to introduce a copper wire during the braiding process. The completed braid then contains a non-magnetic conductive coil along with structural fiber.

If the coils are aligned with the same handedness, the fabric exhibits chirality. The extent of this effect can be determined by measuring the scattering, or S-, parameters of the composite. Each of these S-parameters is a ratio between the incident and the reflected waves. The first subscript represents the reflected wave, while the second subscript represents the incident wave. S_{21}, therefore, is the ratio between the reflected signal at port 2 and the incident signal at port 1. Using the axial transmission, S_{21}, along the axis of the material and the cross-polarization transmission, $S_{21\text{-}yz}$, between the axial and normal transmissions, a polarization contour can be

created and projected onto a rectangular plane. The shape and characteristics of this contour reflect the amount of chirality present in the material.

This study presents a braided and woven composite with chirality. Scattering parameters were predicted with a full-wave finite element simulation using Ansoft HFSS and experimentally verified in free space. The results from both the model and the experiments indicate the feasibility of creating a woven composite that exhibits strong chirality.

2.2 Materials

2.2.1 Sample Materials

Each woven fabric sample consisted of braids as the warp component and plain aromatic polyamide, or aramid, fibers (DuPont Kevlar) as the weft component. For the preliminary study, 200 denier and 1140 denier Kevlar fibers were used in conjunction with 210 denier nylon 6,6 fiber. One braid consisted of three strands of 200 denier Kevlar, two strands of 210 denier nylon 6,6 fiber, and one 30-gauge copper wire braided around a core of 6 strands of the nylon. The second braid comprised five strands of 1140 denier Kevlar fiber and one 28-gauge copper wire.

2.2.2 Sample Preparation

2.2.2.1 Braids

In each case of the preliminary study, a braider with six carriages was used to construct the braids. The braider operates in a maypole fashion with each carriage following a specific path around the center mandrel. This allows the strands to weave in and out of each other and, if desired, around a fiber core. This produces a basic two-under-two-over braid. A spool attached to

a wheel at the top of the machine collects the braid as it is completed. This process, illustrated in

Figure 2.1, produces a spool of right-handed coils integrated into a complex braid.
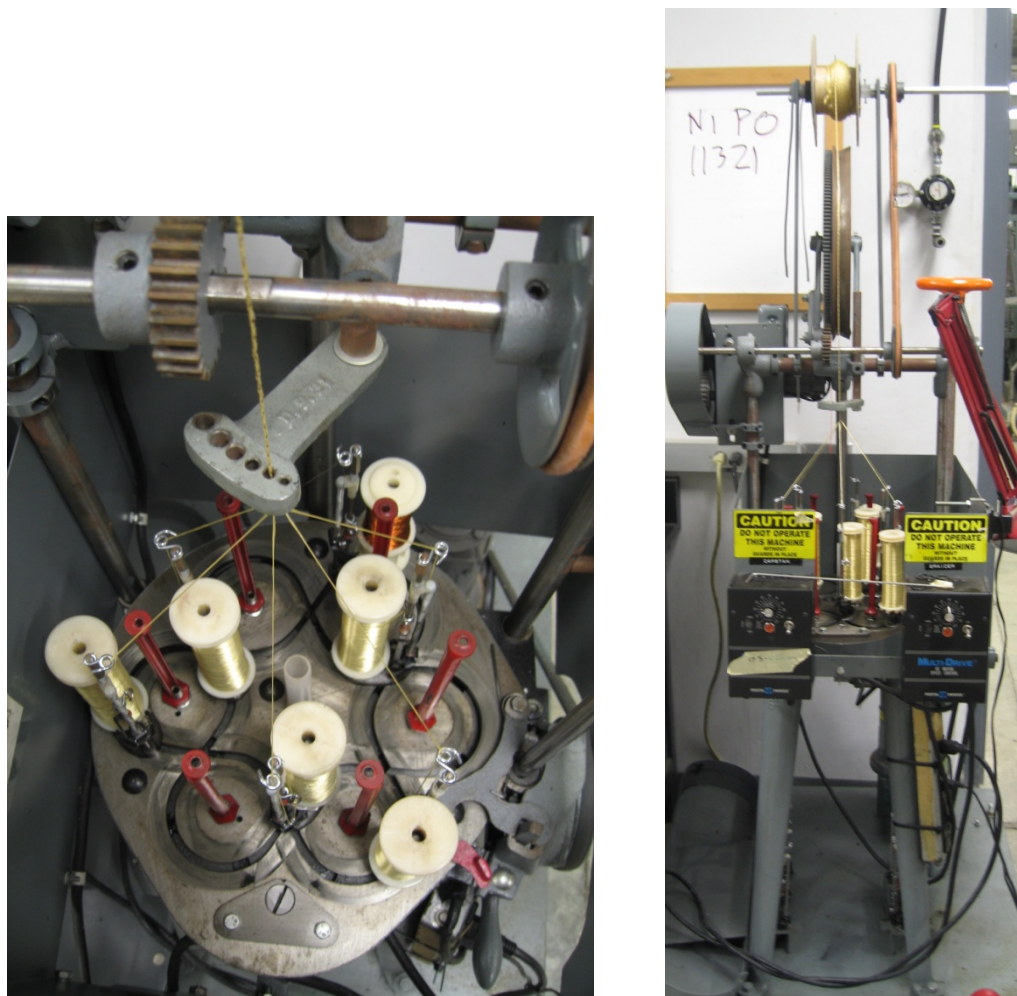
Figure 2.1: Images of the maypole braider showing the tow configuration (left) and the placement of the spool (right)

For the current study, Kevlar fiber was wound onto each of either three or five carriages

so that an equal amount was on each. Copper wire of either 30- or 28-gauge, respectively, was

wound onto one carriage. For the first braid, nylon 6,6 fiber was wound onto two carriages. Six

strands were thread through the center of the braider to make the core of the braid. The carriages

were then placed into the tracks of the machine. Each strand was pulled through the top hole and

knotted together to facilitate braid initiation. This knot was then attached to the braid-collecting spool. Once the braider started, carriage and feed speeds were adjusted to achieve the desired pitch and tightness of braid. Each braid was initially monitored to ensure that the tension in the system would allow the spool to collect the finished braid. Once the whole braid was completed and collected, the spool was removed from the system and an empty spool was inserted.

2.2.2.2 Fabric

Once complete, the braid on the spool was taken from the braider and woven with 1140 denier Kevlar fiber into a fabric. This involved several steps to ensure a consistent composite. First, the braid was wound around a warp board, reversing direction along the same path with each turn. By tying various mid-sections of this warp together, movement of the braids was restricted. This provided a means for organizing the braids and facilitating near identical lengths of braid once the ends were cut.

Second, the warp was worked onto the loom for weaving. One set of the cut braid ends was tied to the back of a Woolhouse Tools Air-Loom. The free ends were then threaded through the heddles, alternating between 1st row and 2nd row heddles in order to create the basic 2D weave pattern. Ends were threaded through the comb and attached to the front of the loom in groups of about 10, adjusting each group so that the entire width had similar tension to produce a more uniform fabric.

With the braids on the loom, the final fabric sample was created. Plain cotton yarn was woven through the warp initially to achieve proper and consistent spacing. Plain 1140 denier Kevlar weft was woven through the entire length of the warp to produce a single length of fabric. Once the front apron bar could no longer advance, the back section of remaining warp was cut

and the completed fabric was removed from the loom. A completed fabric sample is shown in Figure 2.2.
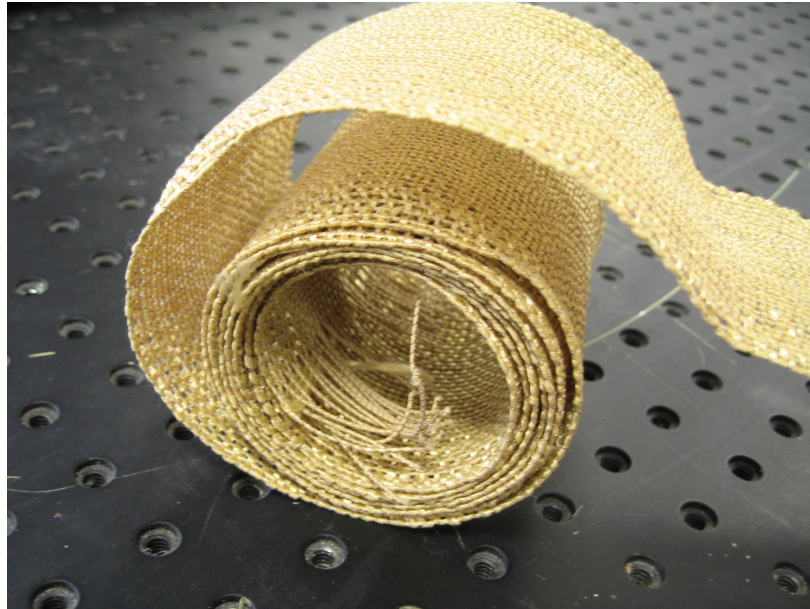
Figure 2.2: Woven fabric with 2mm pitch braids

2.3 Experiments

2.3.1 Sample Specifications

For the experiment, the fabric with braids containing nylon fiber was used. The wire was braided such that a pitch of 2mm was attained. The woven material measured 85mm wide and was cut into four 400mm long sections. Each section contained 43 braids spaced 2mm apart. This created a total width of 340mm. The large sample size is necessary due to the aperture of the lens-horn antennas. The sections were placed in a test frame consisting of Plexiglas and wood, shown in Figure 2.3. Both ends of each section were wrapped around Plexiglas rods to create a total

length of 340mm, held in place with Plexiglas beams, and secured in a wooden frame. The cross-head beam was attached to the frame with threaded nylon rods and nuts. The sections were pulled individually to ensure uniform tension in the sample. The whole sample was straightened further by raising the cross-head beam. This also aided with locating slack in the sample.
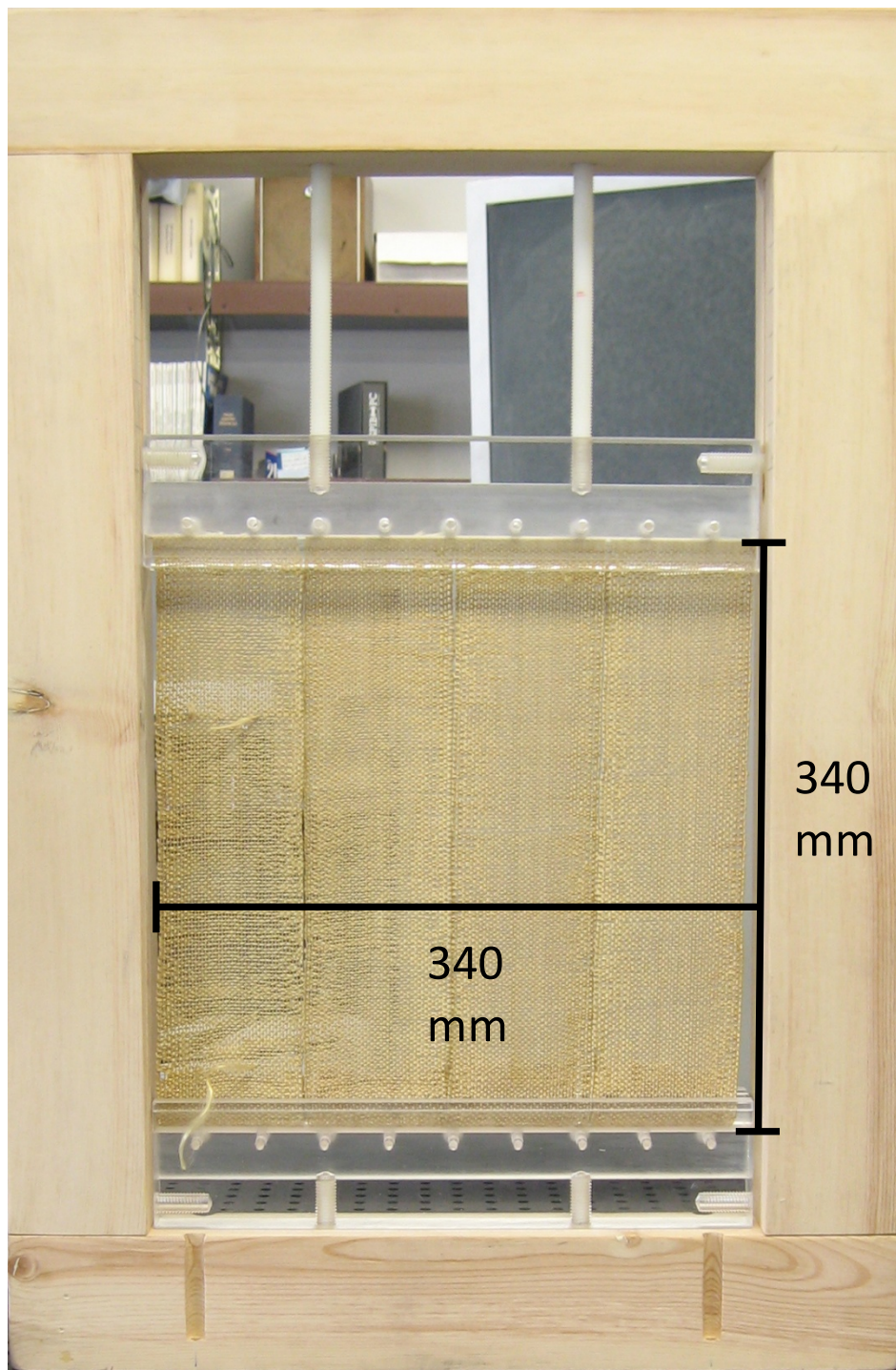
Figure 2.3: Electromagnetic test sample

Two horn antennas were placed on either side of the test fixture to measure reflected and transmitted signals, as shown in Figure 2.4. An Agilent 8510C Vector Network Analyzer (VNA) sent and received the signals.
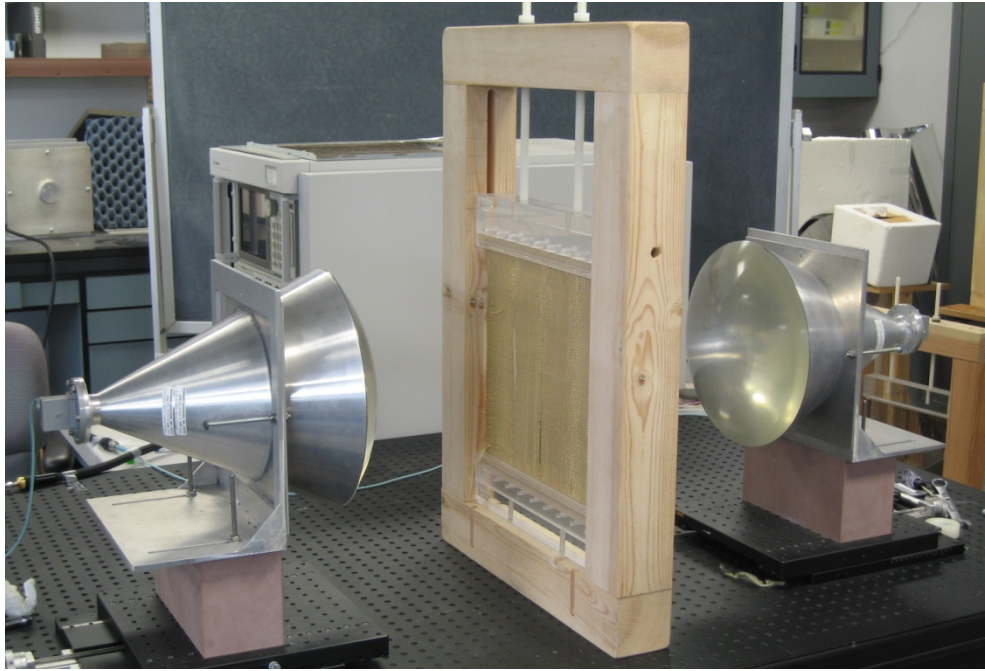
Figure 2.4: Test setup showing antenna placement and VNA location

2.3.2 Experimental Procedure

During the experiment, the VNA sent microwave signals in the 5.5GHz to 8GHz range with an absolute power output of 15dBm. This is the operating range of the horn antennas. Outside of this range, the received data is less reliable. Transmitted and reflected signals were received by the VNA and transferred to a computer in the form of S-parameters.

2.4 Simulation

To verify the results of the experiments, an electromagnetic simulation was created with Ansoft High Frequency Structural Simulator (HFSS). One full rotation of copper wire with surrounding material was modeled using master and slave boundaries. Two reflection-free perfectly matched layers (PML) were placed on either side of the material with a sufficient air gap to simulate the horn antennas used in the experiments and to minimize reflection. A diagram of the setup for the simulation is shown in Figure 2.5.
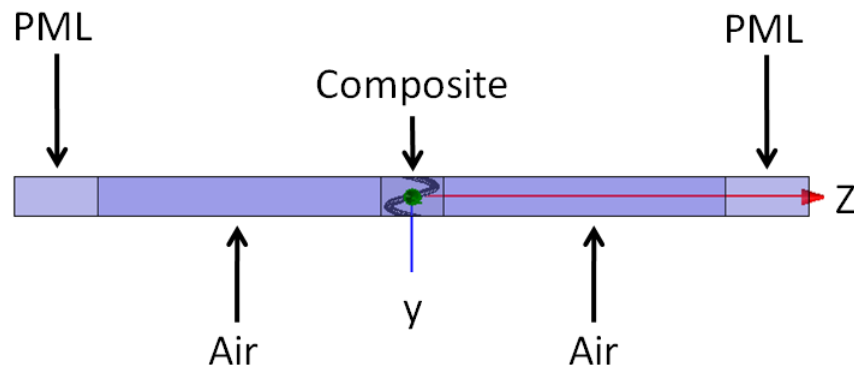
Figure 2.5: Schematic of the electromagnetic simulation showing the location of PML boundaries and air gaps around the composite

For simplicity, the fibers surrounding the wire, either Kevlar and nylon or Kevlar alone, were approximated as a solid block of material with a dielectric constant of 4.33. In other words, no air gaps existed between braids or between braids and weft in the model. Such an approximation, though unrealistic in this case, provides a first-order basis for comparison with the experiments. The dielectric constant comes from the polyamide material model, which is in the range of known Kevlar values.

The unit cell for the 2mm pitch braid measured 2x2x2mm. The coil had a wire diameter of 0.25mm and an inner diameter of 0.39mm. The unit cell for the 7mm pitch braid measured 1.98x7x1.98mm, with a coil inner diameter of 0.53mm and a wire diameter of 0.32mm. The axes were oriented such that the pitch extended in the y-direction. The signal was sent as a propagating incident plane wave excitation in the z-direction with the electric field either axially or normally polarized. Model parameters are presented in Figure 2.6.
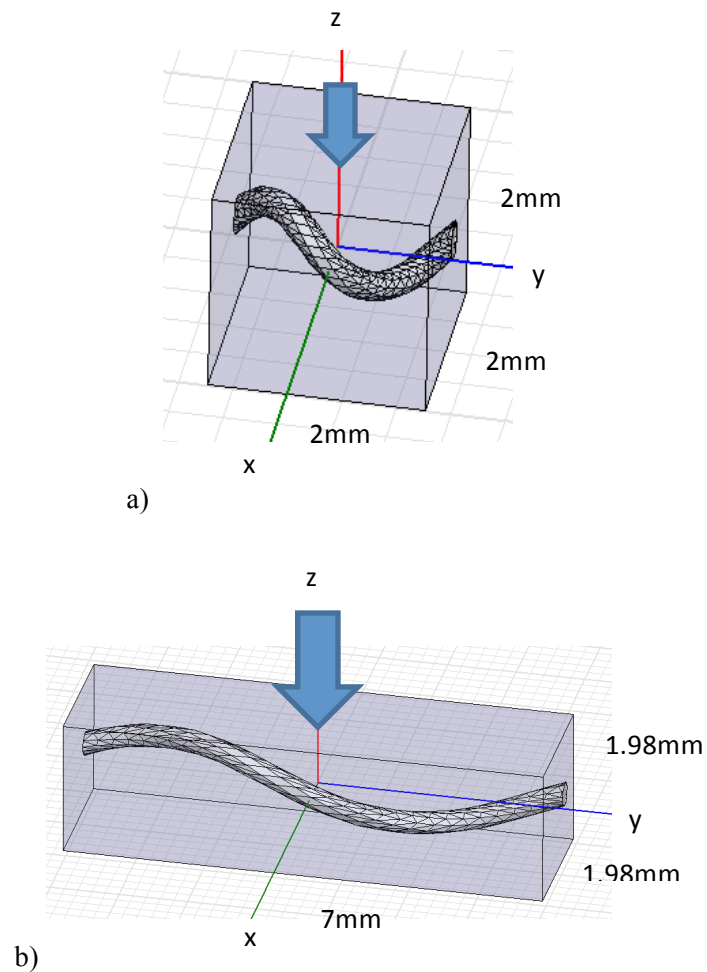
Figure 2.6: Model dimensions for a) 2mm pitch and b) 7mm pitch. The blue arrow indicates the direction of wave propagation.

The models were simulated over the frequency spectrum from 5 to 22GHz. This range was divided into 3 sections: 5-10GHz, 10-16GHz, and 16-22GHz. The first section was chosen for comparison with the experimental tests. The remaining two were chosen to pinpoint the plasmon frequency. Within each run, a discrete frequency sweep and an adaptive analysis were performed. The latter required the convergence of the solution in a minimum of 10 passes. This restriction ensured more precise results.

2.5 Results and Discussion

As the antennas operate between 5.5 and 8GHz, only this frequency range has both experimental data and simulation results. The magnitude of the S_{21} transmission for the axial polarization ($S_{21\text{-}zz}$) in the experiment closely follows the model prediction after 7GHz, as shown in Figure 2.7. Prior to this frequency, a maximum of 5dB separates the two sets of results. Similarly, the magnitude of the S_{21} transmission for the cross polarization in the experiment resembles the simulation result until 7GHz, when it begins to diverge with a maximum separation of 5dB. Since the simulation models the fiber matrix as a solid block surrounding the coil rather than as a braid with air gaps, a difference in measured parameters is not unexpected. Adding air gaps on either side of a narrower block could improve the approximation. However, the current difference is small relative to the difference between polarizations.
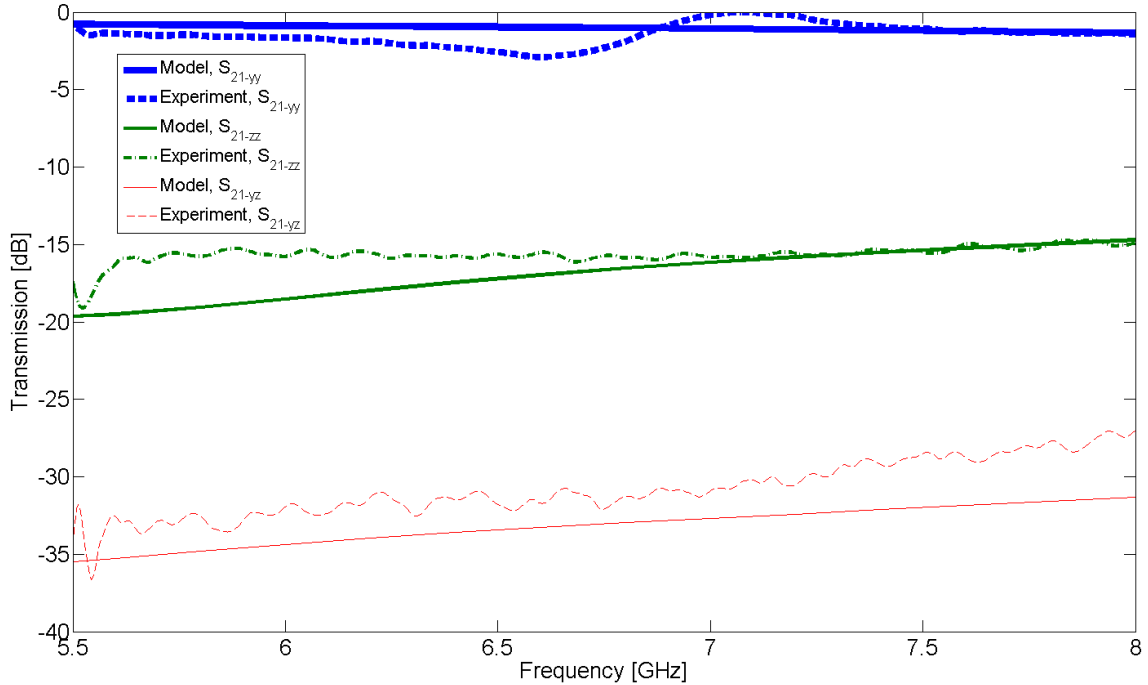
Figure 2.7: Transmission comparison between simulation and experimental results for perpendicular polarization, S_{21-yy} (blue), axial polarization, S_{21-zz} (green), and cross polarization, S_{21-yz} (red).

The magnitude of the axial polarization shown in Figure 2.7 is also an indication of the amount of chirality in the composite. Over the frequency sweep, the transmission measured -20 to -15dB. A nonchiral material would show magnitudes of -80dB. This demonstrates that there is a great deal of chirality present. The extent of this effect is shown in Figure 2.8. Due to rotation of the electric field, the polarization contour of a chiral material resembles an ellipse, whereas nonchiral materials display linear behavior. The amount of rotation of the polarization contour indicates the degree of chirality. From Figure 2.8, it is clear that this effect is strong in this composite.
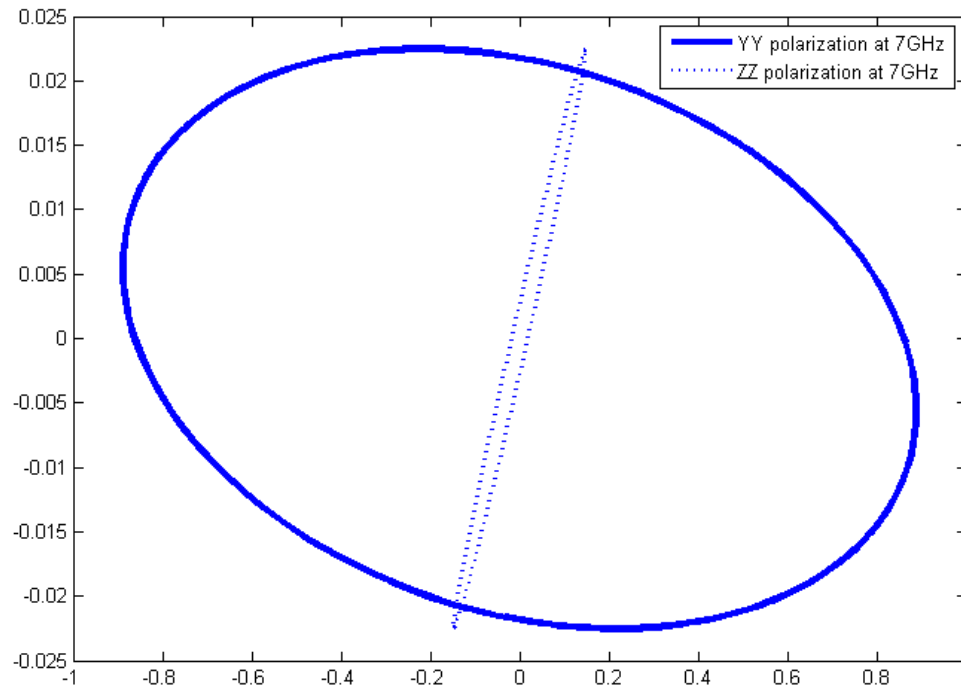
Figure 2.8: Polarization contours for axial (dotted) and perpendicular (solid) polarizations at 7GHz

A comparison between the simulation results of the 2mm fabric and those of the 7mm fabric show an increase in f_p with the increase in pitch and diameter. The S_{11} and S_{21} curves cross at 17.4GHz for the 2mm pitch fabric, shown in Figure 2.9a, and at 20.0GHz for the 7mm pitch fabric, seen in Figure 2.9b. This further illustrates the effect of coil properties on the plasmon frequency.
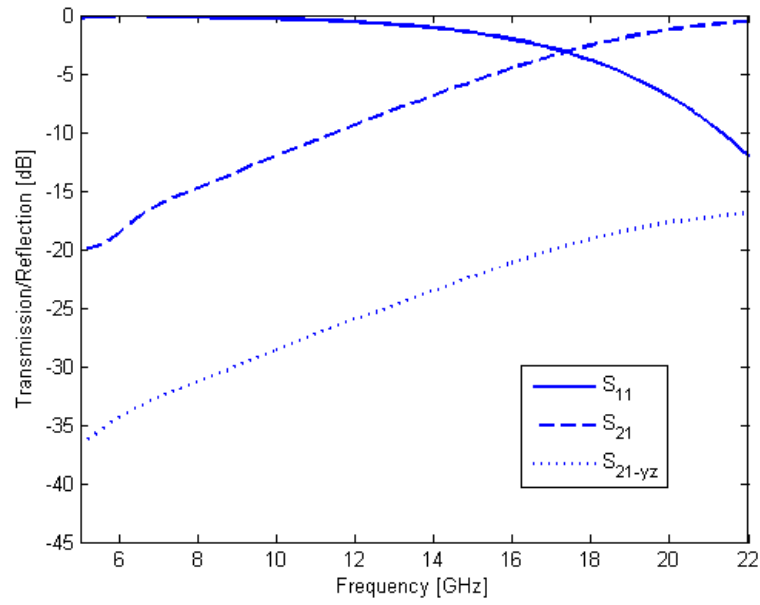
a)
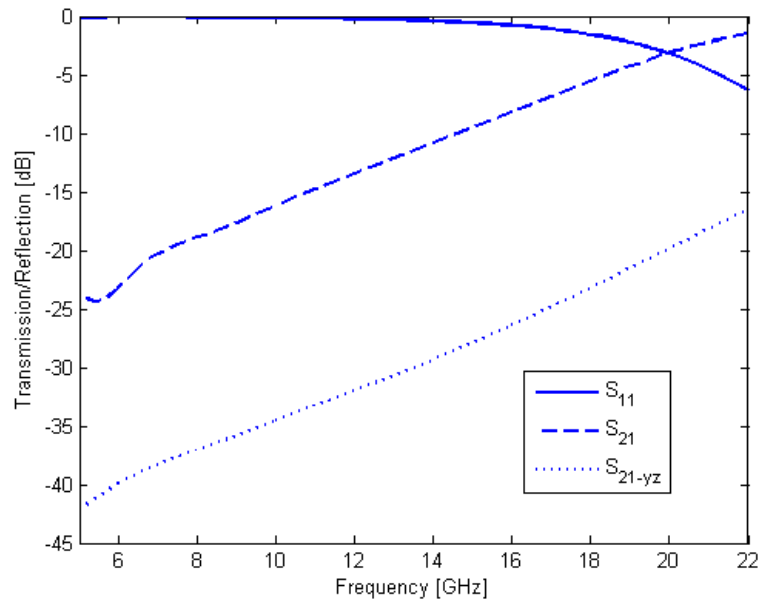
b)

Figure 2.9: Magnitude of S_{11} reflection, S_{21} transmission and $S_{21\text{-yz}}$ transmission for a) 2mm pitch fabric and b) 7mm pitch fabric

2.6 Conclusions

A chiral braided and woven composite was presented. The S-parameters measured through the experiment agreed well with the results of the simulation. Both indicate a considerable amount of chirality in the composite. Polarization contours confirmed this effect. An additional test with a fabric of greater pitch showed an increase in plasmon frequency consistent with previous work. This new material demonstrates a method to integrate electromagnetic properties into traditional composites to create an effective multifunctional material.

2.7 Acknowledgements

This research has been conducted at the Center of Excellence for Advanced Materials (CEAM) at the University of California, San Diego with partial support from AFOSR Grant FA9550-09-1-0528 to University of California, San Diego.

Chapter 2, in part, appears in Proceedings of SPIE Smart Structures and Materials & Nondestructive Evaluation and Health Monitoring, 18th Annual International Symposium, 2011 by S. Wheeland, A.V. Amirkhizi, and S. Nemat-Nasser. The dissertation author was the primary investigator and author of this paper.

2.8 References

[1] Huang, Z.M., "The mechanical properties of composites reinforced with woven and braided fabrics," *Compos. Sci. Technol.*, Vol. 60, 479-498, 2000.

[2] Naik, R.A., "Failure Analysis of Woven and Braided Fabric Reinforced Composites," *J. Compos. Mater.*, Vol. 29, No. 17, 2334-2363, 1995.

[3] Kang, T.J., and Lee, S.H., "Effect of Stitching on the Mechanical and Impact Properties of Woven Laminate Composite," *J. Compos. Mater.,* Vol. 28, No. 16, 1574-1587, 1994.

[4] Tabiei, A., and Yi, W., "Comparative study of predictive methods for woven fabric composite elastic properties," *Compos. Struct.,* Vol. 58, 149-164, 2002.

[5] Cox, B.N., Dadkhah, M.S., Morris, W.L., and Flintoff, J.G., "Failure Mechanisms of 3D Woven Composites in Tension, Compression, and Bending," *Acta Metall. Mater.,* Vol. 42, No. 12, 3967-3984, 1994.

[6] Jiang, Y., Tabiei, A., and Simitses, G.J., "A novel micromechanics-based approach to the derivation of constitutive equations for local/global analysis of a plain-weave fabric composite," *Compos. Sci. Technol.*, Vol. 60, 1825-1833, 2000.

Chapter 3

PCB Composites with Tunable Chirality

3.1 Introduction

Previous efforts in creating materials with turn-on frequencies in the microwave range demonstrated the effectiveness of using wire loops instead of the traditional thin wires [1,2,3]. Wire loops and coils allow for larger wire and smaller unit cells, increasing the feasibility of producing such a material. The coils also provide two more parameters that can be varied to change the plasmon frequency. The pitch between loops and the inner diameter of the coil, in addition to the diameter of the wire and the size of the unit cell affect the overall dielectric constant [4].

One way to create this type of material is by integrating such wire loops into a printed circuit board (PCB) design. PCBs are the standard method of circuit fabrication in electrical engineering. As a result, the technology is reliable and well-defined [5]. By using this fabrication technique, coils can be incorporated into a structurally stable, rigid chiral material. Previous work into the integration of helices onto a PCB focused primarily on antenna design [5,6,7]. Ensuring each helical element has the same handedness induces chirality in the composite. The incorporation of varactor diodes into the circuit allows for tuning of the chiral response via adjusting the reverse bias voltage. This research combines the interesting behavior of an array of copper coils with the reliability of PCB techniques to create a composite with a tunable electromagnetic response.

3.2 Electromagnetic Simulation

3.2.1 Preliminary Design

Prior to PCB fabrication, electromagnetic simulations were conducted to predict the response of the circuits using the Ansoft HFSS finite element solver. Periodic boundary conditions were attained via master and slave boundaries. Several configurations were considered. The effect of pitch was initially investigated by simulating 3mm and 8mm pitch periodic coils spaced 3mm apart. A spacing study was performed with either 1.5mm or 3mm between coils with a 3mm pitch. Model dimensions for these preliminary simulations are shown in Figure 3.1. For all of these, HFSS scanned the 4-12GHz frequency range.
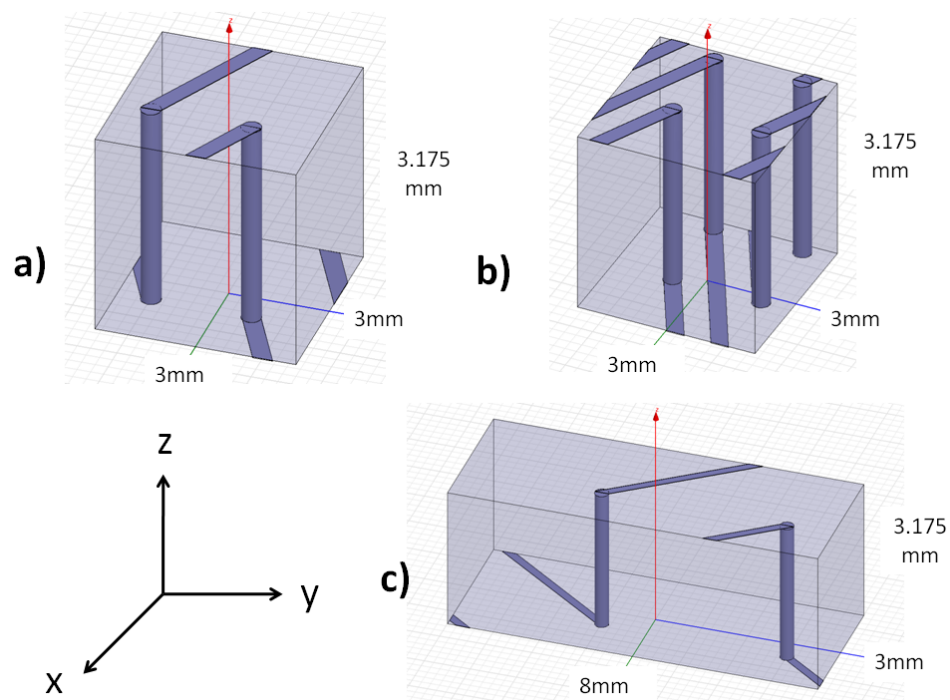
Figure 3.1: Model dimensions for a) 3mm pitch and 3mm spacing, b) 3mm pitch and 1.5mm spacing, c) 8mm pitch and 3mm spacing

The effect of multiple layers of PCB was examined using 3mm pitch coils spaced 3mm apart in either 1, 2, 3, 4, or 5 layers, including a 2-layer study where the coils in one layer were rotated by 38° with respect to the horizontal axis. Model dimensions are given in Figure 3.2.
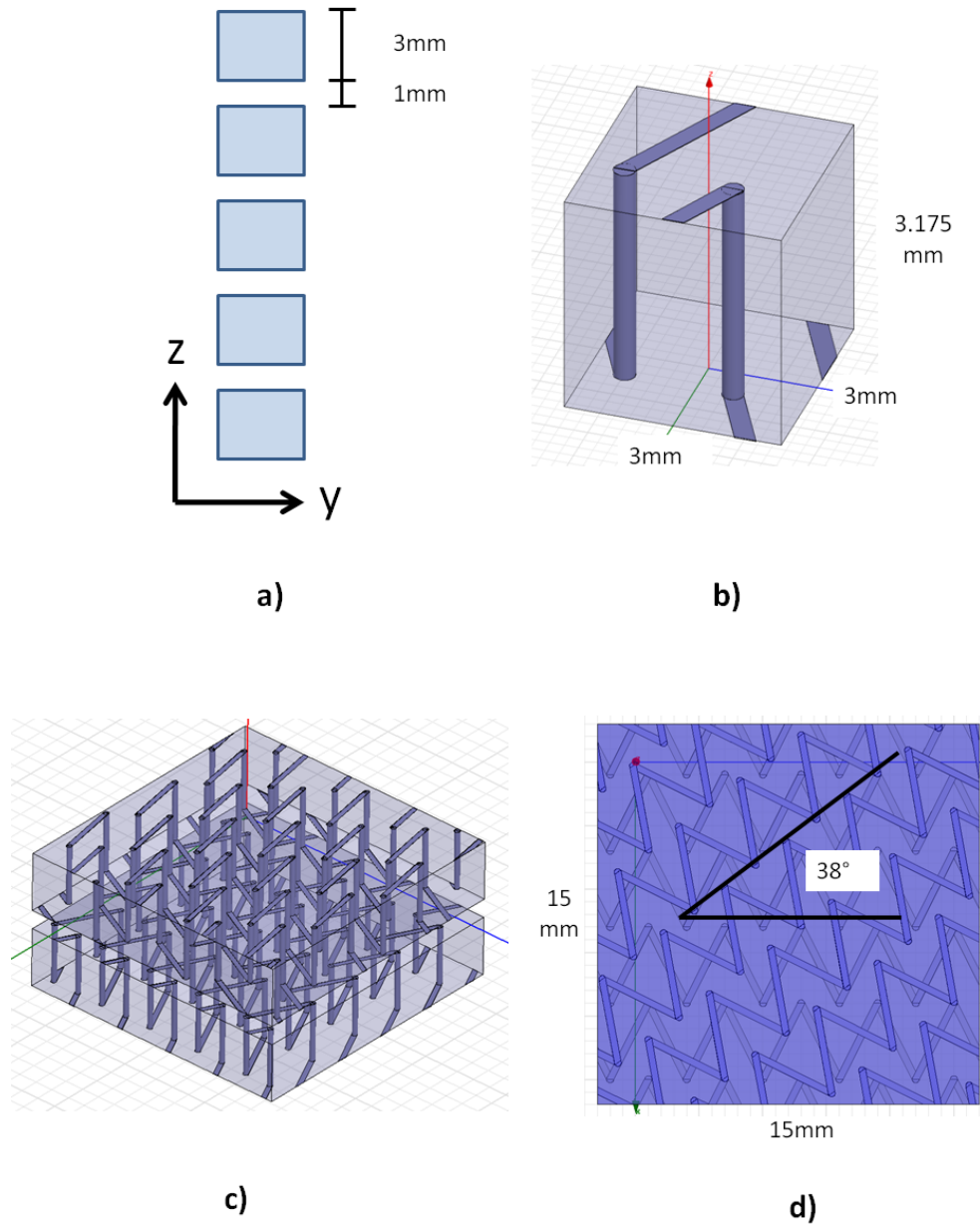
Figure 3.2: Model dimensions for the PCB layer study: a) layer spacing, b) unit cell, c) 2-layer angled PCB isometric view, and d) 2-layer angled PCB top view

Electromagnetic tuning was also investigated by inserting capacitors into the helix structure, as shown in Figure 3.3, and varying the capacitance between 0.1pF and 2.0pF. These

studies were conducted over two frequency ranges: 4-12GHz and 14-26GHz. Each range was chosen to simulate a different pair of antennas used in the experiments.
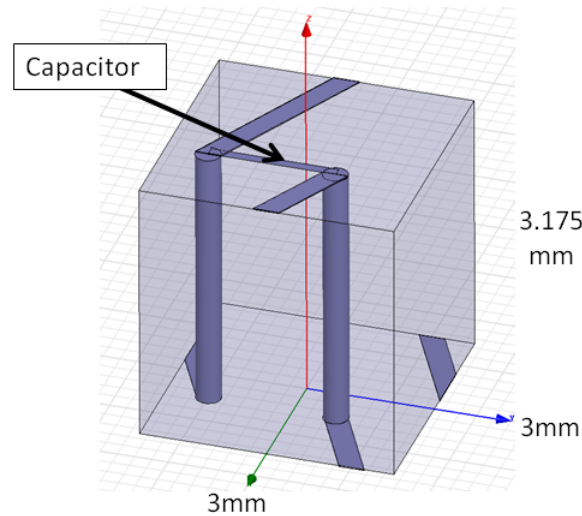
Figure 3.3: Periodic cell for PCB coil with capacitor

In each of the simulations, high transmission was received for at least one configuration. The goal for the PCB spacing and pitch studies was to pinpoint a design that would exhibit high transmission in the X band (8-12GHz). As can be seen in Figure 3.4, the 3mm pitch and 3mm spacing combination has the highest magnitude of transmission over the frequency range, making it an ideal candidate for the PCB.
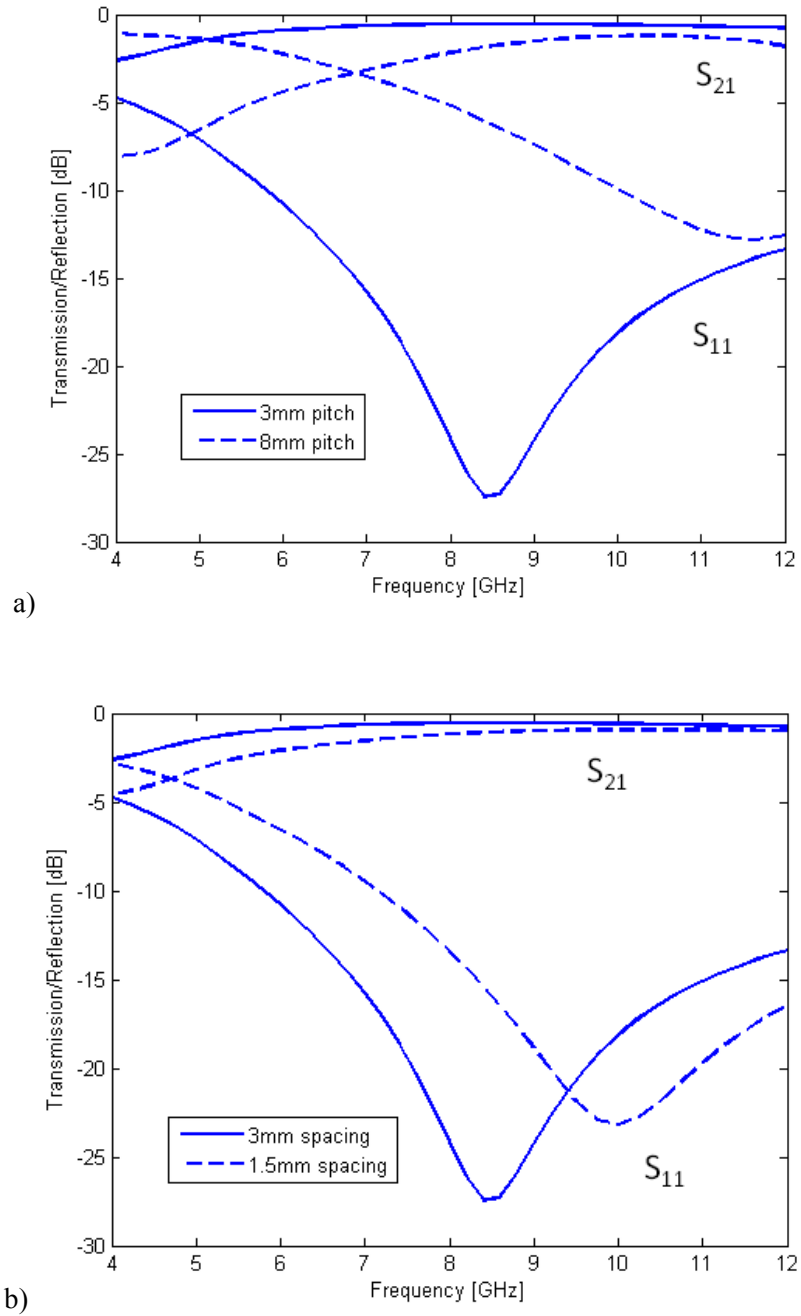
Figure 3.4: Magnitude of S_{11} reflection and S_{21} transmission over the frequency spectrum with axial excitation for a) 3mm and 8mm pitch with 3mm spacing, and b) 1.5mm and 3mm spacing with 3mm pitch

The results of the layer study do not seem to show a distinction between the numbers of layers in the simulation. As seen in Figures 3.5 and 3.6, there is no clear trend. The number of

layers in the simulation does not correlate to an effect on the magnitude of reflection off of or transmission through the material. One layer, four layers and five layers appear to have the greatest transmission, with five layers exhibiting near-perfect transmission.

One possible explanation for this is the electric field. As the wave travels through the PCB, the electric field is rotated from the bottom surface to the top surface due to the chirality in the material. When the wave encounters the next layer, the electric field is no longer polarized in the same direction as the layer. This causes the transmission to decrease and continues to rotate the electric field until the next layer and so on. In addition, the separation between the layers, 1mm, may not provide adequate spacing for the wavelength between layers.
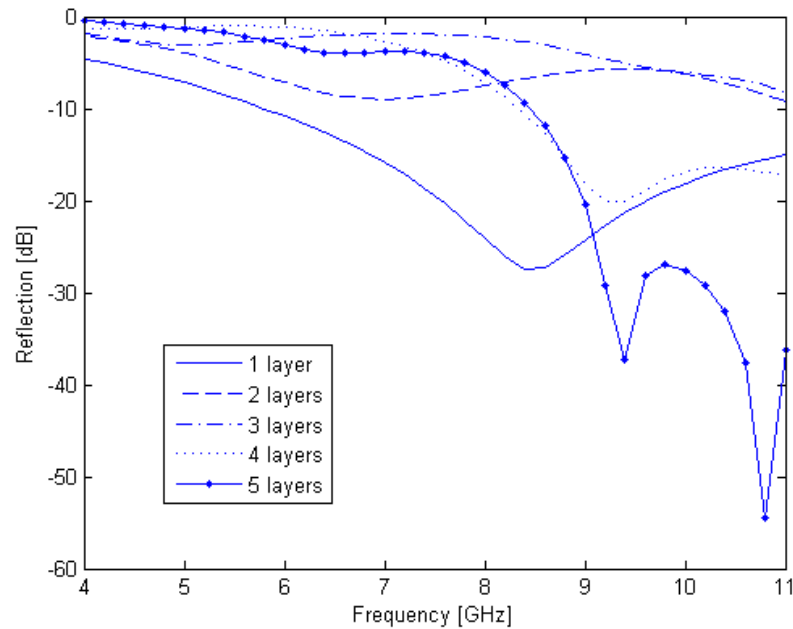
Figure 3.5: Magnitude of S_{11} reflection for axial excitation over the frequency spectrum for various numbers of layers
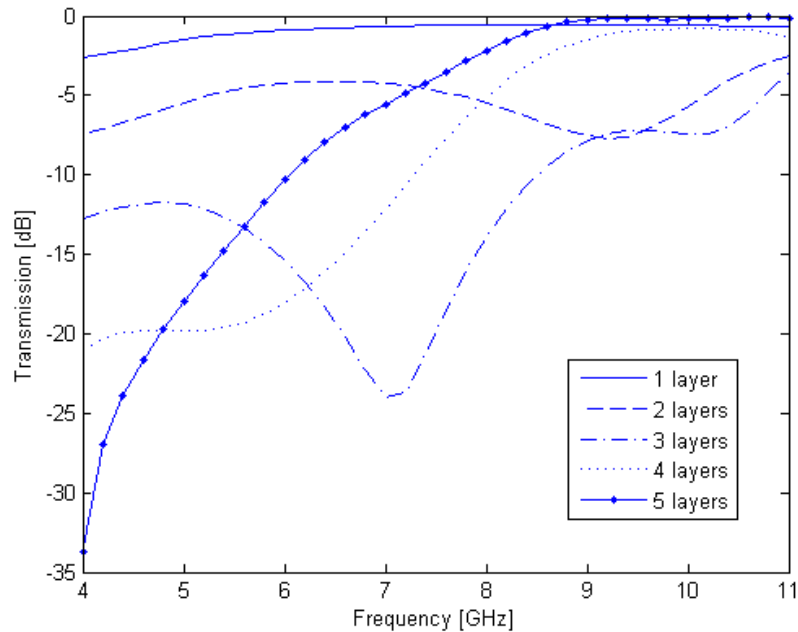
Figure 3.6: Magnitude of S_{21} transmission for axial excitation over the frequency spectrum for various numbers of layers

To investigate the rotation of the electric field, a two layer simulation was conducted with the top layer rotated at an angle of 38° with respect to the y-axis. Due to geometric constraints, this angle was chosen based on the 3-4-5 triangle, which gives the smallest integer periodic cell. Larger periodic cells are possible; however, here they are infeasible due to the processing power required for the solution. Initial results show that this configuration is not ideal for the rotation of the field. Further investigation via computer simulation is not possible without access to more extensive computing resources.

Varying the capacitance has a small effect on the electromagnetic response of the material. As illustrated in Figure 3.7a, increasing the capacitance in the system slightly increases the reflectivity of the material at lower frequencies. This is not the case at higher frequencies, which show identical behavior despite the value of the capacitance, see Figure 3.7b.
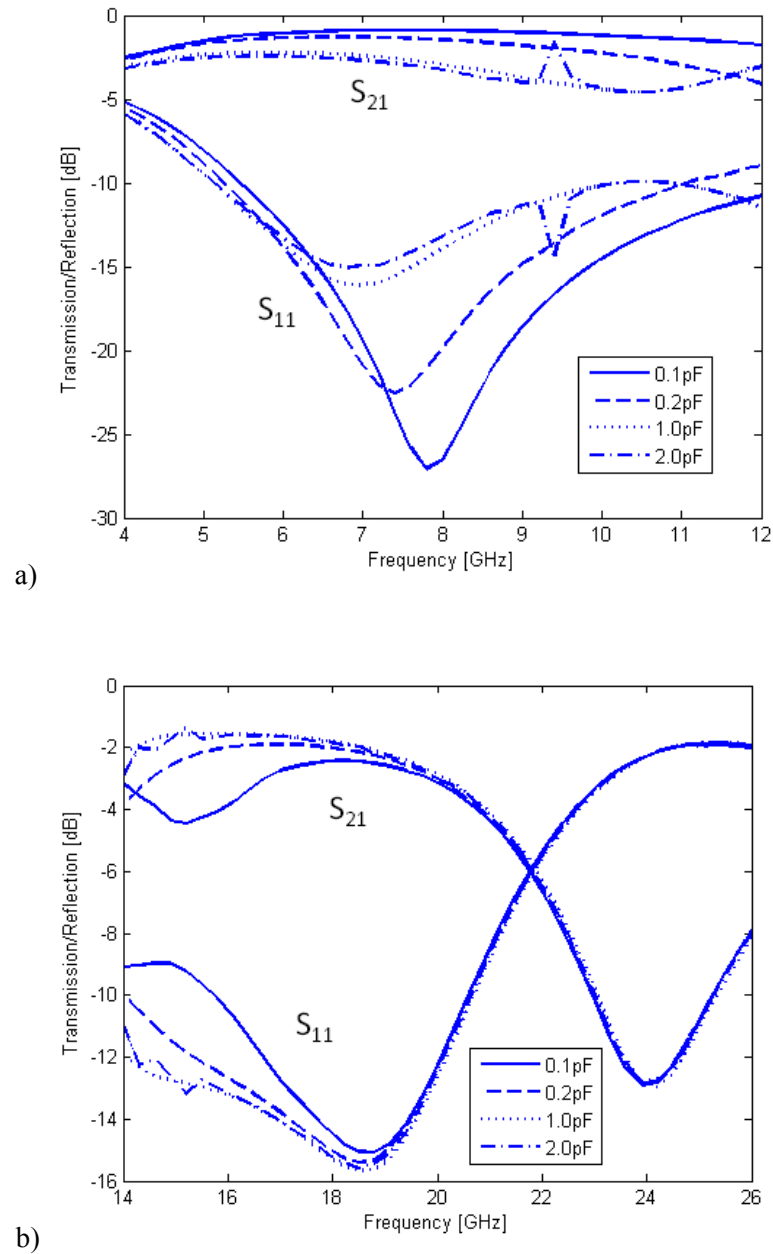
Figure 3.7: Magnitude of S_{11} reflection and S_{21} transmission for 4 capacitance values with axial excitation over the frequency spectrum, a) 4-12GHz and b) 14-26GHz

Varying the capacitance also has a dramatic effect on the chirality in the material. As seen in Figure 3.8, an increase in capacitance transforms the polarization contour from a nearly linear relationship to an elliptical one. Changing the capacitance seems to have a larger effect at

lower values; the difference between the polarization contours for 1.0pF and 2.0pF are nearly identical.
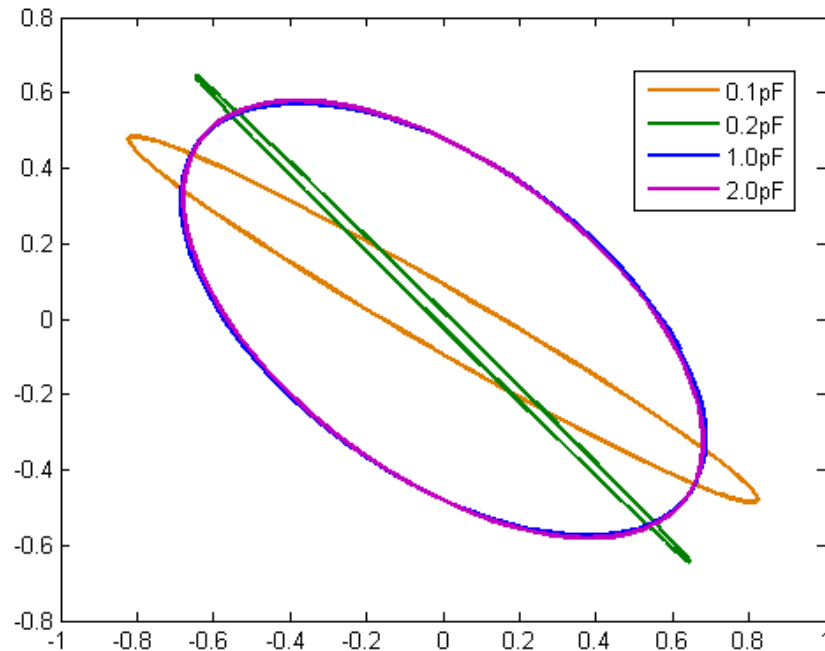
Figure 3.8: Polarization contours for 0.1pF, 0.2pF, 1.0pF, and 2.0pF capacitors at 12GHz. Note the change in shape from 0.2pF (green curve) to 2.0pF (purple curve).

3.2.2 Redesign

Though the preliminary design of 3mm pitch with 3mm spacing performed well in the aforementioned simulations, such a configuration requires an unreasonable amount of varactors for tuning. The goal of the PCB-helix redesign is to maintain microwave transparency and cross-polarization levels in a certain band while minimizing the number of varactors required for tuning. To determine the most appropriate design to accomplish this goal, the effects of pitch, spacing, trace width, substrate dielectric constant and thickness, capacitance, and varactor placement are simulated. In the first study, pitch and spacing varied from 3mm to 9mm in 3mm increments. Figure 3.9a shows the total transmission levels for all of the configurations, while Figure 3.9b

shows the cross-polarization transmission levels for all of the configurations. The pitch parameter is color-coded and the spacing parameter is line-style-coded.

a)

b)
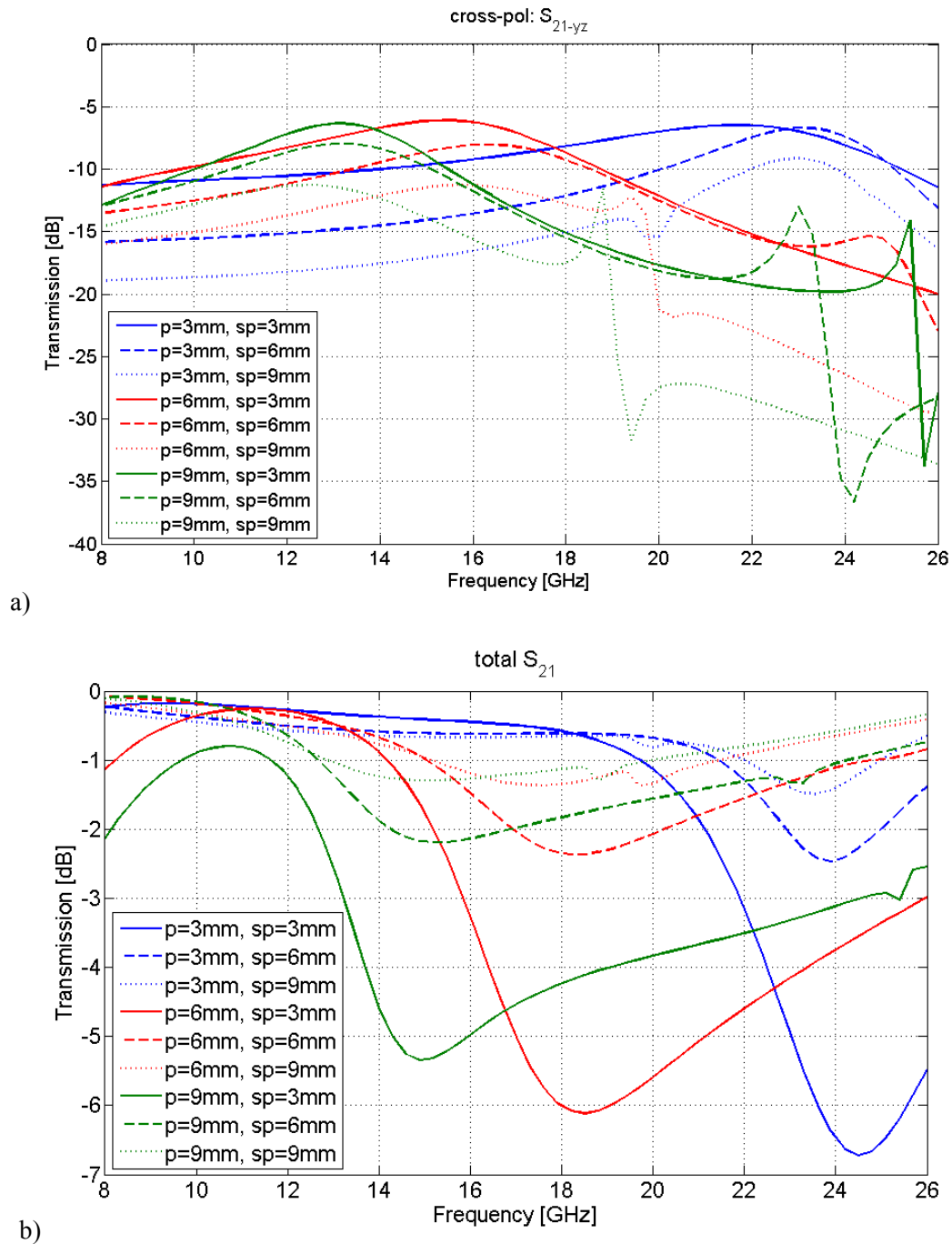
Figure 3.9: Effect of pitch and spacing on: a) cross-polarization transmission and b) total transmission.

The results demonstrate reasonably high transmission for most configurations in the 8-12GHz band. The higher frequencies (above 18GHz) show poorer transmission. For a given pitch, an increase in the spacing yields higher total transmission above 18GHz. Below 18GHz, the results are less conclusive. However, an increase in the spacing consistently leads to a decrease in cross-pol transmission. For a given spacing, an increase in pitch yields a decrease in total transmission, while leading to an increase in cross-pol transmission.

A second series of simulations investigated the effect of copper trace width on the performance of the composite. Using the square 3mm pitch x 3mm spacing, 6mm pitch x 6mm spacing, and 9mm pitch x 9mm spacing models, trace width varied between 0.3mm, 0.6mm and 0.9mm. As with the previous simulations, each case assumed a block of air surrounding the board with PML radiation boundary conditions at the ends. The results for all cases are shown in Figure 3.10. The blue lines represent the 3mm pitch x 3mm spacing model. The green curves show the 6mm pitch x 6mm spacing model. The red curves represent the 9mm pitch x 9mm spacing model. Solid lines indicate a trace width of 0.3mm; dashed lines indicate a trace width of 0.6mm; and the dotted lines represent a trace width of 0.9mm.
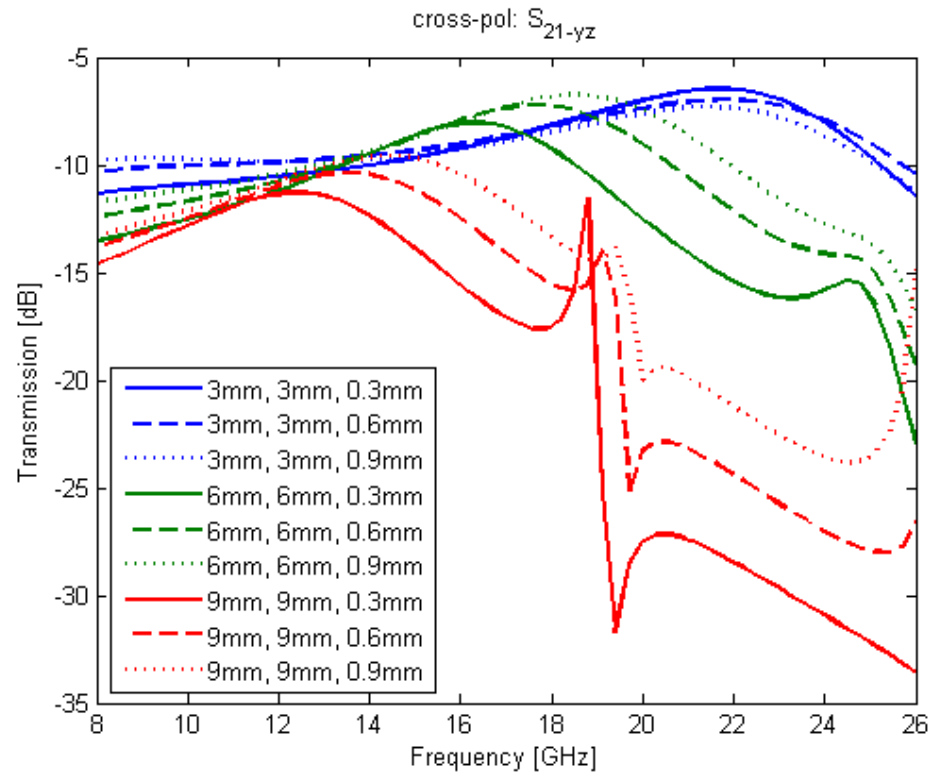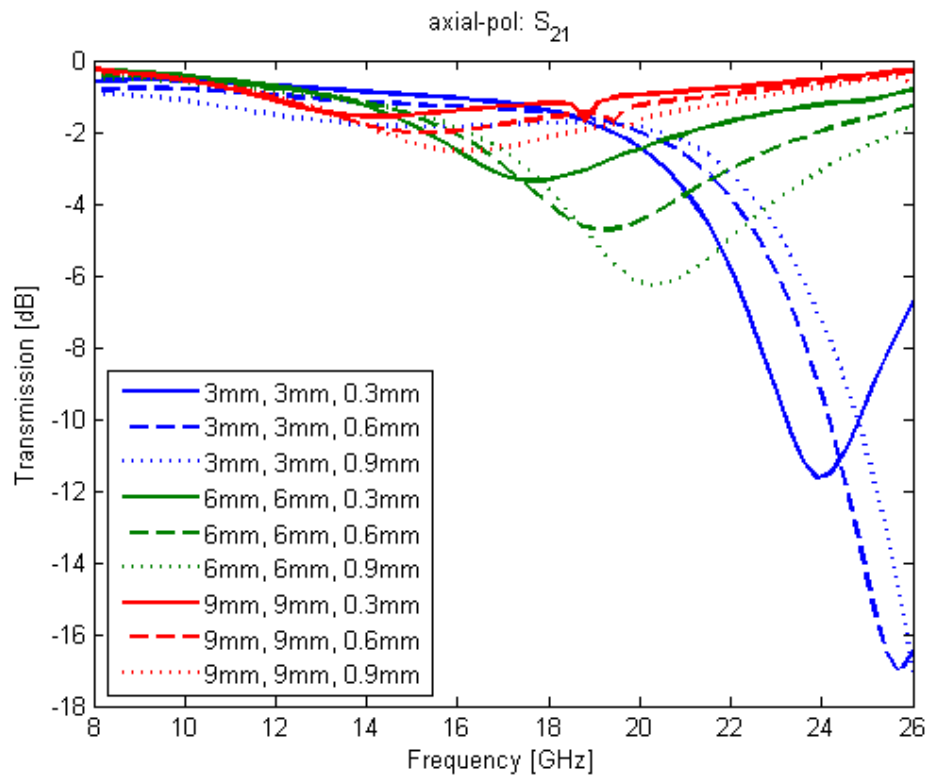
Figure 3.10: Effect of trace width on a) axial transmission and b) cross-polarization transmission.

As seen in the figure, increasing the width of the copper trace leads to a slight decrease in axial transmission and a slight increase in cross-pol transmission. An increase in trace width also leads to a frequency shift in the minimum and maximum peaks of S_{21} and $S_{21\text{-yz}}$, respectively. From the $S_{21\text{-yz}}$ graph, it is clear that higher frequencies have the highest cross-pol transmission. This is very significant for this project, as high cross-pol transmission indicates an increase in chirality (due to the rotating electric field).

The next simulations modeled a variance in the dielectric constant and in the substrate thickness for the 3mm pitch x 6mm spacing x 0.3mm trace width case. Figure 3.11 illustrates the effect of the dielectric constant for a substrate thickness of 3.175mm. As shown in the figure, an increase in the dielectric constant shifts the peak frequency to a lower value.

Figure 3.12 shows the dependence of the response on the thickness of the substrate. For these simulations, the dielectric constant was constant at 2.2. The first three thicknesses were chosen from a list of available board sizes. The last value (6mm) was arbitrarily chosen. From these, it is clear that increasing the substrate thickness from 0.792mm to 3.175mm increases the cross-pol $S_{21\text{-yz}}$ transmission while slightly decreasing the total S_{21} transmission. This signals an increase in the chirality of the system. However, a further increase in thickness causes a drastic change in the behavior of the board, leading to a maximum value of -5dB at 14GHz and a minimum value of about -43dB at about 16.5GHz. At 14GHz, the thickness of the board approaches a quarter wavelength, and thus more reflection is present.
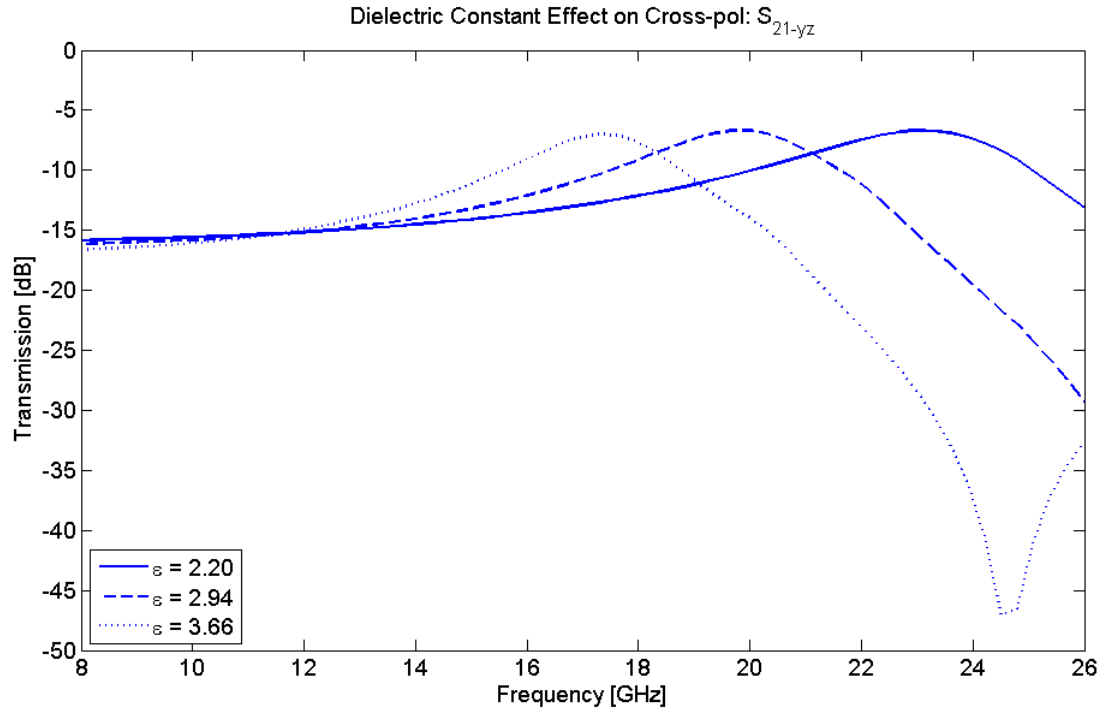
a)
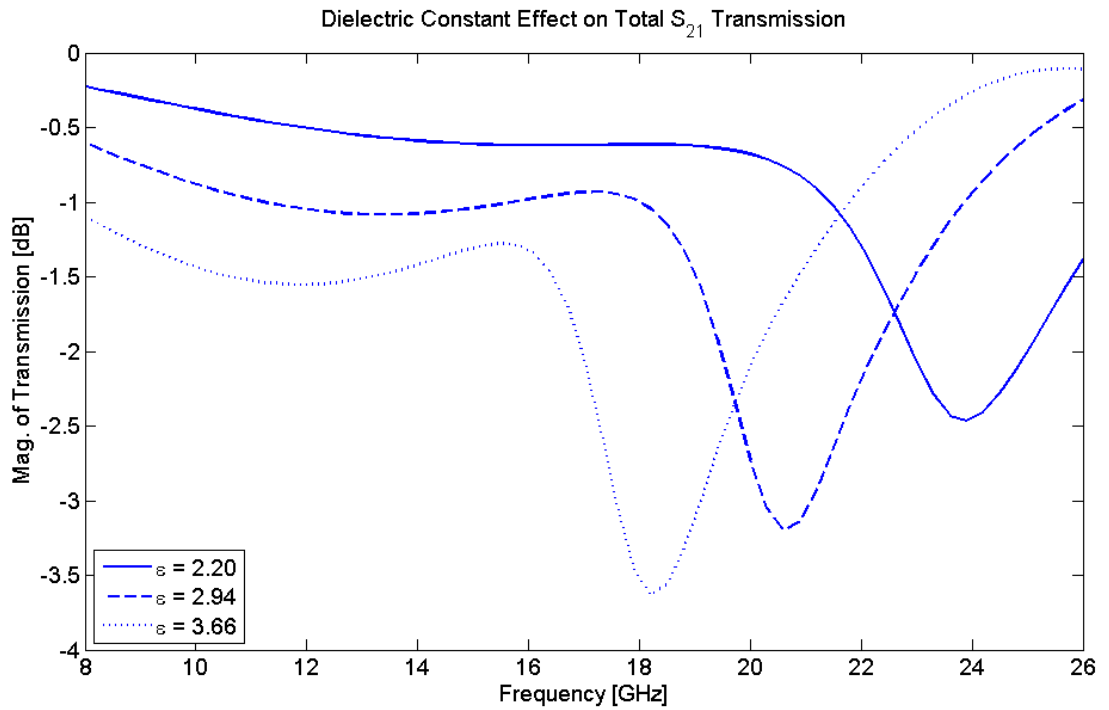
b)

Figure 3.11: Effect of dielectric constant on a) cross-polarization transmission and b) total transmission.

a)

b)
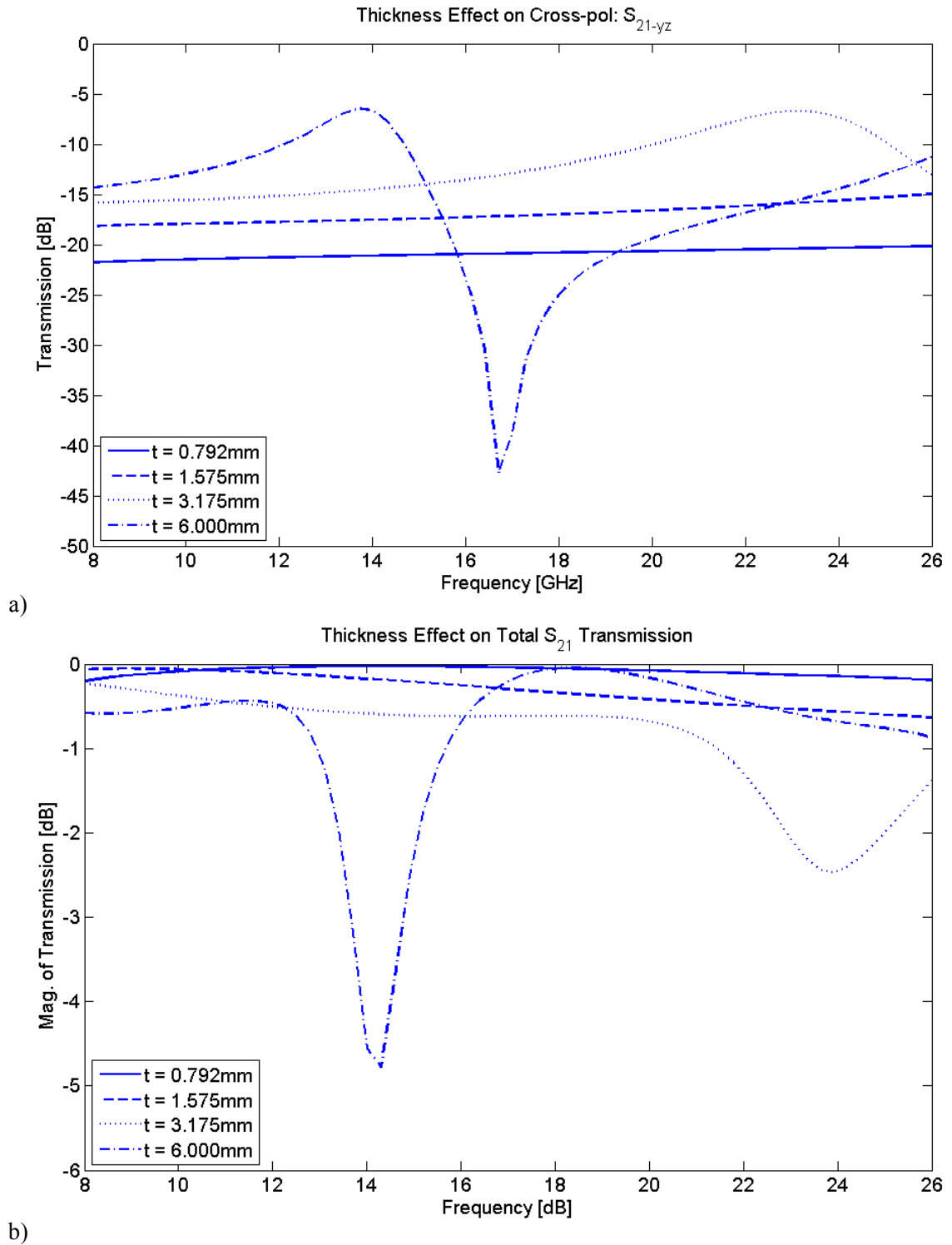
Figure 3.12: Effect of substrate thickness on a) cross-polarization transmission and b) total transmission.

The fourth set of simulations modeled the effect of capacitance on the performance of the composite for the 9mm pitch and 6mm spacing configuration. The model in each simulation had a board thickness of 3.175mm, a trace width of 0.3mm and a dielectric constant of 2.2. Here, frequency varied from 7 to 14GHz with capacitance values of 0pF, 0.1pF, 0.5pF and 1.0pF. The 0.1pF value was included to determine the sensitivity of the response to small capacitance variation.

Figure 3.13a shows the magnitude of transmission for the cross-polarized ($S_{21\text{-yz}}$) wave, while Figure 3.13b shows the magnitude of total S_{21} transmission. From these, it is clear that increasing capacitance affects the response of the model. This effect, however, only seems to exist for small capacitance values. Above 0.5pF, the response is essentially the same, regardless of capacitance. Below this value, the response changes dramatically with increasing capacitance values.
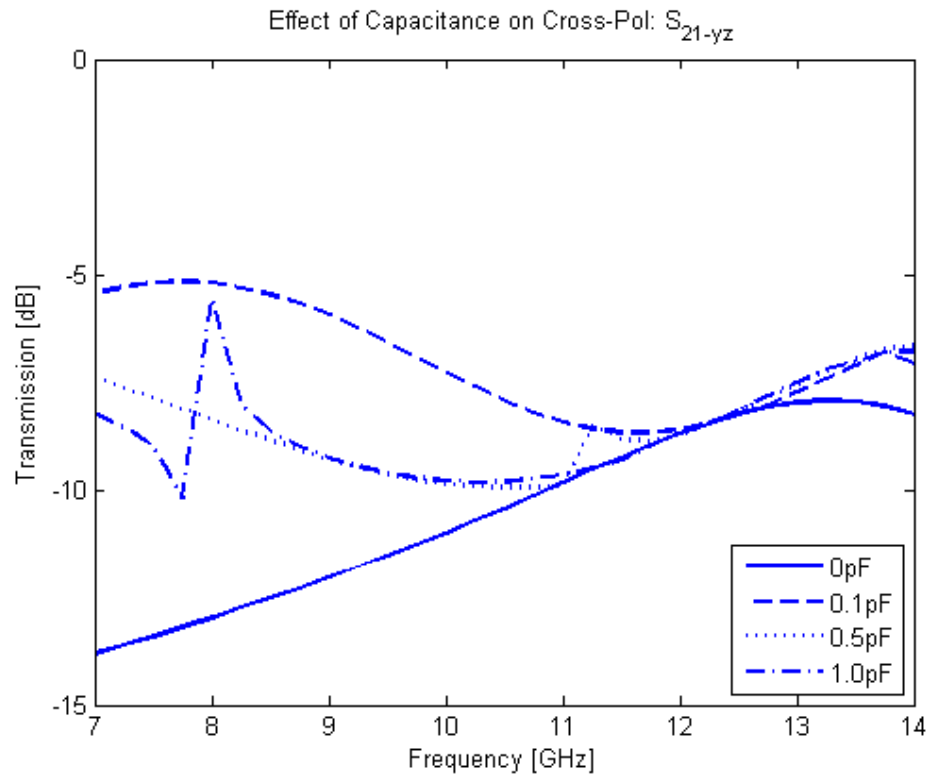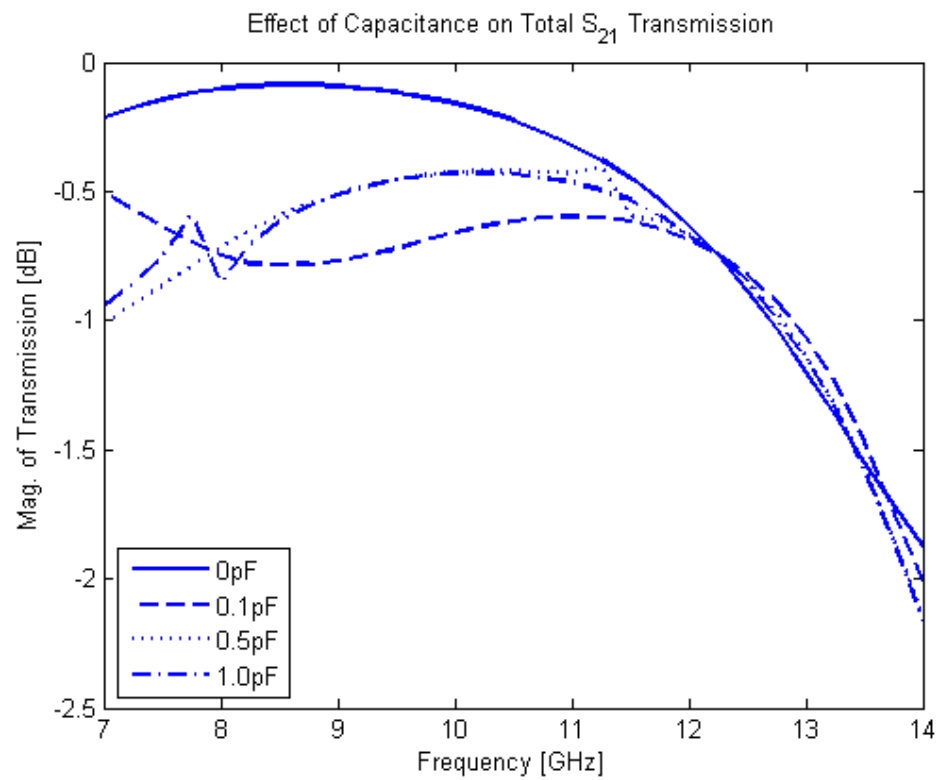
Figure 3.13: Effect of capacitance on a) cross-polarization transmission and b) total transmission.

The final round of simulations investigated various varactor configurations. For simplicity, each simulation modeled the 9mm pitch, 6mm spacing and 0.3mm trace width design between 14 and 21GHz. Figure 3.14a shows the $S_{21\text{-yz}}$ cross-polarization transmission for 0.1pF and 1.0pF for one capacitor placed vertically between two adjacent helices. Figure 3.14b shows the total transmission for 0pF, 0.1pF, 0.5pF, and 1.0pF for the same configuration. The greatest variation between the total transmission responses exists between 14 and 15GHz. However, this configuration appears to yield 0.5dB tuning in the cross-pol response. Figure 3.15 illustrates the difference between cross-polarization transmission when the incident wave is normal to ($S_{21\text{-yz}}$) and parallel to ($S_{21\text{-zy}}$) the varactor. As shown in the figure, there is a difference of about 2dB between the responses. This indicates variation in the through-thickness symmetry.
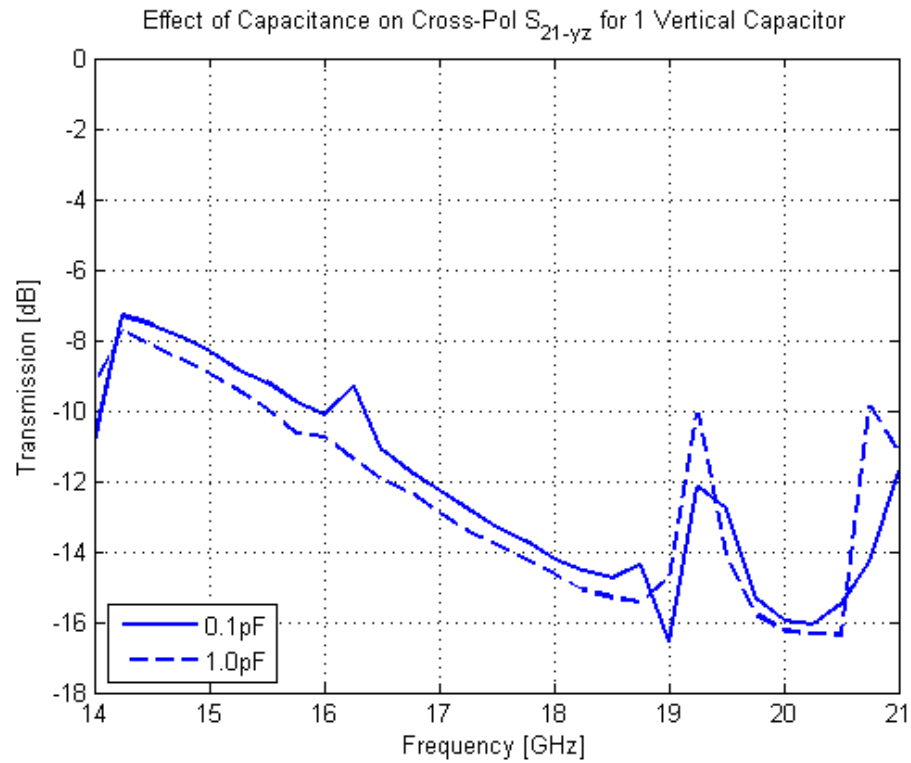
a)
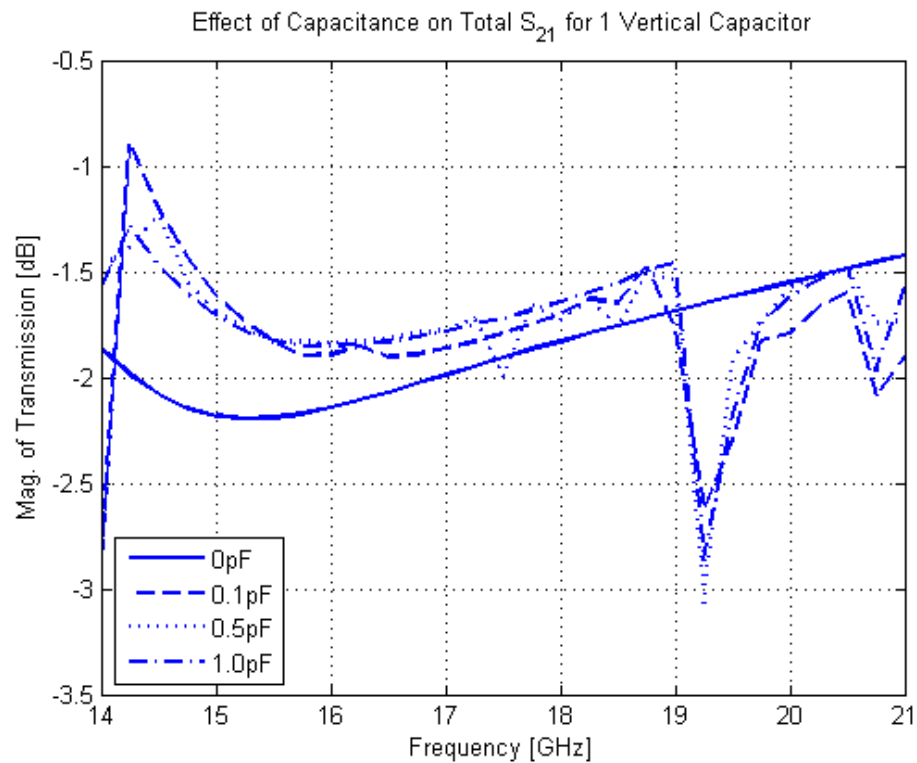
b)

Figure 3.14: Effect of capacitance of vertical varactor on a) cross-polarization transmission and b) total transmission
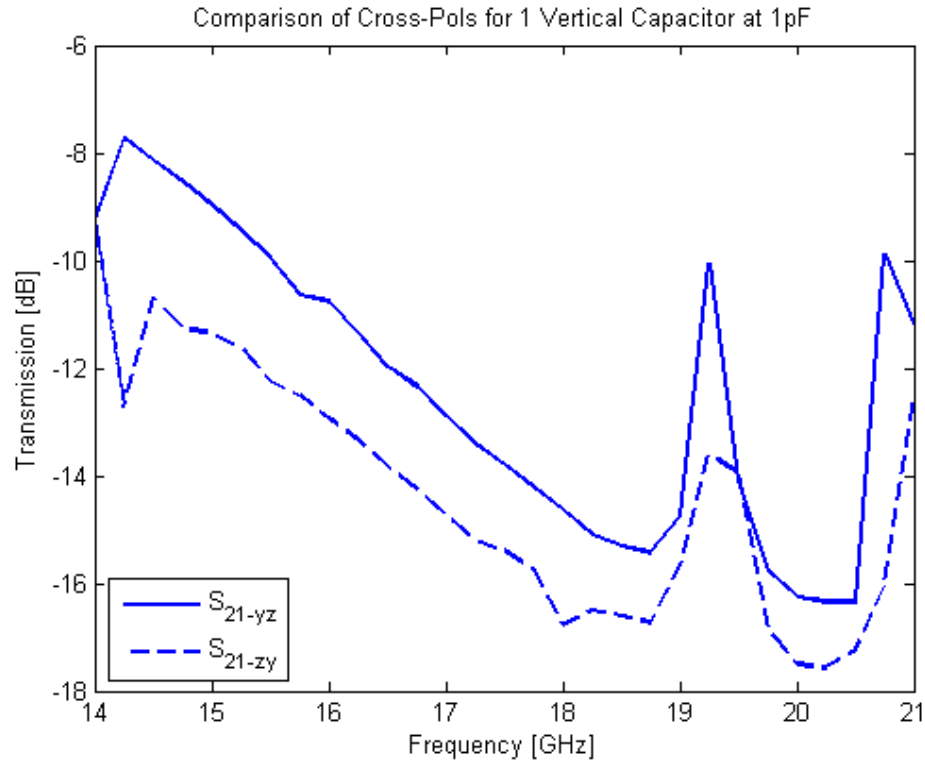
Figure 3.15: Cross-polarization transmission difference between front and back faces of PCB

The next simulations modeled two separate configurations for horizontally-placed varactors, shown in Figure 3.16. In the first case, the model consists of one varactor for every other open space. This means a total of half the number of varactors included in the original version. In the second case, varactors are placed on the top and on the bottom surfaces of the board. Though this would double the number of varactors required, this configuration may increase capacitance control due to the through-thickness asymmetry. Each simulation models the 9mm pitch, 6mm spacing and 0.3mm trace width design between 7 and 14GHz for capacitance values of 0, 0.1, 0.5, and 1.0pF.
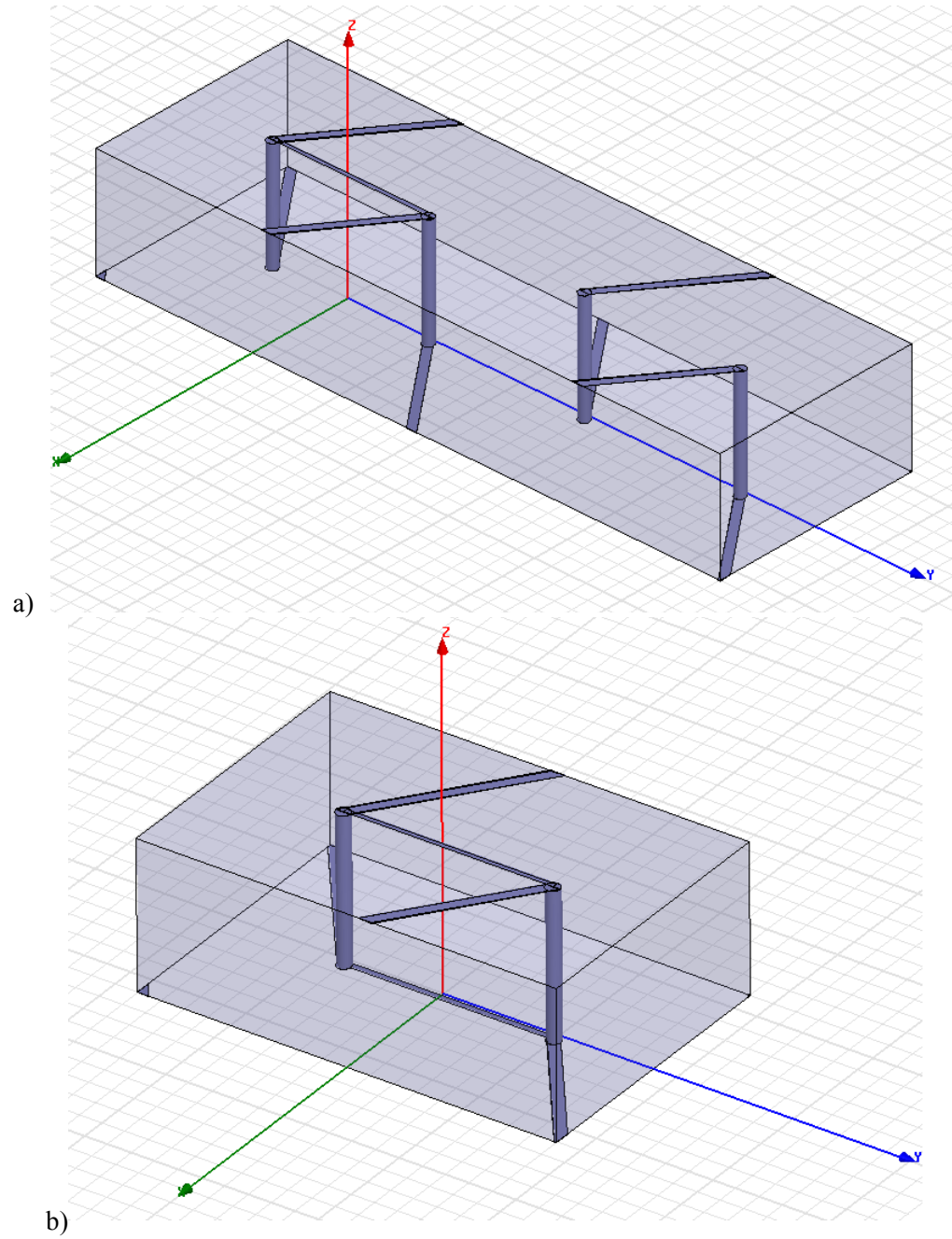
Figure 3.16: Model configurations for a) half-varactor design and b) double-varactor design

Figure 3.17 illustrates the response for the half-varactor design. Figure 3.18 displays the response for the double-varactor design. In each set, the first graph shows the $S_{21\text{-}yz}$ cross-polarization transmission. The second graph depicts the total S_{21} transmission. As can be seen in each design, the responses after 0.5pF are fairly similar. This is consistent with the behavior of the initial one capacitor per space design. It appears that greater tuning is achieved with the double-capacitor design, though the half-capacitor design also shows a great increase in cross-pol transmission at lower frequencies.
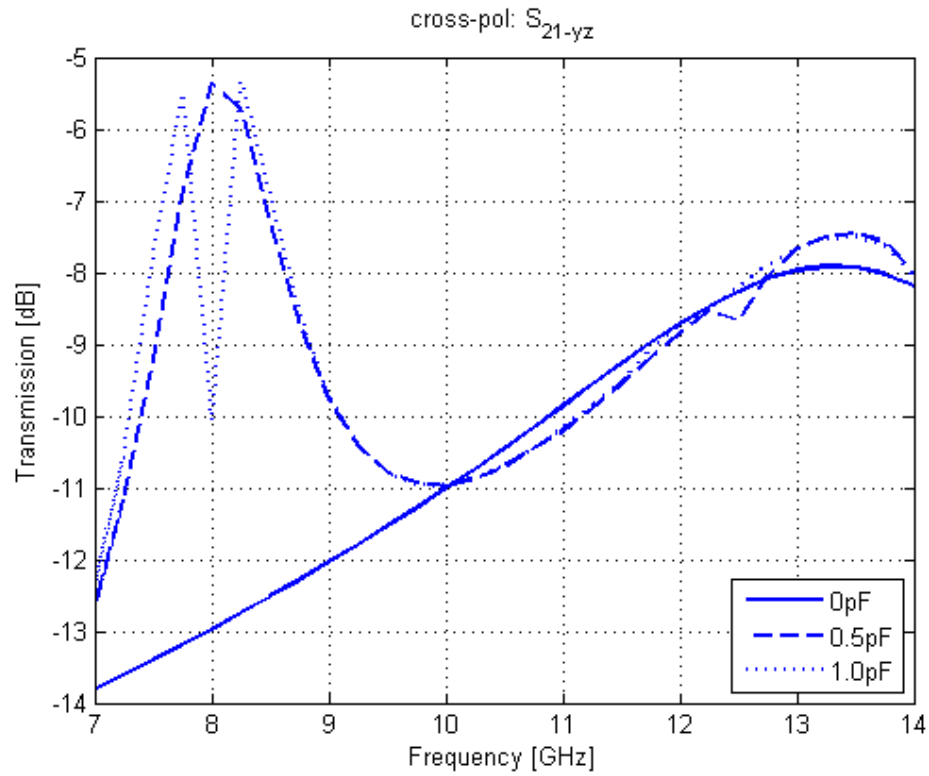
a)
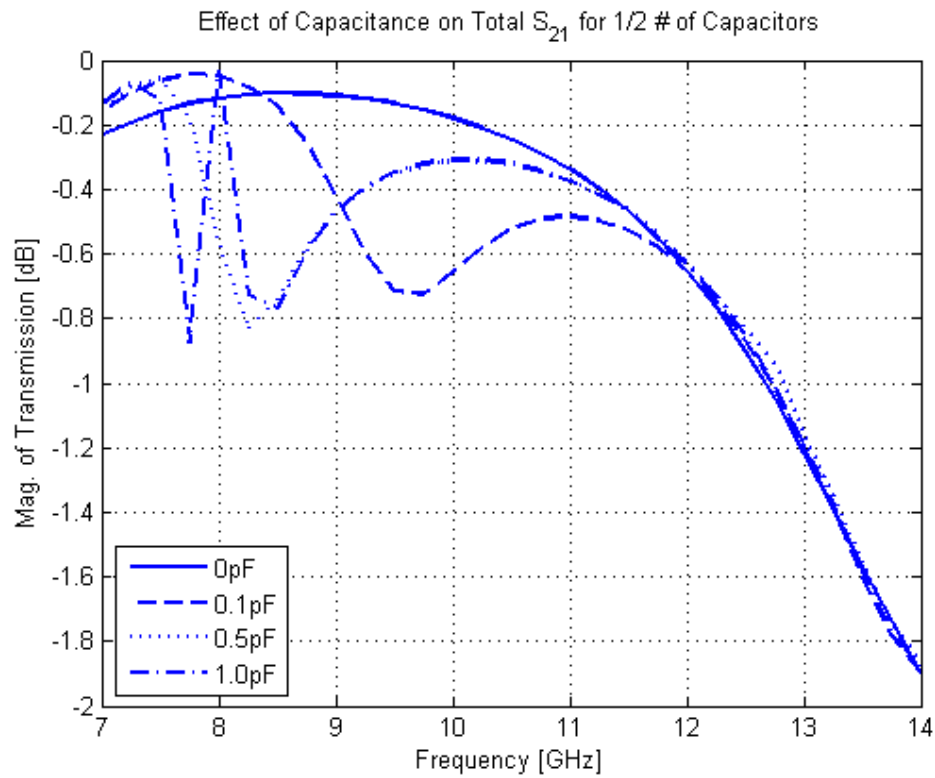
b)

Figure 3.17: Response for the half-varactor design
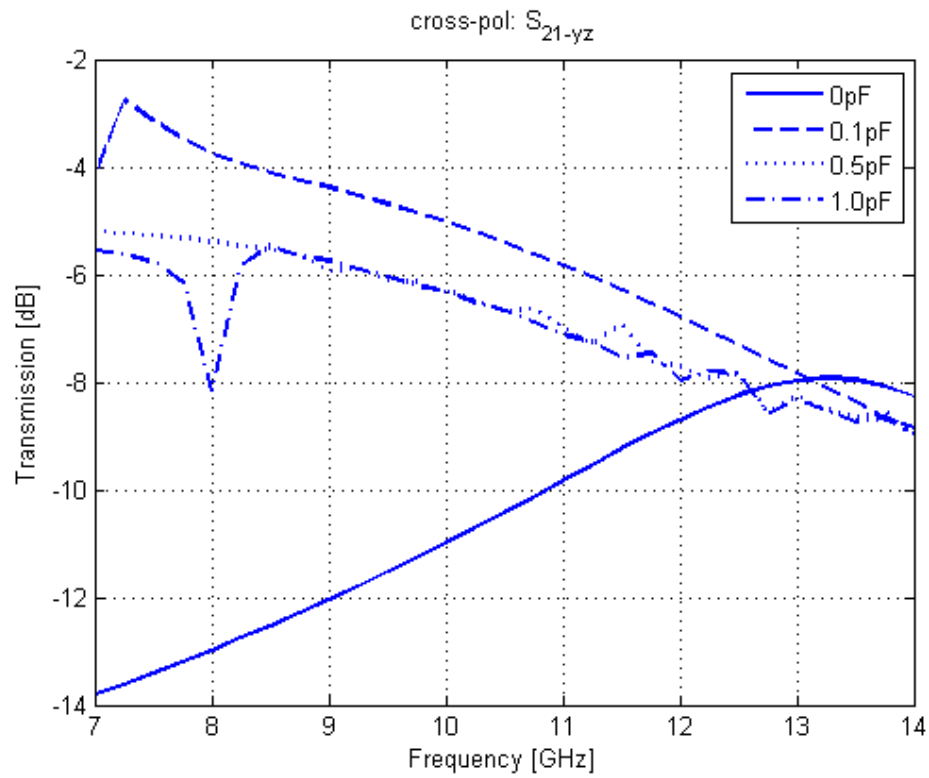
a)
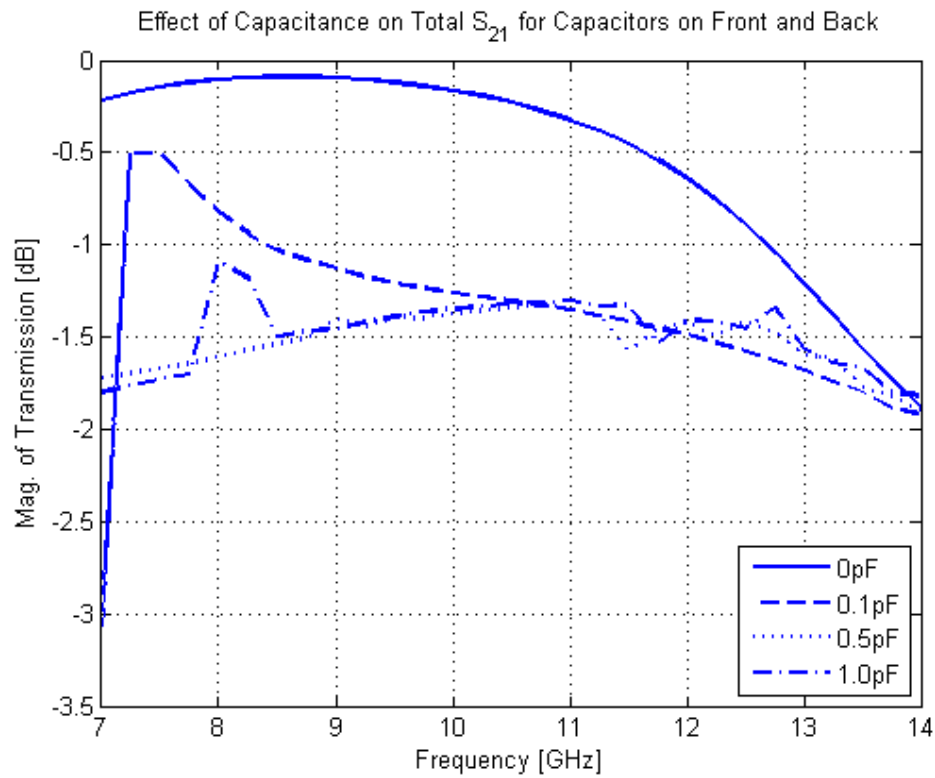
b)

Figure 3.18: Response for double-varactor design

Based on this analysis and the ultimate goal, the ideal sample consists of an array of helices with 9mm pitch, 6mm spacing and 0.3mm trace width on a 3.175mm thick substrate of dielectric constant 2.2 tested in the 8.2-12.4GHz-frequency range. With a varactor placed horizontally between the helices, this would require 660 varactors for a 198mm by 180mm board. With this configuration, transparency and cross-polarization performance are maintained while minimizing the required number of varactors.

3.3 Materials

Using the results of the simulations, the optimal design for the chiral array was determined and fabricated onto a PCB substrate. The experimental sample consisted of a high frequency circuit board from Rogers Corporation. Copper cladding on the RT/duroid® 5880 PTFE-glass microfiber composite board comprised the periodic helix pattern, as shown in Figure 3.19a. Holes were drilled and electroplated with copper to join the front and back faces, yielding rectangular helices. MA46H120 varactor diodes were obtained from M/A-COM Technology Solutions. The board material was obtained from Rogers Corporation and given to Hughes Circuits, Inc for circuit fabrication and component placement. The completed sample, including varactor placement, is shown in Figure 3.19b.
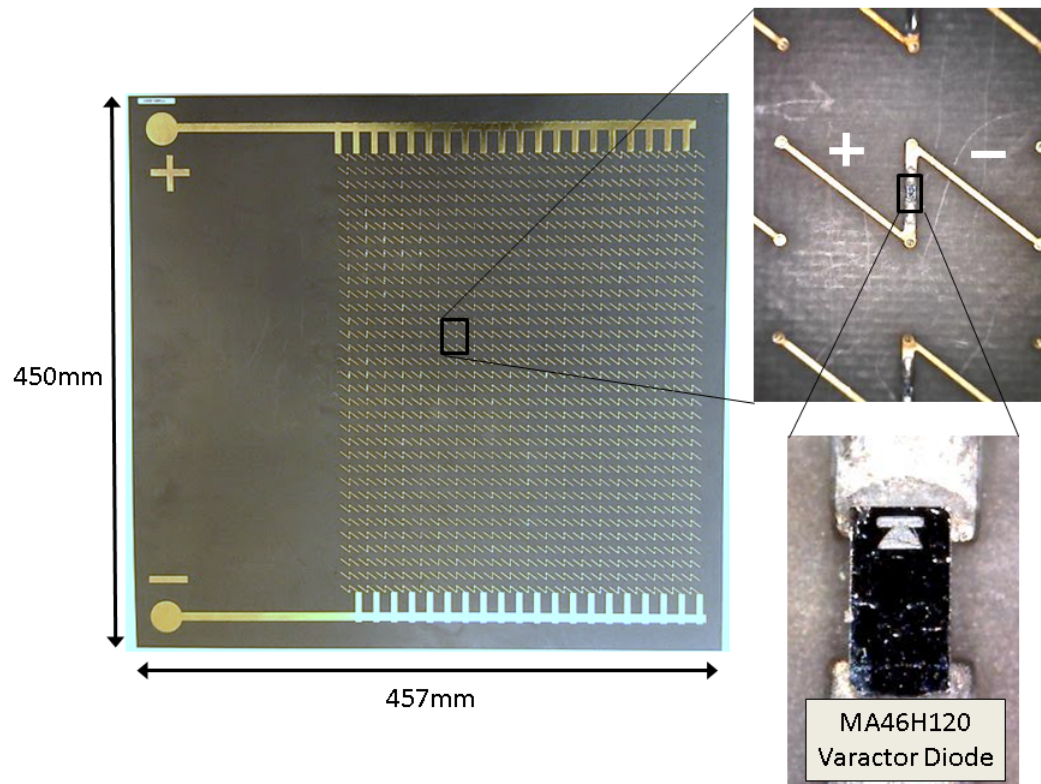
Figure 3.19: Sample specifications showing helix layout (pitch = 9mm, spacing = 6mm, trace width = 0.3mm, substrate thickness = 3.175mm) and varactor placement.

3.4 Experiments

3.4.1 Test Setup

Electromagnetic tests were performed using an Agilent 8510C Vector Network Analyzer (VNA). Two lens-horn antennas placed on either side of the sample measured the reflected and transmitted signals in the form of S-parameters, as shown in Figure 3.20. This represents the standard transmit/reflect (TR) setup used for measuring slab characteristics.
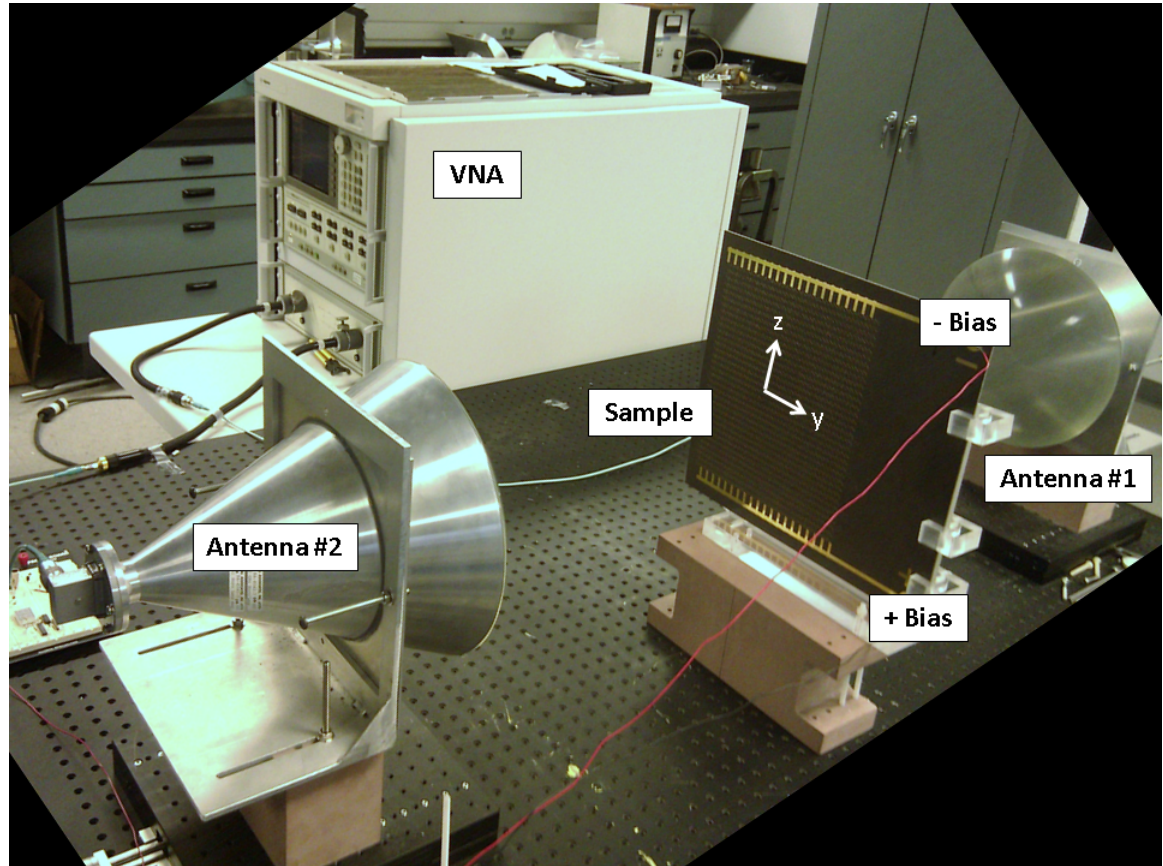
Figure 3.20: EM test setup using two lens-horn antennas connected to the VNA. Sample is placed equidistant from either antenna.

3.4.2 Experimental Procedure

Prior to testing, the system is calibrated using a standard two-port TRL technique. Thru, reflect and line standards are achieved, which provide the antennas with reference planes at the front and back surfaces of the sample. For each test, the 5.5 to 12.4GHz frequency range is scanned. Two sets of antennas are used to achieve this frequency range. The first pair operates between 5.5 and 8.2GHz. The second pair operates between 8.2 and 12.4GHz. Using a power supply, 1V, 3V, 11V and 15V are applied to the board via two bias ports. An increase in bias voltage causes a decrease in capacitance. Scattering parameters and relative magnitude and phase

measurements are taken at each voltage and frequency step to determine the overall electromagnetic response.

3.5 Results

As both axial and perpendicular incidence tests were performed, cross-polarization measurements for each of these cases are presented. Figure 3.21 shows the amplitude of the transmitted waves for both incidence polarizations in addition to polarization contours illustrating the change in chirality.
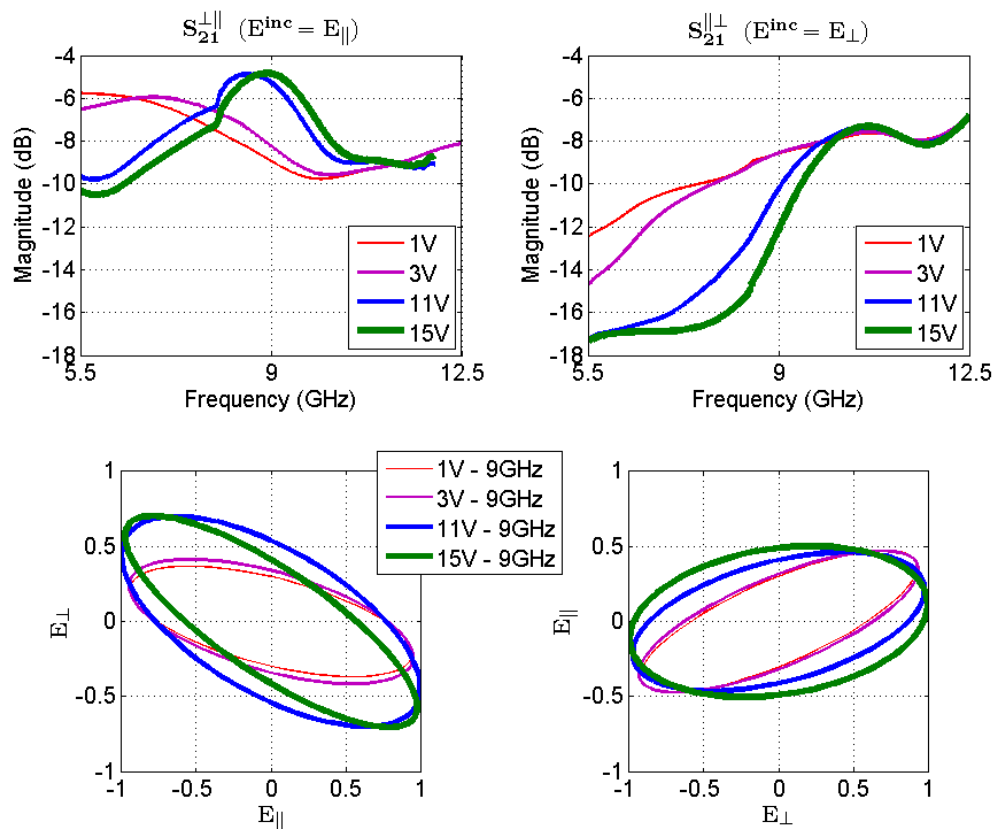
Figure 3.21: Measured performance: magnitude of cross-polarization transmission for axial and perpendicular incidence (top), cross-polarization contours demonstrating chiral tuning for axial and perpendicular incidence (bottom)

3.6 Conclusions

The design, fabrication and testing of an electronically tuned chiral PCB-helix composite was presented. A series of full-wave simulations demonstrate that the optimum configuration for the PCB consists of a one layer array of 9mm pitch rectangular helices spaced 6mm apart with a trace width of 0.3mm on a 3.175mm thick substrate of dielectric constant 2.2. More than one layer does not have a significant effect on the performance of the composite. The plasmonic response can be tuned electromagnetically by varying the capacitance of the circuit, up to a limit. This was demonstrated experimentally using the presented PCB. Cross-polarization transmission decreases with increasing voltage up to a certain frequency, depending on the incident polarization. The peak transmission frequency for perpendicular incidence can be tuned from 6 to 9GHz. Polarization contours confirm that the chirality of the board is affected by the increase in voltage. These results demonstrate the feasibility and effectiveness of creating electronically tunable chiral composite layers.

3.7 Acknowledgements

3.8 References

[1] Pendry, J.B., Holden, A.J., Stewart, and W.J., Youngs, I., "Extremely Low Frequency Plasmons in Metallic Mesostructures," *Phys. Rev. Lett.,* Vol. 76, No. 25, 17 June 1996.

[2] Smith, D.R., Vier, D. C., Padilla, Willie, Nemat-Nasser, Syrus C., Schultz, S., "Loop-Wire Medium for Investigating Plasmons at Microwave Frequencies," *App. Phys. Lett.,* Vol. 75, No. 10, 1425-1427, 6 September 1999.

[3] Wheeland, S., Amirkhizi, A., Nemat-Nasser, S., "Mechanically-tunable composite filter at low frequencies," *Proc. SPIE 7644*, 76441N (2010).

[4] Amirkhizi, A., Plaisted, T., Nemat-Nasser, S.C. and Nemat-Nasser, S., "Metallic Coil–Polymer Braid Composites: I. The Numerical Modeling and Chirality," ICCM–14, Society of Manufacturing Engineers, (2003).

[5] Huang, T.F., "Methodology of External Dual-band Printed Helix Design," *IEEE Antennas and Propagation Society, AP-S International Symposium (Digest)*, Vol. 1A, 458-461, 2005.

[6] Li, S.J., Zhou, Q., Xie, Y.J., Lei, Z.Y., "Theoretical and Experimental Investigation on PCB Helix Antenna," *J. of Electromagn. Waves and Appl.,* Vol. 21, No. 7, 877–887, 2007.

[7] Lin, C.C., Chang, Y.J., Chuang, H.R., "Design of a 900/1800 MHz dual-band LTCC chip antenna for mobile communications applications," *Microwave Journal*, Vol. 47, No. 1, 78-88, January 2004.

[8] Bayatpur, F., Wheeland, S., Amirkhizi, A.V., Nemat-Nasser, S., "An Electronically Tunable Chiral Layer with Agile Polarization Capabilities," submitted to *IEEE Microwave and Wireless Components Letters*, October 2012.

Chapter 4

Mechanically Tunable Polymer-Wire Composites

4.1 Introduction

Pioneering work on chirality at microwave frequencies was performed by Lindman in the early 1920s when he embedded helices of the same handedness in foam and observed the rotation of the plane of polarization [1]. Ever since, different elements exhibiting chiral characteristics have been proposed [2-4]. This chapter investigates chiral, uniaxial, bianisotropic elastomeric composites with mechanically tunable electromagnetic properties whose mechanical attributes have been maintained. Elastomeric composites with robust mechanically tunable EM properties may have application in skins or the flexible multifunctional elements in tensegrity structures.

Mechanically tunable composites have been investigated over the years for a variety of applications. Chiang et al [5] applied external stresses to a 2-D array of gold nano-particles embedded into polydimethylsiloxane (PDMS) to increase the distance between the particles. In this study, mechanical stress increased the surface plasmon frequency. Schmidt et al. [6] used an external stimulus to control the stiffness of an electrochemically responsive polymer nano-composite thin film. Blaszkiewicz et al. [7] applied uniaxial compression to a silicone rubber and piezoelectric ceramic electro-acoustic transducer, which tuned its resonant frequency. Truxal et al. [8] mechanically strained a PDMS grating in a MEMS device for photo-spectroscopic measurements, varying the wavelength of diffracted light. Tunability can extend to non-EM property control. Kennedy et al. [9] increased cellular fiber alignment and tuned porosity in a polyurethane scaffold for cardiac tissue by elongating the scaffold after fabrication.

The overall EM properties of composite materials have also sparked the interest of researchers over the years. Of particular interest are materials with plasmon frequencies in the microwave range [10-13]. Pendry et al. [10] demonstrated that achieving a relatively low plasmon frequency is possible using an array of thin metallic wires. In the microwave range, however, Smith et al. [11] noted the infeasibility of such an array and instead suggested using loop-wire elements. The loops achieve similar results with thicker wire and smaller unit cells, making the fabrication of such a material more viable.

A practical alternative to the loop-wire is the coiled wire helix [14]. Tuning the plasmon frequency is accomplished by changing the dimensions of the building blocks [12, 13]. The EM performance of an array of coils depends on the coil inner diameter, coil spacing, wire thickness, and pitch. Through a series of EM simulations, Nemat-Nasser et al. [13] determined pitch to have the greatest effect on performance. Schuil et al. [14] experimentally examined the effect of pitch on plasmon frequency with an array of coils in air. A 30% increase in pitch corresponded to an increase in plasmon frequency from 6.3 to 7.5GHz, thus demonstrating the effectiveness of such an array.

The present work seeks to develop a material with a deformation-induced change in chirality. To create such a composite, the metallic helices must be embedded in a matrix capable of supporting the large elastic deformation and shear stresses required to extend the coils and vary the pitch. Ceramics are brittle by nature and metals would reflect incident waves. In this case, the most logical choice is an elastomer, such as low durometer polyurethane. Furthermore, the elastomeric material protects the fragile coils against damage and permanent deformation due to unwanted contact and out-of-plane loads. Polyurethane elastomer has been used in a variety of applications, including biomedical research [15], and the creation of nanocomposites [16]. This broad span of utility is largely due to its material properties. A polyurethane chain forms when a

polyisocyanate reacts with a polyol. Polyurethanes exhibit high tear resistance, high toughness, and high elongation before break [17], as well as high elasticity and adhesion [18]. These properties make polyurethane an ideal material for use in a mechanically adjustable composite.

Using numerical and experimental tools, we aim to create an electromagnetically transparent polymer-helix composite with enhanced and tunable chirality, operating between 5.5–12.5GHz frequencies. Electromagnetic simulations are used to identify important design parameters for the elastomeric helix composite. A prototype sample of the helix composite is fabricated and characterized. To evaluate the tuning performance, the sample is stretched up to 30% and the chirality is measured as a function of helix length using the procedure described in Bayatpur et al. [19].

4.2 Electromagnetic Simulations

Chirality quantifies the level of coupling between the components of an EM wave while traveling through a material [1]. A chiral material, in general, is represented by four constitutive parameters in tensorial form through [20]:

$$\overline{D} = \bar{\bar{\varepsilon}}\overline{E} + \bar{\bar{\xi}} \tag{4.1}$$

$$\overline{B} = \bar{\bar{\mu}}\overline{H} + \bar{\bar{\zeta}}\overline{E} \tag{4.2}$$

where permittivity ε, electric polarization ξ, permeability μ and magnetic polarization ζ are 3×3 complex-valued matrices. A chiral medium couples the electric and magnetic components of the wave, thus rotating the wave polarization. As a result, the strength of the chirality depends on the amount of polarization rotation (cross-polarized transmission response): the higher the cross-polarized transmission, the larger the chirality.

The dielectric properties of the polyurethane are considered in designing the helices to achieve the desired EM frequency response. This is done through a full-wave simulation using Ansoft HFSS Finite Element solver. The simulation considers the polymer-helix as a periodic array of parallel, infinitely long helices embedded in a polyurethane matrix. The helix handedness remains constant throughout the array. Given its periodic structure, this composite can be simulated using the Periodic Boundary Condition setup in HFSS. The model unit cell is shown in Figure 4.1. This unit cell represents an array of helices that are periodic along $\hat{y}$, and their axes are parallel with $\hat{z}$.
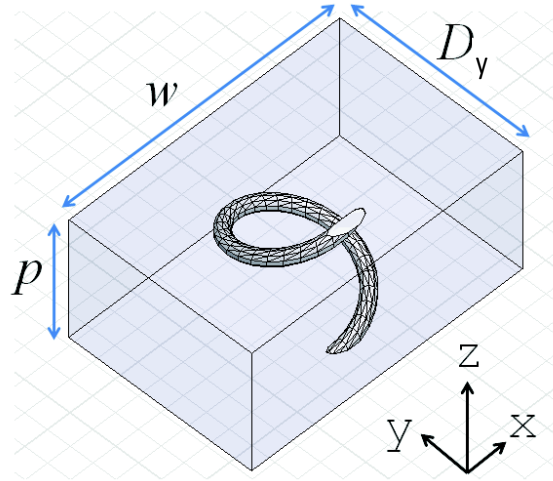
Figure 4.1: The polymer-helix composite unit cell consisting of one turn of one helix embedded in polyurethane. The array is periodic along $\hat{y}$ and $\hat{z}$.

A sensitivity analysis on the helices' pitch, diameter, spacing and the wire thickness was performed as a guide for fabrication. Through full-wave simulation, this analysis seeks enhanced cross-polarized transmission through the composite over the band of operation while keeping the total transmissivity high. In these simulations, the incident wave propagates in the x direction and is linearly polarized parallel to a single layer of composite with periodicity in the y- and z-directions. The nominal values for the unit cell dimensions, adopted from an earlier work [14],

are provided in Table 4.1. In this table, D_y is the spacing of the helices in the array, p is the helix pitch size, d is the helix inner diameter, t is the wire thickness, and w is the overall composite thickness.

Table 4.1: Helix Composite Design Parameters: Nominal Values (mm)

D_y	p	d	t	w
4	2.7	2	0.29	6

(a)   (b)
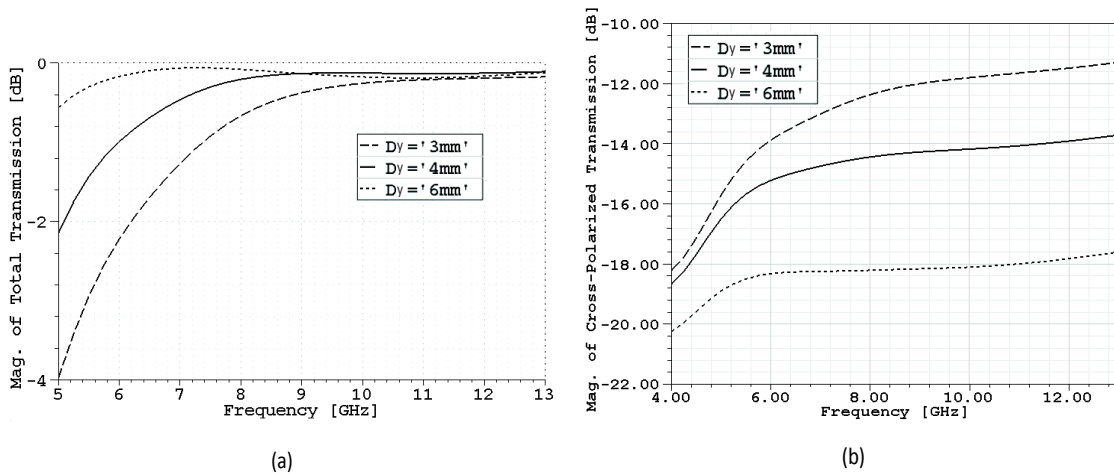
Figure 4.2: Reducing the spacing between the coils, D_y, reduces the total transmission at the lower end of the frequency range (a) while increasing cross-polarization transmission at all frequencies (b). The incident wave is polarized parallel to the helix.

Figure 4.2 shows the effect of spacing D_y on the transmission response. Increasing the spacing increases the total transmission, while the chirality decreases as the cross-polarization level goes down. This shows that the two desired EM properties are inversely correlated based on spacing. Thus a mid-range choice of spacing would be most suitable. Pitch is expected to have a major influence on the chirality. Chirality will increase with decreasing pitch size. This analysis shows that decreasing pitch indeed increases the cross-polarization level, but only up to a limit. This limit, shown in Figure 4.3, decreases by changing the pitch from 2.7 mm to 2 mm. A smaller pitch yields greater transmission.
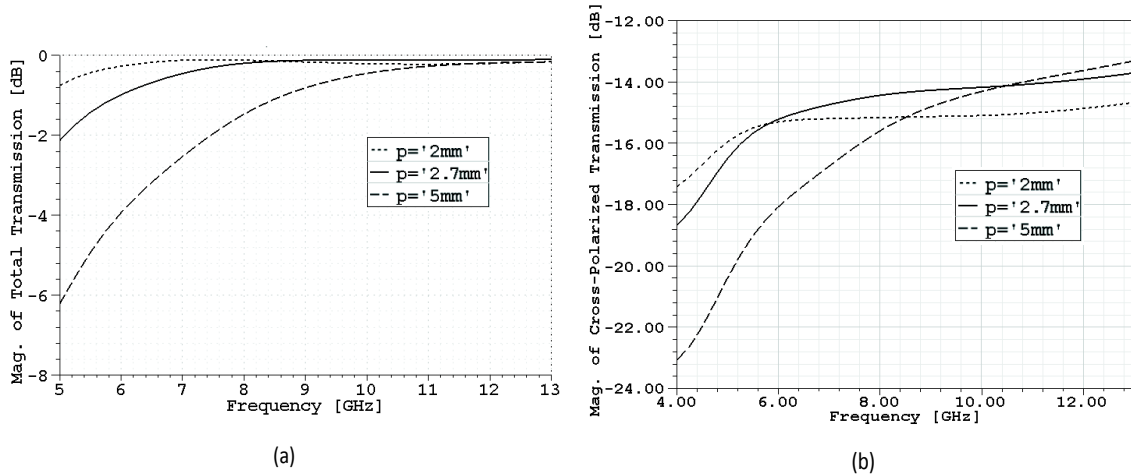
Figure 4.3: An increase in pitch, *p*, reduces the total transmission at the lower end of the frequency range (a) while causing an increase in cross-polarization transmission at higher frequencies (b). The incident wave is polarized parallel to the helix.

This full-wave analysis also includes other helix parameters; increasing the diameter enhances the total transmission, as shown in Figure 4.4.
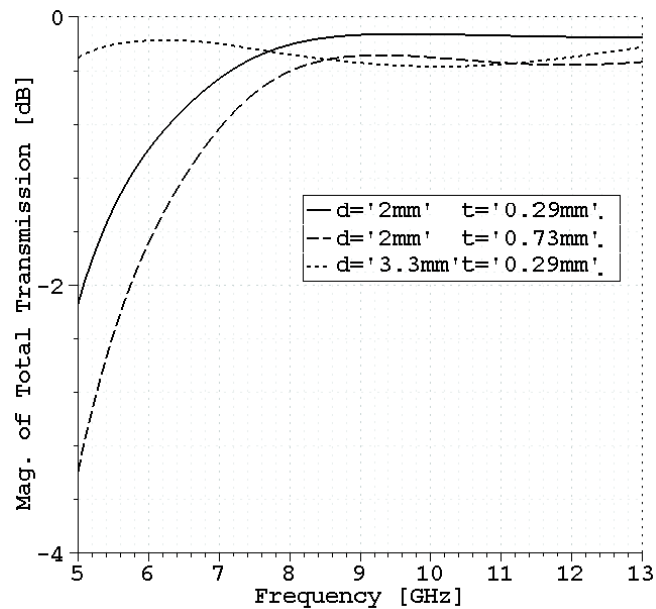
Figure 4.4: A larger helix inner diameter, *d,* increases the total transmission at lower frequencies while reducing it at higher frequencies. An increase in *t* reduces the total transmission. The incident wave is polarized parallel to the helix.

The choice of the diameter, however, is dependent on the spacing. Wire thickness has a lesser effect on transmission and chirality.

The analysis shows that spacing and pitch have a more pronounced effect on the EM properties than wire and composite thicknesses. The final design values are chosen after testing the mechanical performance of the design discussed in the fabrication section.

4.3 Mechanical Simulation

To better understand the interfacial interaction between the polymer matrix and the wire, the composite was modeled using an implicit finite element analysis. For simplicity, a single turn of copper wire was embedded inside a polyurethane matrix; see Figure 4.5 for geometric parameters. HyperMesh v10.0 was used to create the mesh. The coil shape was subtracted from the polyurethane block so the entire space is filled with a single material at any point. Both the block and the coil meshes were composed of tetrahedral elements with common elements using the same nodes. This allowed for both components to act as a unified composite.
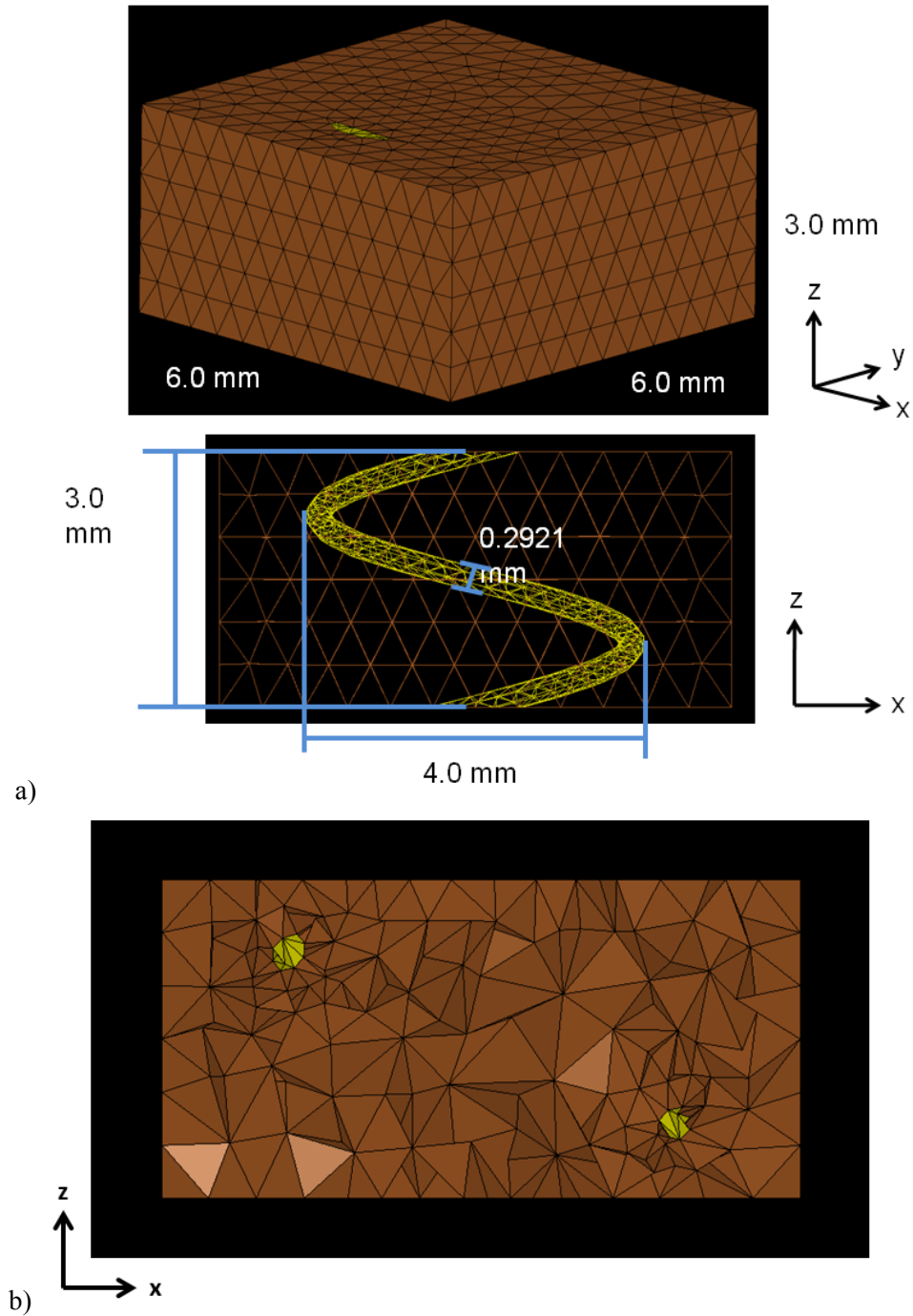
Figure4.5: a) Model unit cell parameters for block material (polyurethane) and coil (copper). b) Cut model showing placement of coil within polymer matrix.

Three separate boundary condition scenarios were modeled: fully periodic, periodic in x only, (traction-free on +y and −y faces) and non-periodic. Two corner nodes along the bottom

surface were constrained in x to prevent lateral movement. In the non-periodic case, the central node on the bottom surface was fixed in all directions, while a central edge node aligned in the y-direction was fixed in x and z. In all cases, the bottom surface was constrained in the z-direction. The nodes are set up in each file such that edges do not include corners and faces do not include edges or corners. This helps prevent over-constraining. The simulations ran for 500ms with a z-displacement prescribed on the top surface of 0.635mm for a strain rate of 76.2mm/min.
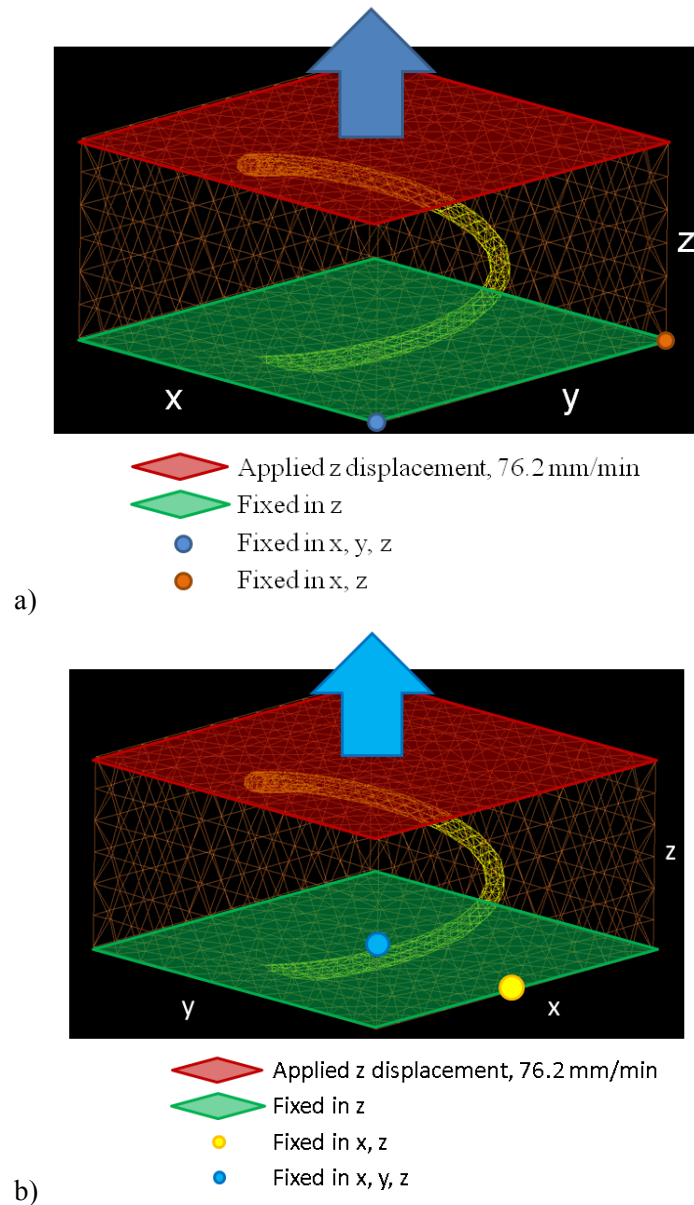
Figure4.6: Mechanical model constraints for a) periodic and b) non-periodic cases

The numerical solver LS-DYNA 971 was used to perform the simulation. The polyurethane was simulated using a hyper-elastic continuum rubber material model developed by Blatz and Ko [21]. Properties used in this model were calculated, assuming isotropy, from pure polyurethane tension tests. An elastic material model was used for the copper wire. A nonlinear implicit analysis with Broyden-Fletcher-Goldfarb-Shanno (BFGS) updates was implemented in the composite model for 500ms with a 0.01ms time step.

Graphical results confirm that stress is concentrated along the interface between the matrix and the coil. In each constraint case, the maximum von Mises stress occurs at the interface. A cut-away view of the block shows uniform stress elsewhere in the matrix; see Figure 4.7.

a)

b)

c)
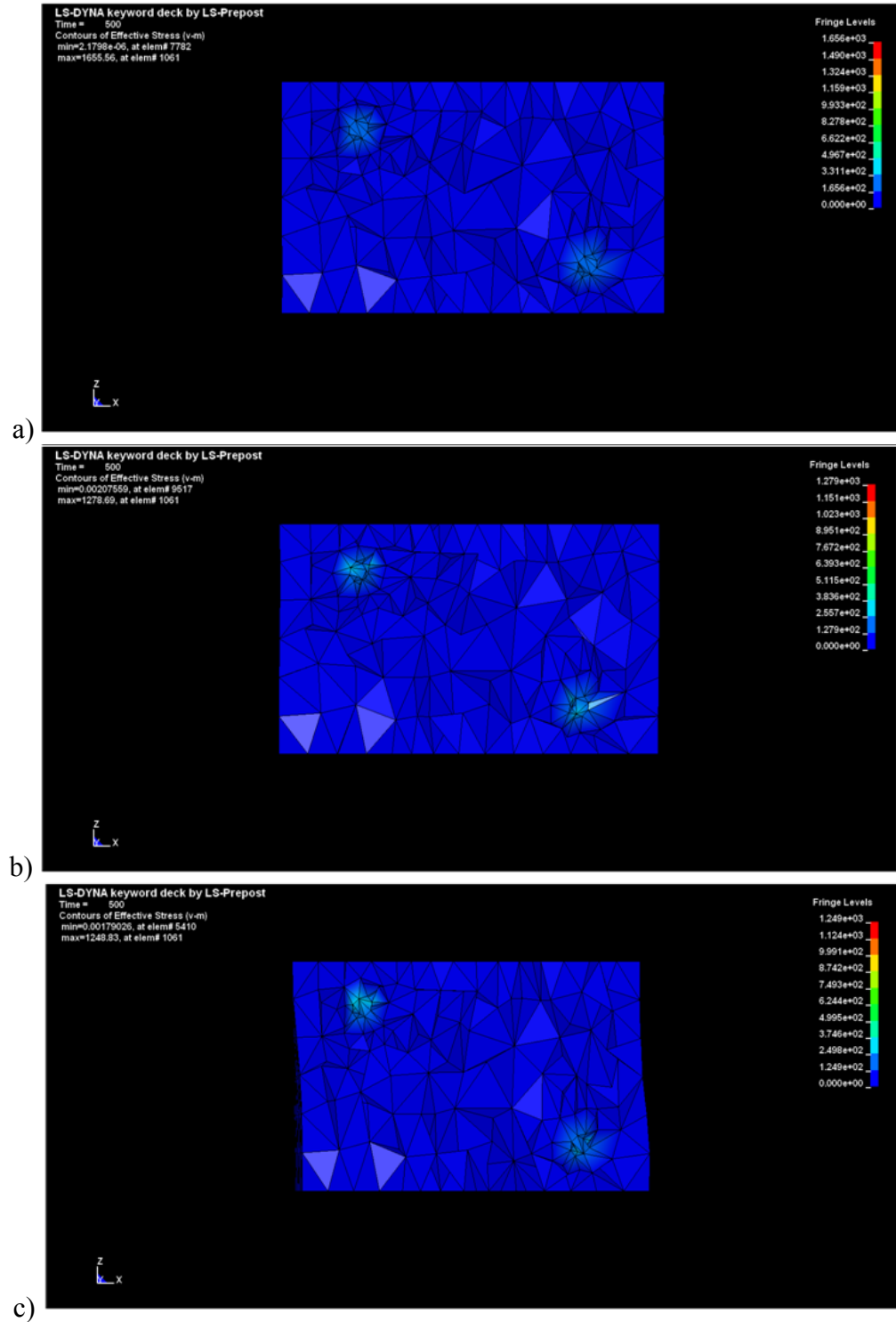
Figure 4.7: Cut-away views after 500ms showing von Mises stress for a) fully periodic, b) periodic in x, and c) non-periodic boundary condition cases.

The rigid body displacement, rigid body rotation and strain components in x and y for the top surface nodes in the non-periodic case can be calculated from the simulation using code developed in Mathematica (see Appendix). The top surface nodes include all four corners, all four edges, and interior surface nodes for the top face of the composite block. The code consists of a system with more equations than unknowns, requiring the use of a least squares fit of all possible solutions. Results are displayed in Table 4.2.

Table 4.2: Parameters extracted from non-periodic polymer-coil simulation

Parameter	Value: Top Face	Value: Bottom Face
u_x^t (rigid body disp. in x)	-0.0393265mm	-0.0103472mm
u_y^t (rigid body disp. in y)	0.00857995mm	0.00374415mm
Ω (rigid body rotation)	0.0390246 rad	0.0185212 rad
ε_{xx}	-0.0900853	-0.0892509
ε_{xy}	-0.00294222	0.00447661
ε_{yy}	-0.0743613	-0.0737

An interesting phenomenon with this composite is the interfacial interaction between the polymer matrix and the metallic coil. The force exerted by the coil onto the matrix results in rotation of the whole composite block. The amount of rotation observed in the model can be calculated through an energy-based approach. First, assume a square prismatic block of material with length L, shear modulus G_p, and side a centered at the origin. The change in axial rotation per unit length and the change in torque per unit length are given by:

$$\frac{d\varphi}{dz} = \frac{T}{G_p J_p} \, , \, \frac{dT}{dz} = -t \tag{4.3}$$

respectively, with the following boundary conditions:

$$\varphi = 0 \ at \ z = -\frac{l}{2}, \ T = 0 \ at \ z = \frac{l}{2} \qquad (4.4)$$

Integrating the torque equation and substituting the result into the first equation give:

$$\frac{d\varphi}{dz} = \frac{-t\left(z - \frac{l}{2}\right)}{G_p J_p} \qquad (4.5)$$

Upon integration of this equation, we rearrange to solve for t (torque per unit length). This is the amount of torque acting on the block.

$$t = \frac{2 G_p J_p \Delta\varphi}{l^2} \qquad (4.6)$$

From Newton's laws, the torque acting on the spring should be equal and opposite to the torque on the block with a change of coordinate system factor:

$$\bar{t}(\zeta) = -\frac{t}{\sin \alpha} \qquad (4.7)$$

where α is the angle between the wire and the horizontal. The angle of twist should be related to the angle of twist in the block by a similar factor, approximately:

$$\bar{\varphi}(\zeta) = \varphi(z) \sin \alpha \qquad (4.8)$$

The internal energy in the spring is the continuous sum of the energy at each segment of the spring, hence:

$$U = \int_{\frac{-l}{2 \sin \alpha}}^{\frac{l}{2 \sin \alpha}} \frac{1}{2} G_s J_s \bar{t} \bar{\varphi} \ d\zeta \qquad (4.9)$$

Substituting the previous expressions for $\bar{t}$ and $\bar{\varphi}$ and performing substitution of variables give:

$$U = -\frac{t^2 G_s J_s}{2 G_p J_p \sin \alpha} \int_{-\frac{l}{2}}^{\frac{l}{2}} \left(\frac{\left(z - \frac{l}{2}\right)^2}{2} - \frac{l^2}{2} \right) dz = \frac{t^2 G_s J_s l^3}{6 G_p J_p \sin \alpha} \qquad (4.10)$$

The above should equal the spring energy for a given displacement. Therefore, we have:

$$\frac{1}{2}k_s\delta^2 = \frac{t^2 G_s J_s l^3}{6 G_p J_p \sin\alpha} \tag{4.11}$$

Solving for δ yields:

$$\delta^2 = \frac{t^2 G_s J_s l^3}{3 k_s G_p J_p \sin\alpha} = \frac{4\Delta\varphi^2}{3 k_s l \sin\alpha} G_p J_p G_s J_s \tag{4.12}$$

which is the displacement of the spring with respect to the global coordinate system. Solving instead for the torque per unit length gives:

$$t^2 = \frac{3\delta^2 k_s \sin\alpha G_p J_p}{l^3 G_s J_s} \tag{4.13}$$

The values used with the above equations and the calculated results are given in Table 4.3. Italicized values indicate parameters input to the simulation. Notice that the angle of twist when central nodes are fixed along the bottom is not as accurate as the case with corners fixed.

Table 4.3: Input and calculated values for system torque

Parameter	Non-periodic, bottom corners fixed		Non-periodic, bottom center and edge center fixed	
	From Block	**From Spring**	**From Block**	**From Spring**
δ	*0.635mm*	0.724mm	*0.635mm*	0.995mm
ϕ	*0.0284 rad*	0.0249 rad	*0.039 rad*	0.0249 rad
t	0.1914Nm/m	0.1678Nm/m	0.2629Nm/m	0.1678Nm/m

In addition to the rotation, high shear stress exists at the interface due to the force exerted by the coil on the matrix. In the simulation, maximum shear stress is indeed observed at this boundary. Elsewhere in the matrix, the shear stress is essentially zero. The highest shear occurs at the interface along the top surface where the displacement is prescribed. High shear exists

throughout the interface, with moderate shear in the coil itself. Figure 4.8 graphically demonstrates this behavior.
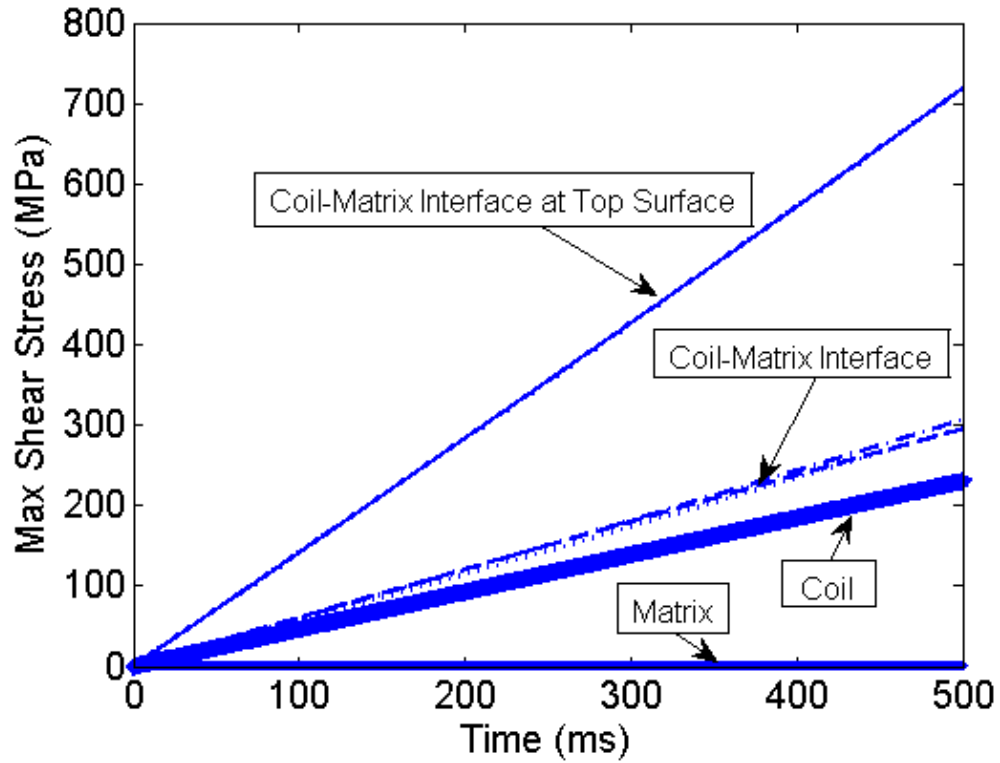
Figure 4.8: Comparison of maximum shear stress at the coil-matrix interface, coil, and matrix for the non-periodic boundary conditions case.

4.4 Fabrication

4.4.1 Sample Preparation

Each coil was wound using the parameters in Table 4.4 with a length, L, along the z-axis. These values were chosen based on the results of the EM simulations.

Table 4.4: Helix Composite Design Parameters: Finalized Values (mm)

D_y	p	d	t	w	L
4	4	2.4	0.29	6	310

Polyurethane served as the host medium for the helices. Smooth-On Inc VytaFlex 20, a polyurethane elastomer of durometer 20A, was prepared from two component which have been separately stirred and degassed for one hour. The components were combined and hand-mixed for three minutes and mixed under vacuum for another five minutes.

The coils were embedded in the polyurethane. A thin layer of polyurethane was first injected into the Teflon mold with a syringe. Next the coils were linearly positioned and held in place by wooden dowel pins. The remaining polyurethane was then added. This ensured the coils were near the center of the polymer thickness. Prior to curing, the samples were degassed for 15-20 minutes to eliminate air pockets and to improve the adhesion between the springs and the polymer. The samples were then cured overnight in an environmental chamber with the relative humidity maintained at 10%. The next day, the samples were post-cured in a 65°C oven for 4 hours. Figure 4.9(a) shows a completed unit cell: one layer of 13 helices.

Figure 4.9: Sample used in the mechanical and EM tests. (a) One unit consists of 13 coils. (b) 6 units in the test frame for a total area of 310 mm x 310 mm.

4.4.2 Mechanical Repeatability

After performing several tension tests, we determined that coils made with thin wire would allow for elastic deformation more reliably than thicker wire coils. The thick wire springs exert greater force on the polyurethane matrix prior to axial break due to its higher stiffness. This force translates to high shear stress at the interface between the wire and the matrix. As a result, delamination occurs much earlier than with the thin wire coils.

To demonstrate the repeatability of the composite, one sample was tested several times at the simulation strain rate of 76.2mm/min. The results of two tests, shown in Figure 4.10, demonstrate that the sample recovers its initial configuration even after being deformed near the

elastic limit of 50% axial strain, thus enabling mechanical tuning of the structure and its EM behavior.
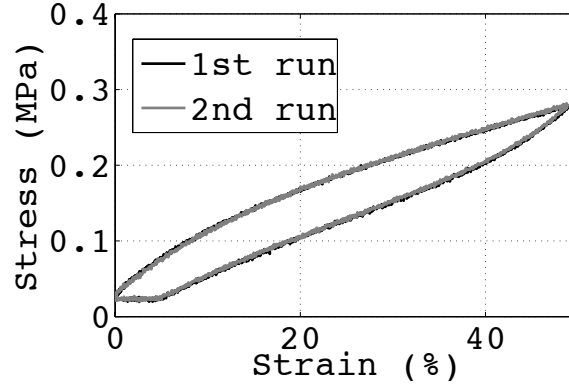
Figure 4.10: Axial stress-strain curve showing repeatability for one, 13-coil unit.

A comparison between the expected ε_{xx} and ε_{yy} based on the tension experiments to the values seen with the model presented in Section 4.3 can be seen using the Poisson effect:

$$\Delta d = -d\left(1 - \left(1 + \tfrac{\Delta L}{L}\right)^{-\nu}\right) \tag{4.14}$$

where d is the initial length of one side of the block (either x or y), L is the initial height of the block, ν is the Poisson ratio, ΔL is the change in height, and Δd is the change in either x or y. These two parameters, ε_{xx} and ε_{yy}, should be equal, assuming isotropy. The values generally agree with each other (Table 4.5):

Table 4.5: Comparison between strain components perpendicular to coil axis

	Model	**Experiment**
ε_{xx}	-0.0904	-0.0898
ε_{yy}	-0.0749	-0.0898

4.5   Chiral Helix-Polymer Composite: Measured Performance

Through a standard transmit/receive (TR) measurement setup, the EM properties of the finalized sample were measured. This setup includes two horn antennas connected to an Agilent 8510C Vector Network Analyzer. The antennas use microwave lenses located at their apertures to keep the radiating energy focused on the sample. The overall dimensions of the sample must be large enough to enclose the beam emanating from the antennas. With the sample placed equidistant between them at their focal point, the antennas collect the scattering parameters of the sample undergoing testing. Given the lens-antenna specifications, the beam area may be calculated quantitatively. For our TR setup this minimum area is nearly 1000cm^2 about 30cm from the antenna. The size of the assembled sample is big enough to cover this area; it consists of 6 units, each having 13 helices, covering a square area of 310 x 310mm; see Figure 4.9(b).

The magnitude of the cross-polarization transmission is given in Figure 4.11 for the unstretched setup and at 30% axial strain.
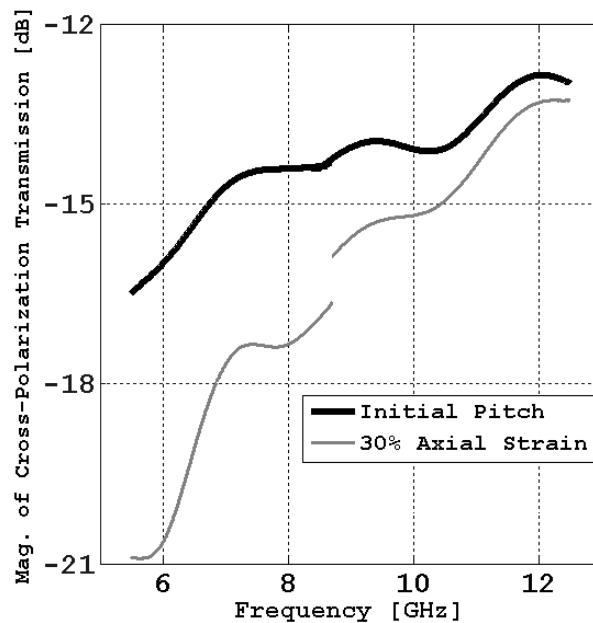
Figure 4.11: Cross-polarization transmission for initial and stretched composite tests. Note: discontinuity at 8GHz due to two separate test setups.

Two separate antenna configurations (5.5-8.7GHz, 8.7-12.5GHz) were used to collect data. The discontinuity between the two ranges is small given this change in test setup and represents the reliability and repeatability of our experimental protocol. The experimental results (Figure 4.11) must be compared with the results of the EM simulation (Figure 4.2(b)). They both represent the significant changes in chirality due to change in axial strain or pitch, shown in terms of raw cross-polarization transmission.

Given its scattering response, the uniaxially chiral slab material presented here is fully characterized for its constitutive parameters. These parameters are carefully retrieved using a process provided in an earlier work [19]. The extracted results for the sample at rest (without any strain) are shown in Figures 4.12(a) and 4.12(b), demonstrating an appreciable normalized chirality factor, $c\xi$". The retrieved permeability for both directions, parallel and perpendicular to the helices ($\mu'_{\parallel}, \mu'_{\perp}$), is ~1 (lower graphs in Figure 4.12(a)). The permittivity, however, well reflects the uniaxial behavior of the composite; the perpendicular permittivity ($\varepsilon'_{\perp}$) is ~3 on average in the band, while the axial response ($\varepsilon'_{\parallel}$) shows a turn-on frequency of ~7.1GHz (see the top, left graph in Figure 4.12(a)).

(a)

(b)
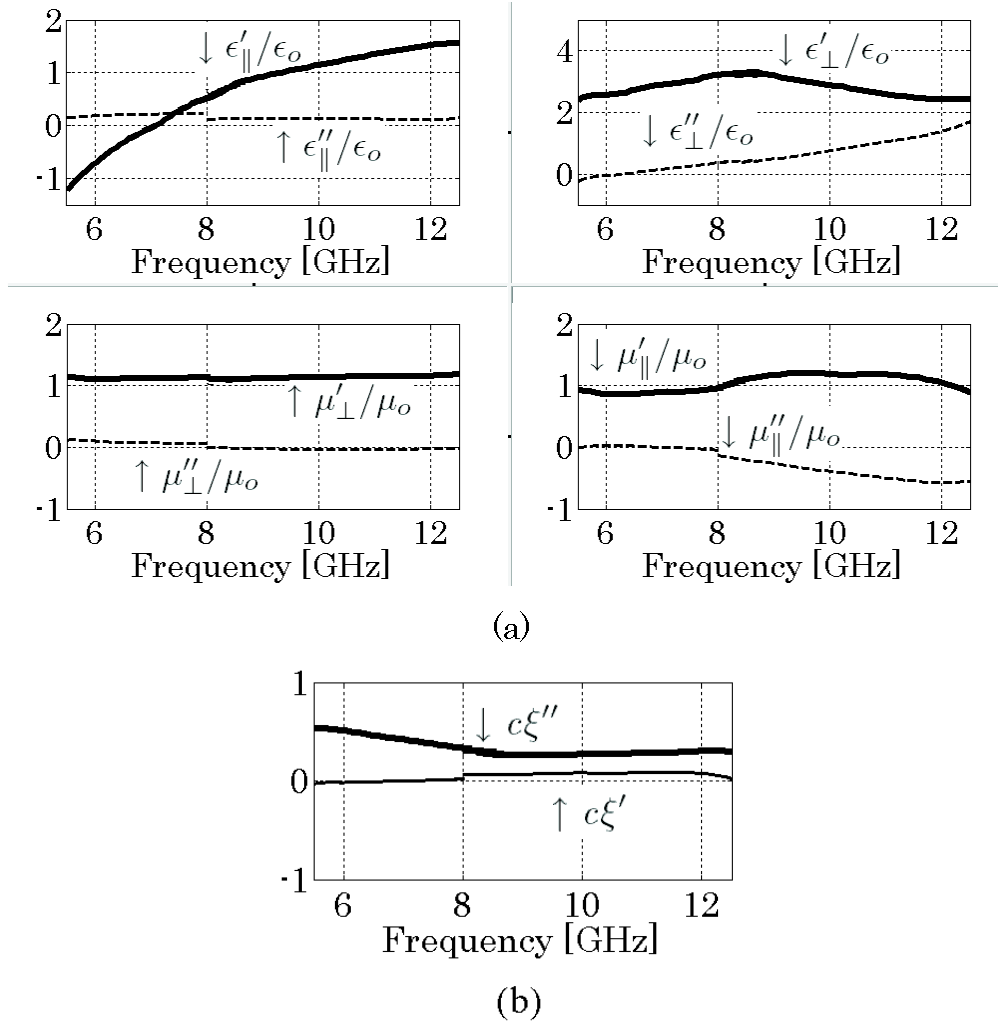
Figure 4.12: The constitutive parameters of the polymer-helix composite at zero strain.
(a) Axial and transverse permittivity ($\varepsilon_\parallel = \varepsilon_\parallel' - j\varepsilon_\parallel'', \varepsilon_\perp = \varepsilon_\perp' - j\varepsilon_\perp''$) and permeability ($\mu_\parallel = \mu_\parallel' - j\mu_\parallel'', \mu_\perp = \mu_\perp' - j\mu_\perp''$). (b) The axial chirality ($\xi = \xi' - j\xi''$), which is normalized to the speed of light in air, c.

In another test, the sample was axially stretched, and the EM measurement was performed for this length of the sample. The chirality variation over frequency generated as a result of the induced strain is provided in Figure 4.13. Up to ~18% tuning is achieved experimentally by a 30% increase in length and thus pitch. Based on previous work with achiral samples [14], it is expected that the constitutive parameters continuously change with pitch, within the range established here. The measured results well demonstrate the tuning capability of the polymer-helix composite.
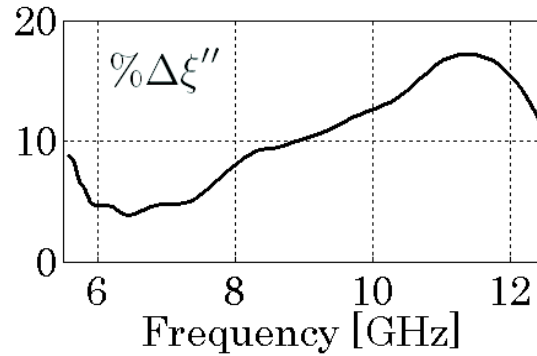
Figure 4.13: Percentage decrease in chirality (ξ'') due to 30% axial strain as compared to the un-stretched results shown in Figure 4.12.

4.6 Conclusions

A polymer-helix composite with mechanically adjustable chirality was presented. The initial geometry of the sample was selected using a full-wave EM sensitivity analysis. Samples were fabricated and mechanically tested to confirm a consistent recoverable strain limit of ~50%. Mechanical simulations numerically verified the results of the experiments while highlighting the interfacial interaction between the matrix and the coil. As expected, the matrix-coil interface experiences the greatest shear stress with the maximum value occurring at the end of the coil where strain is applied. EM tests performed on a larger sample confirm the qualitative results of the simulations. The chiral behavior can be tuned by about 18% through axial strain and frequency variation. This study suggests a method of creating mechanically tunable polymer-helix chiral composite filters for use at microwave frequencies.

4.7 Acknowledgements

The authors would like to thank Jon Isaacs and Robert Kim for their assistance in this study. In addition, the authors thank the University of California, San Diego (UCSD) Campus

Chapter 4, in part, appears in Smart Materials and Structures, 2013 by S. Wheeland, F. Bayatpur, A.V. Amirkhizi, and S. Nemat-Nasser, Vol. 22, 6pp. The dissertation author was the primary investigator and author of this paper.

4.8 References

[1] Lindell, I.V., Vitanen, A.J., Electromagnetic Waves In Chiral And Bi-Isotropic Media, Artech House Publishers, New York, 2002.

[2] Lakhtakia, A., Varadan, V.K., Varadan, V.V., Time-Harmonic Electromagnetic Fields in Chiral Media, Berlin: Springer-Verlag, 1989.

[3] Saadoun M.M.I., Engheta, N., "A Reciprocal Phase Shifter Using Novel Pseudochiral or Medium," Microwave and Opt. Tech. Lett., Vol. 5, 184-188, 1992.

[4] Leveque, G., Martin, O., "Tunable composite nanoparticle for plasmonics," Opt. Lett., Vol. 31, No. 18, 2750-2752, 15 September 2006.

[5] Chiang, Y.L., Chen, C.W., Wang, C.H., Hsieh, C.Y., Chen, Y.T., Shih, H.Y., Chen, Y.F., "Mechanically tunable surface plasmon resonance based on gold nanoparticles and elastic membrane polydimethlysiloxane composite," App. Phys. Lett., Vol. 96, 041904-1 - 041904-3, 26 January 2010.

[6] Schmidt, D.J., Cebeci, F.C., Kalcioglu, Z.I., Wyman, S.G., Ortiz, C., Van Vliet, K.J., Hammond, P.T., "Electrochemically Controlled Swelling and Mechanical Properties of a Polymer Nanocomposite," ACS Nano, Vol. 3, No. 8, 2207-2216, 22 July 2009.

[7] Blaszkiewicz, M., Newnham, R.E., Xu, Q.C., "Tunable transducers as smart materials," International Conference on Solid-State Sensors and Actuators, Digest of Technical Papers, TRANSDUCERS '91, 899-903, 24-27 June 1991.

[8] Truxal, S.C., Kurabayashi, K., Tung, Y.C., "Design of a MEMS Tunable Polymer Grating for Single Detector Spectroscopy," Int. J. Optomechatronics, Vol. 2, No. 2, 75-87, April 2008.

[9] Kennedy, J.P., McCandless, S.P., Lasher, R.A., Hitchcock, R.W., "The mechanically enhanced phase separation of sprayed polyurethane scaffolds and their effect on the alignment of fibroblasts," Biomater., Vol. 31, 1126-1132, 30 October 2009.

[10] Pendry, J.B., Holden, A.J., Stewart, and W.J., Youngs, I., "Extremely Low Frequency Plasmons in Metallic Mesostructures," Phys. Rev. Lett., Vol. 76, No. 25, 17 June 1996.

[11] Smith, D.R., Vier, D.C., Padilla, W., Nemat-Nasser, S. C., Schultz, S., "Loop-Wire Medium for Investigating Plasmons at Microwave Frequencies," App. Phys. Lett., Vol. 75, No. 10, 1425-1427, 6 September 1999.

[12] Amirkhizi, A., Plaisted, T., Nemat-Nasser, S.C. Nemat-Nasser, S., "Metallic Coil-Polymer Braid Composites: I. The Numerical Modeling and Chirality," ICCM-14, Society of Manufacturing Engineers, (2003).

[13] Nemat-Nasser, S., Nemat-Nasser, S.C., Plaisted, T., Starr, A., Amirkhizi, A.V., [BIOMIMETICS: Biologically Inspired Technologies], Edited by Yoseph Bar-Cohen, CRC Press, 309-341 (2005).

[14] Schuil, C.J., Amirkhizi, A.V., Bayatpur, F., Nemat-Nasser, S., "Composites with Mechanically Tunable Plasmon Frequency," Smart Mater. Struct. 20, 115012, 2011.

[15] Kanyanta, V., Ivankovic, A., "Mechanical characterization of polyurethane elastomer for biomedical applications," J. Mech. Behav. Biomed. Mater., Vol. 3, No. 1, 51-62, January 2010.

[16] Koo, J.H., Ho, W.K., Ezekoye, O.A., "Thermoplastic polyurethane elastomer nanocomposites: Morphology, thermophysical, and flammability properties," J. Nanomater., Vol 2010, 2010.

[17] ASM Engineered Materials Handbook, 2nd ed., ASM International: 2002.

[18] Elastomers, Polyurethane. Encyclopedia of Materials: Science and Technology, 1st ed., Pergamon: Oxford, 2001, p 2472.

[19] Bayatpur, F., Amirkhizi, A.V., Nemat-Nasser, S., "Experimental Characterization of Chiral Uniaxial Bianisotropic Composites at Microwave Frequencies," IEEE Trans. Microw. Theory Tech., In Press, Dec. 2011.

[20] Kong, J.A., Electromagnetic wave theory, Cambridge, MA: EMW Publishing, 2000, Chapter 2.

[21] Blatz, P.J., and Ko, W.L., "Application of Finite Element Theory to the Deformation of Rubbery Materials," Trans. Soc. of Rheology, Vol. 6, 223-251, 1962.

Chapter 5

Soft-Focusing in a Thin Wire Array

5.1 Introduction

There are many materials that exhibit an electrical plasmonic response. For these materials the electric permittivity is negative within certain frequency bands. However, few materials possess an equivalent magnetic response, i.e. negative magnetic permeability. Pendry et al. [1] and Smith et al. [2] theoretically and experimentally presented examples of microstructured materials with such magnetic properties. The combination of negative electrical permittivity and magnetic permeability was postulated by Veselago [3] to produce a negative index of refraction. The negative-index metamaterials and negative refraction were first established in 2000 [2]. This has stimulated considerable research activities ever since. One fascinating phenomenon observed in such media is the reversal of Snell's law. Pendry [4] presented an ideal design for a perfect lens with the index of refraction, n, equal to -1 and the characteristic impedance, Z, equal to the free space characteristic impedance, $+Z_0$. Even though such a design may be impractical, the general idea of using negative refraction to control a wave path has attracted considerable attention. Shen et al. [5] developed a compact lens in the visible spectrum using Pendry's theory. One notable example in the microwave regime was a flat, gradient lens, which showed focusing of close to +7dB over incident power in the absence of the lens [6]. This demonstrates that negative-index materials could be used to focus microwave signals without the need for curved lenses.

The present work discusses a simple method for producing an anisotropic indefinite slab expected to produce similar soft-focusing. First, the theoretical prediction of soft-focusing in

indefinite or hyperbolic media is explained. Next, the experimental work is discussed. We conclude by presenting results, which illustrate the focusing pattern in a variety of configurations.

5.2 Theory

The majority of the microstructured metamaterials manufactured so far have been anisotropic. Smith et al. [7] noted that many interesting phenomena exist in cases where the diagonal components of the permittivity and permeability tensors have opposite signs. These materials are termed indefinite, since the permittivity tensor, $\boldsymbol{\varepsilon}$, (or the permeability tensor, $\boldsymbol{\mu}$) is neither positive- nor negative-definite. Consider a slab of such a material with transverse-magnetically polarized wave vectors that lie in an indefinite plane (i.e. the 12-plane for which the product of the corresponding permittivity tensor components, $\varepsilon_{11}\varepsilon_{22}$, is less than 0). When the group velocity is normal to the wave vector, the isofrequency curve is hyperbolic. An ellipse is seen in positive- or negative-definite media [8-14] (see Figure 5.1).
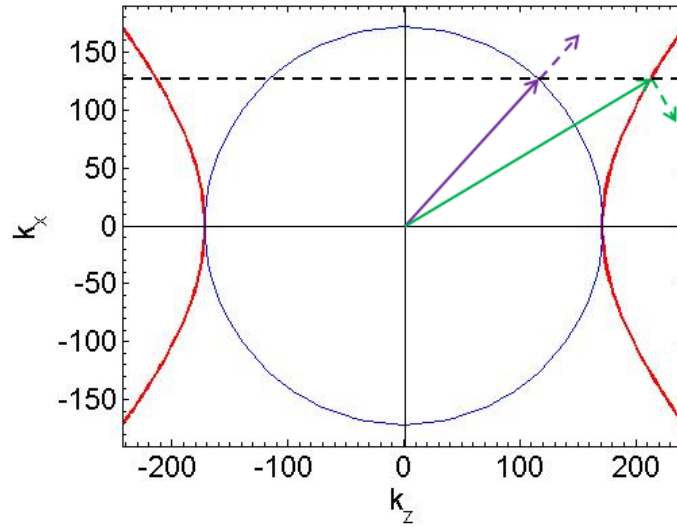
Figure 5.1: Isofrequency curves showing the distinction between free space (circle), where $\varepsilon_x>0$ and $\varepsilon_z>0$, and the indefinite medium presented in this paper (hyperbola), where $\varepsilon_x>0$ and $\varepsilon_z<0$. In both cases, z is in the direction of propagation. In indefinite media, waves are refracted negatively, as indicated by the green arrows. The solid vectors show the wave vector, while the dashed arrows show the group velocity direction. A similar calculation can be made when the magnetic permeability tensor is indefinite, as discussed in Smith et al[14], reproduced courtesy of The Electromagnetics Academy.

Such a shape of the isofrequency curve will result in negative refraction, a reversal of Snell's law, without the need for negative index. Consider the x-component of the group velocity and phase velocity vectors in (Figure 5.1). In a positive-definite medium, these components have the same sign while in an indefinite media they have the opposite sign. Smith et al. [14] illustrated this phenomenon with a ray-tracing diagram that was confirmed experimentally with split-ring resonators (SRR), which are magnetically indefinite media. In that study, the magnetic permeability along the axis of propagation was negative while all other diagonal components of the tensor were positive. Shallow incidence angles through the indefinite slab yielded similar focusing to that seen in the negative index slab. Liu et al. [9] and Fang et al. [10] demonstrated this numerically with finite element simulations. Focusing was seen with both ellipsoid and single-sheeted hyperboloid dispersion surfaces. Furthermore, Cheng and Ciu [11] developed a Luneburg microwave lens using the indefinite magnetic permittivity tensor produced in an array

of I-shaped unit cells. Expanding upon these ideas, Salandrino and Engheta [12] also explored far-field scanless microscopy using metamaterial crystals. Simply put, hyperbolic dispersion in the indefinite slab results in partial focusing of a point source radiation on the opposite side of the slab [8-14] (see Figure 5.2).
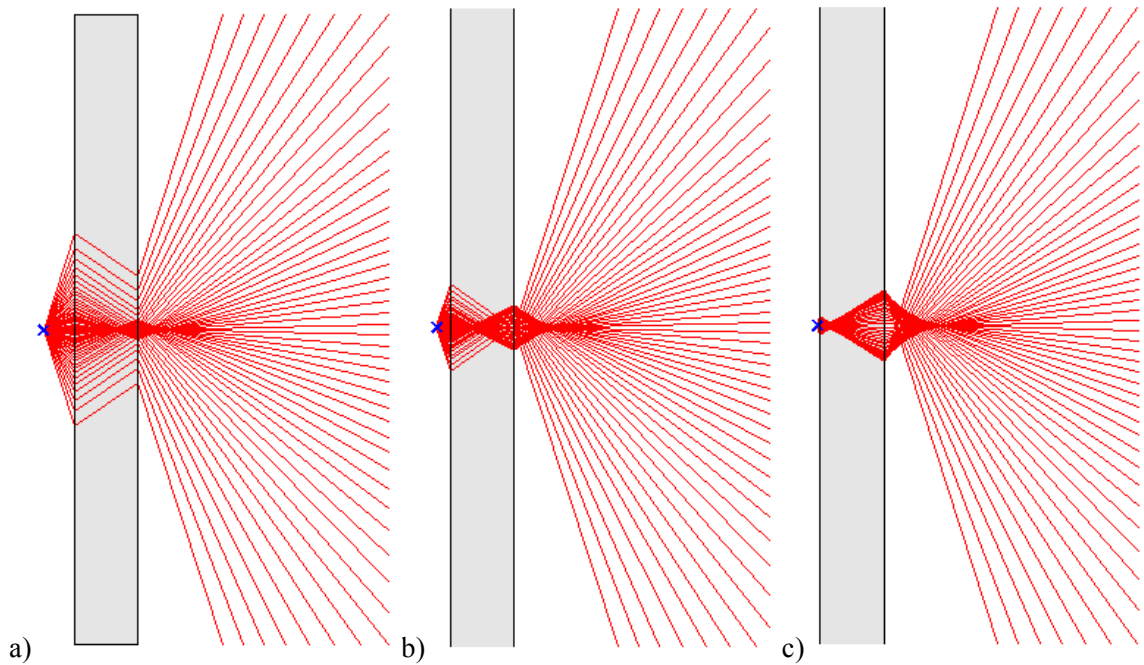
Figure 5.2: Indefinite slab showing partial focusing from a point source placed at a distance of a) 7.35 cm, b) 3.5 cm, and c) 0.8 cm from the sample surface. This is an extension of the picture shown in Smith et al[14]. In our work, a TM point source, rather than a TE one, is used. The Matlab program to create these images was kindly provided by Costas Soukoulis and Thomas Koschny from Iowa State University, reproduced courtesy of The Electromagnetics Academy

For a square lattice array of simple elements with spacing d and self-inductance L, the overall dielectric constant κ of the composite will have the following Drude-Lorentz form with k being the base material's dielectric constant [1,15,16]:

$$\kappa = \varepsilon_{overall}/\varepsilon_0 = k - \frac{f_p^2}{f^2} \tag{5.1}$$

where

$$f_p = \frac{\omega_p}{2\pi} \tag{5.2}$$

is the plasmon frequency,

$$\omega_p^2 = \frac{1}{d^2 L \varepsilon_0} \tag{5.3}$$

When the elements of the array are very thin straight wires of infinite length,

$$L = \frac{\mu_0}{4\pi} \left\{ \ln \left[\frac{d^2}{\pi r^2} \right] - 1 \right\} \tag{5.4}$$

A graph showing the relationship between the frequency and κ is shown in Figure 5.3 [18].
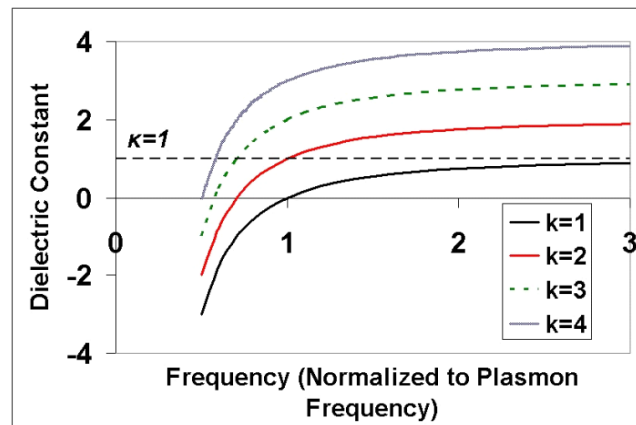
Figure 5.3: Graph of the relationship between dielectric constant and frequency for various values of k, reproduced courtesy of The Electromagnetics Academy.

This permittivity form is valid only for an electric field polarized parallel to the wires. When the electric field is normal to the wires, the overall dielectric constant will be very close to that of the base composite, since the amount of metal is small. Therefore, if the wires are embedded in air and/or very low permittivity materials (such as Styrofoam), one may find a frequency at which $\varepsilon_{pw} = -\varepsilon_{nw} = -\varepsilon_0$. Here pw and nw denote polarizations parallel and normal to the wires, respectively. This frequency is simply:

$$f_{hyp} = f_p / 2^{1/2} \tag{5}$$

We can extend the theoretical prediction by simulating a slab of such material in HFSS. Using equations (1)-(4), the slab is homogenized and placed in an air box with radiation boundary conditions. Normal to the wires, $\kappa_{nw} = 1$ due to the very small volume fraction of metal embedded in the Styrofoam. A lumped port placed on a ring of copper provides the excitation for the system. This antenna mimics a point source. As shown in Figure 5.4, the homogenized indefinite slab partially focuses the incident plane waves. In the figure, transmission is normalized with respect to measured values without the slab.

a)   b)
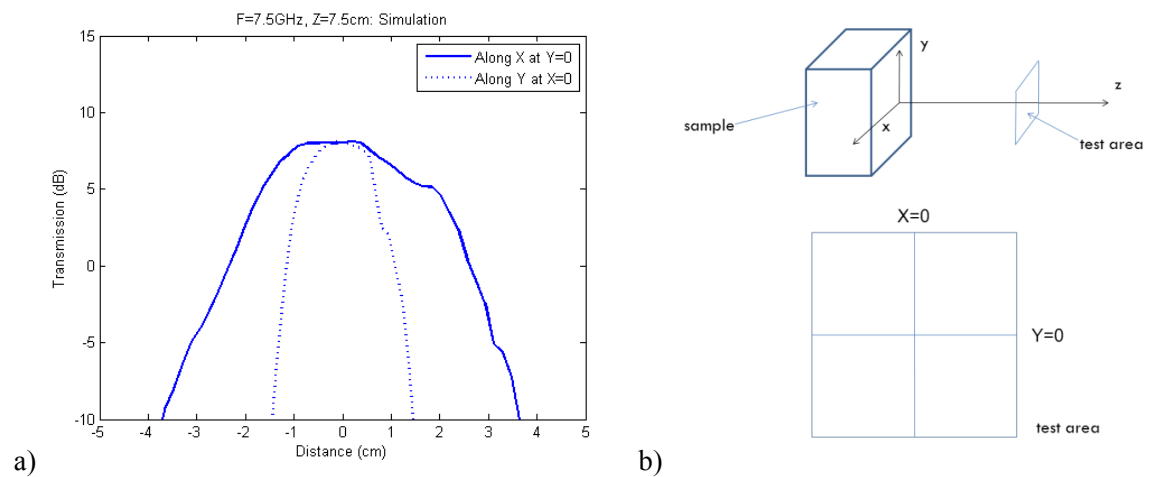
Figure 5.4: a) Full-wave simulation of partially focused transmission through simulated homogeneous slab with $\varepsilon_x = \varepsilon_y = \varepsilon_0$ and $\varepsilon_z = -\varepsilon_0$ and b) configuration schematics of the simulation, reproduced courtesy of The Electromagnetics Academy.

The plasmonic response can be further predicted using a parameter retrieval procedure similar to the one described in Nemat-Nasser et al. [17], though this is outside the scope of this paper. Previous work in this area indicates the expected plasmonic curve is similar to the theoretical prediction discussed here.

5.3   Methodology

5.3.1   Sample

We constructed the sample for this series of experiments out of two rectangular Styrofoam blocks and 0.3065mm diameter brass wires. The Styrofoam blocks each measured 50mm thick and 350mm wide, placed so the total thickness measured 147mm; see Figure 5.5. The wires were 147mm long, arranged in an array with a lattice spacing of 6.35mm. This was maintained by a series of holes in the Styrofoam blocks. Two square panels of Plexiglas with large circular holes were placed on either side of the Styrofoam for support. These were secured with threaded nylon rods, as shown in Figure 5.5. Given this lattice geometry and using equations (1)-(4), soft focusing was expected at $f_{hyp} = 8.18$ GHz.
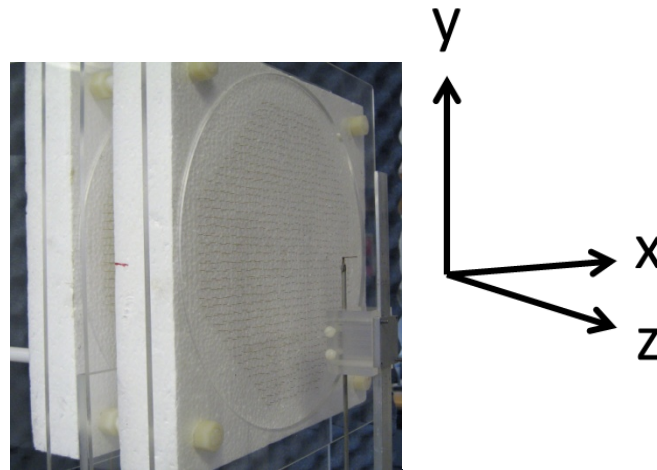
Figure 5.5: Styrofoam and 12-gauge brass wire sample secured with Plexiglas and threaded nylon rods, reproduced courtesy of The Electromagnetics Academy

5.3.2   Test Setup

To approximately create a TM point source and probe, two single-loop circular antennas with diameter 11mm and wire thickness 0.29mm were made. The antennas were arranged such that the linear coaxial feed was between the sample and the loop at all times, as shown in Figure

5.6. This configuration was chosen during calibration since it resulted in cleaner measurements among all considered configurations. The stationary transmitter antenna was placed at a distance of 7.35cm, 0.8cm, or 3.5cm from the center of the loop to the back surface of the sample. The receiver antenna scanned the space in the x, y, and z directions, starting from 4cm, 2.3cm, or 1.7cm, respectively, from the front surface of the sample. The scanning was carried out by an XYZ automated scanning robot and controlled using LabVIEW. Each antenna was connected to the Agilent 8510C VNA where the signals originated and returned. At each point in the scanned space, the VNA measured the transmission component of the scattering matrix, S_{21}, for the requested frequency values. The data was then collected into a file on the controlling computer. Figure 5.6 shows the test setup. In their magnetic counterpart study, Smith et al [14] scanned a two-dimensional space with TE probes, using aluminum plates and absorbing material.
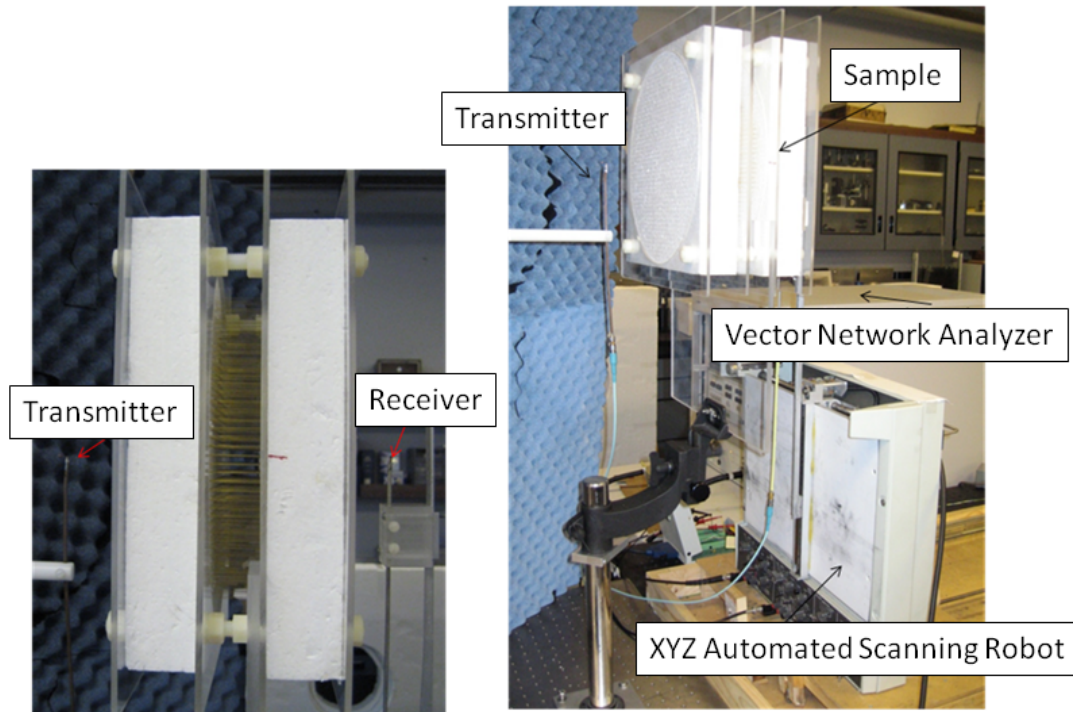
Figure 5.6: Test setup showing placement of two point source antennas around the sample with the robot and VNA – computer with LabVIEW not shown, reproduced courtesy of The Electromagnetics Academy

5.3.3 Calibration

The basic calibration of the experiment was done by running the robot without the sample in place to find the estimated transmission/power pattern due to the presence of the source. Even though the efficiency of the loop antenna TM source/probe is not ideal, we observed that in the spatial volume of interest the source increased the measured transmission coefficient from -75dB to an average of -41dB given a power input of 15dBm. This power input value was used throughout the tests. Also, within the nominal 10x10x10cm box of measurement, the scanning setup was able to consistently stop at the same XYZ grid of 9.7x9.5x10.4cm.

5.3.4 Experimental Procedure

Each test was run with an averaging factor of 16 and 1% smoothing with an absolute power output of 15dBm. In the x and y direction, the robot scanned either a 10x10cm area over 201 or 401 frequency points or a 20x20cm area over 401 frequency points within a range of 7-9GHz. This provided a detailed set of data. The tests were carried out with and without the sample in place. The VNA sent the signals to the transmitter antenna. Using a LabVIEW module, the VNA-measured signal from the receiver antenna was collected in a file readable by MATLAB. In other words, the data sent to MATLAB represents S_{21}, where ports 1 and 2 represent the transmitter and receiver antennas, respectively. This procedure was repeated at each stop of the receiver probe.

5.4 Results

Three sets of tests are presented in this section, corresponding to the three transmitting antenna locations mentioned previously. The results shown in Figure 5.7 and Figure 5.8 are

obtained when the center of the transmitter loop is placed 7.35cm from the back surface of the sample. Figure 5.9 and Figure 5.10 show the experimental results when this distance is changed to 0.8cm and 3.5cm, respectively.

As can be seen from the first set of tests in Figure 5.7, the strongest focusing occurs at 7.6GHz at a distance of 7.5cm from the sample surface. A distinction can be made between the data with the sample and without the sample. It should be noted that the signals focused at a lower frequency than the theoretically predicted 8.18GHz. A possible explanation for this discrepancy is discussed in the next section.
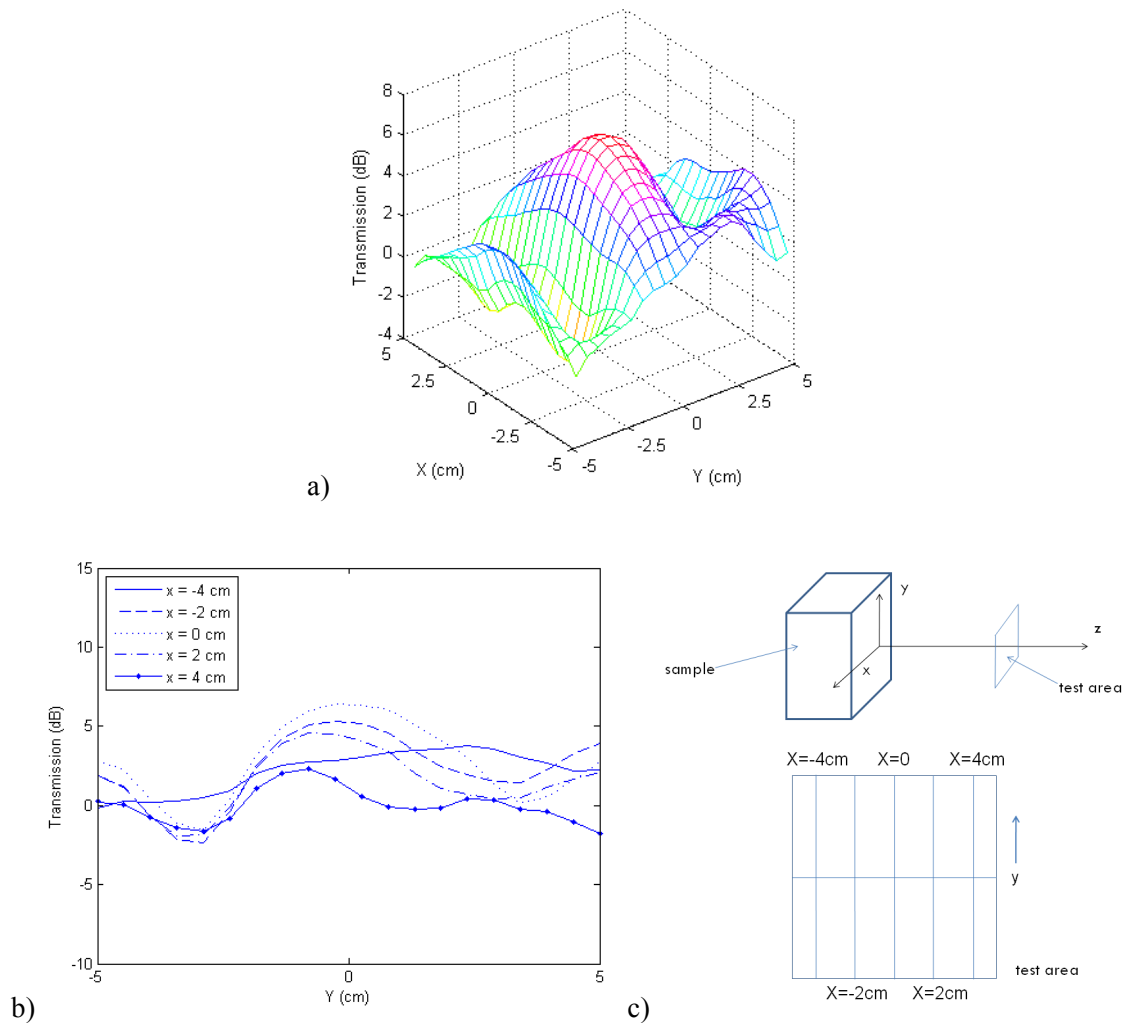
Figure 5.7: Transmitter antenna at 7.35 cm distance. a) Power gain compared to the measurement without the sample as a function of X and Y at Z=7.5 cm (from sample surface) and F=7.6 GHz; b) power gain as a function of Y at Z=7.5 cm and F=7.6 GHz at various values of X; c) schematics of the test configuration, reproduced courtesy of The Electromagnetics Academy.

Illustrated in Figure 5.8a, the strongest focusing is seen at 7.5cm from the front surface of the sample. This is consistent with the predicted focal distance, which is based on the distance between the transmitter antenna and the back surface of the sample.
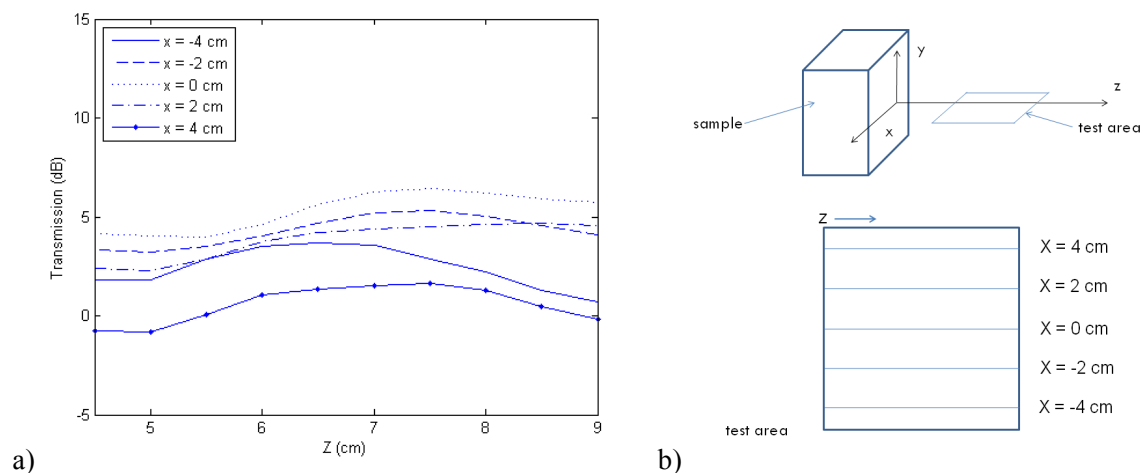
Figure 5.8: Transmitter antenna at 7.35 cm distance. a) Power gain compared to the measurement without the sample as a function of Z for various values of X at F=7.6 GHz and Y=0 cm; b) schematics of the test configuration, reproduced courtesy of The Electromagnetics Academy.

The second set of tests with the transmitter antenna at a distance of 0.8cm from the back surface show similar results, as can be seen in Figure 5.9. The focal point in this case is very close to the front surface of the sample, as expected from a ray tracing analysis of this configuration.
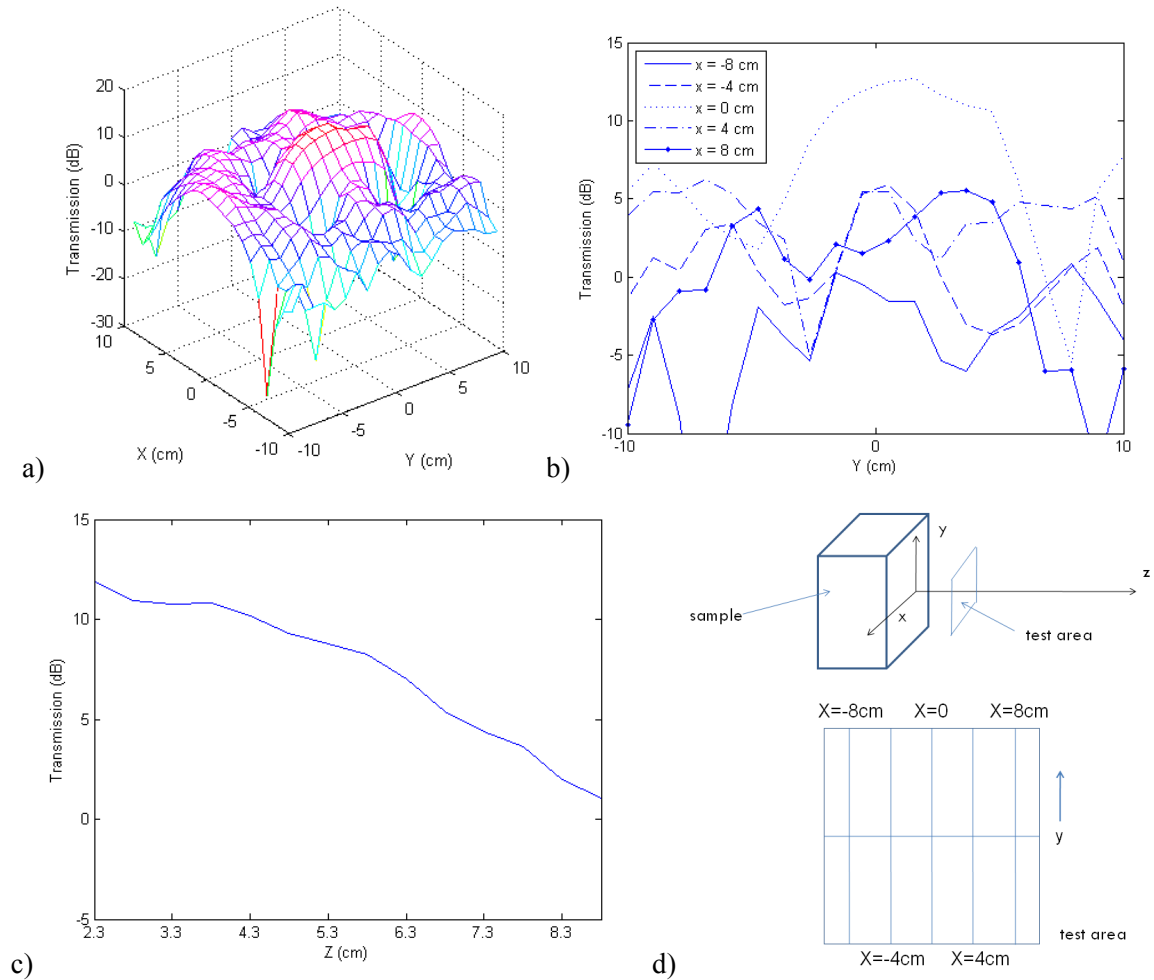
Figure 5.9: Transmitter antenna at 0.8 cm distance. a) Power gain compared to the measurement without the sample as a function of X and Y at Z=2.3 cm (from sample surface) and F=7.6 GHz; b) power gain as a function of Y at Z=2.3 cm and F=7.6 GHz at various values of X; c) power gain at the center of the sample over the z-axis; d) schematics of the test configuration, reproduced courtesy of The Electromagnetics Academy.

A final set of tests with the transmitter antenna at a distance of 3.5cm from the back surface of the sample show similar results as well, see Figure 5.10. Notice the slight focusing towards the center of the sample and towards the top.
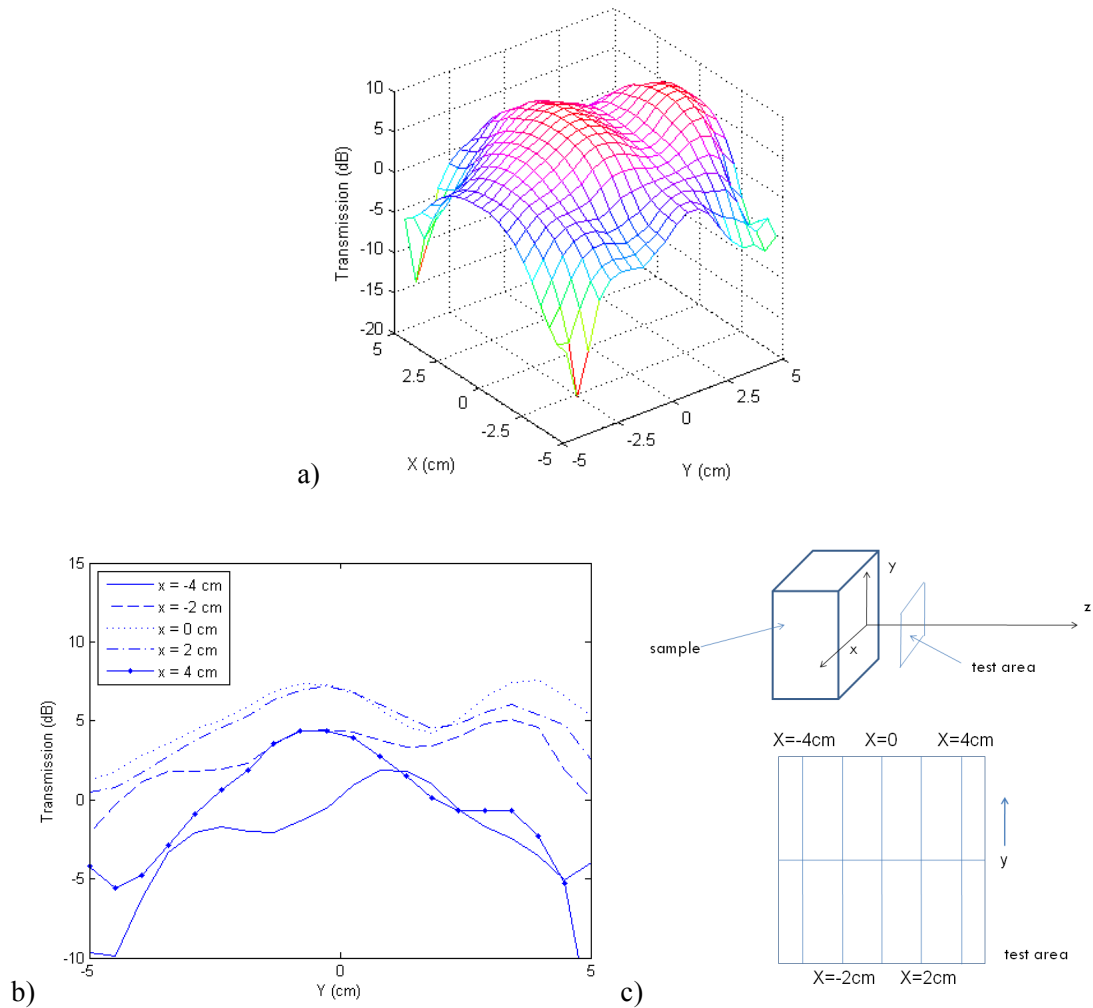
Figure 5.10: Transmitter antenna at 3.5 cm distance. a) Power gain compared to the measurement without the sample as a function of X and Y at Z=3.7 cm (from sample surface) and F=7.6 GHz; b) power gain as a function of Y at Z=3.7 cm and F=7.6 GHz at various values of X; c) schematics of the test configuration, reproduced courtesy of The Electromagnetics Academy.

5.5 Conclusions

In the earlier study with the SRR lattice, Smith et al [10] found that an imperfect focal spot is achieved with $\mu_y<0$, $\mu_x>0$. The results of the experiments presented here show that the sample decreases the amount of signal loss at predicted soft-focus spots compared to that without the sample in place. Though this difference is small, the sample focuses at a 7.5cm distance from the front surface in the 7.35cm test at a frequency of 7.6GHz with softer focusing at other

frequencies and distances. This frequency is lower than the calculated value of 8.18GHz. Equations (1)-(4) assume an infinitely long wire, whereas finite lengths of wire were used in the sample. The effect of finite length of the wires on the mobility of electrons is most pronounced at the interface between the wire array and the air. It is possible that within a distance inside the wire array comparable to the wavelength of interest, the overall dielectric constant may not be estimated by equations (1)-(4). This is due to the strong capacitive effect of the ends of the wires. A theoretical model for this may be possible to derive, but it is outside the scope of this experimental paper. Better antenna construction could allow for higher transmission coefficients. Also, enclosing the whole system in an anechoic chamber would reduce ambient reflection and could improve signal reception. In summary, these results demonstrate hyperbolic focusing within media with an indefinite dielectric constant tensor.

5.6 Acknowledgements

5.7 References

[1] Pendry JB, Holden AJ, Stewart WJ, Youngs I. Extremely Low Frequency Plasmons in Metallic Mesostructures. Physical Review Letters. 1996; 76(25): 4773-6.

[2] Smith DR, Padilla WJ, Vier DC, Nemat-Nasser SC, Schultz S. A Composite Medium with Simultaneously Negative Permeability and Permittivity. Physical Review Letters. 2000; 84: 4184-7.

[3] Veselago VG. The Electrodynamics of Substances with Simultaneously Negative Values of ε and μ. Soviet Physics USPEKHI. 1968; 10(4): 509.

[4] Pendry JB. Negative Refraction Makes a Perfect Lens. Physical Review Letters. 2000; 85(18): 3966-9.

[5] Shen NH, Foteinopoulou S, Kafesaki M, Koschny T, Ozbay E, Economou EN, Soukoulis CM. Compact planar far-field superlens based on anisotropic left-handed metamaterials. Physical Review Letters B. 2009; 80: 115123.

[6] Driscoll T, Basov DN, Starr AF, Rye PM, Nemat-Nasser S, Schurig D, Smith DR. Free-space microwave focusing by a negative-index gradient lens. Applied Physics Letters. 2006; 88: 081101-1 –3.

[7] Smith DR, Schurig D. Electromagnetic Wave Propagation in Media with Indefinite Permittivity and Permeability Tensors. Physical Review Letters. 2003; 90(7): 077405-1 –4.

[8] Smith DR, Kolinko P, Schurig D. Negative refraction in indefinite media. Journal of the Optical Society of America B: Optical Physics. 2004; 21(5): 1032-42.

[9] Liu H, Lv Q, Luo H, Wen S, Shu W, Fan D. Focusing of vectorial fields by a slab of indefinite media. Journal of Optics A: Pure and Applied Optics. 2009; 11: 105103.

[10] Fang A, Koschny T, Soukoulis CM. Optical anisotropic metamaterials: Negative refraction and focusing. Physical Review Letters B. 2009; 79: 245127.

[11] Cheng, Q, Cui, TJ. Planar microwave lens based on complementary metamaterials. Antennas and Propagation Society International Symposium (APSURSI), 2010 IEEE. 2010: 1-4.

[12] Salandrino A, Engheta N. Far-field subdiffraction optical microscopy using metamaterial crystals: Theory and simulations. Physical Review Letters B. 2006; 74: 075103.

[13] Schurig D, Smith DR. Spatial filtering using media with indefinite permittivity and permeability tensors. Applied Physics Letters. 2003; 82(14): 2215-7.

[14] Smith DR, Schurig D, Mock JJ, Kolinko P, Rye P. Partial focusing of radiation by a slab of indefinite media. Applied Physics Letters. 2004; 84(13): 2244-6.

[15] Nemat-Nasser SC, Amirkhizi AV, Padilla WJ, Basov DN, Nemat-Nasser S, Bruzewicz D, Whitesides G. Terahertz plasmonic composites. Physical Review E. 2007; 75: 036614-1 –7.

[16] Smith DR, Vier DC, Padilla WJ, Nemat-Nasser SC, Schultz S. Loop-wire medium for investigating plasmons at microwave frequencies. Applied Physics Letters. 1999; 75(10): 1425-7.

[17] Nemat-Nasser S, Nemat-Nasser SC, Plaisted T, Starr A, Amirkhizi AV. Multifunctional Materials. BIOMIMETICS: Biologically Inspired Technologies. Bar-Cohen Y, ed. CRC Press. 2005: 309-341.

[18] Marshall S, Amirkhizi AV, Nemat-Nasser S. Focusing and negative refraction in anisotropic indefinite permittivity media. In: Bar-Cohen Y, Wallmersperger T, editors. Electroactive Polymer Actuators and Devices (EAPAD) 2009. Proceedings of the International Society for Optical Engineering; 2009; San Diego.

Chapter 6

Mechanically Tunable GRIN Lens

6.1   Introduction

Metamaterials have unique capabilities. Most notably, the bulk properties of these materials can be precisely controlled to achieve a desired effect. This ability lends itself well to the development of gradient index (GRIN) lenses. A lens can be designed to focus incident radiation without the need for a curved surface. Such a lens would minimize the spherical aberration associated with conventional lenses.

Previous work has shown that these designs can be developed for terahertz and microwave frequencies with very small lens thicknesses. The microstructure of such lenses generally includes split- or closed-ring resonators to control the magnetic permeability [1-3], though researchers have also developed slit- or groove-based lenses [4-8]. A variety of materials have been studied for use in such composites, including liquid crystals [9], photonic crystals with electro-thermal actuators [10,11], polydimethylsiloxane membranes with actuation elements [12], gold and stainless steel [5,6,8], as well as copper plate [7]. Indefinite media can be used in the design of soft-focusing lenses [3,13-16].

Through the use of coils in the microstructure, an additional degree of freedom, namely pitch, is introduced into the material. This provides the advantage of enabling mechanical tuning of the material properties [17-19]. Through extension of these coils, the permittivity and thus the refractive index can be fine-tuned to achieve focusing at a different frequency and/or location. This work serves to demonstrate the feasibility and utility of creating a mechanically tunable

GRIN lens using conductive coils. Such a composite extends the application of gradient index lenses in the microwave regime, while also establishing novel mechanisms for mechanical tuning.

This chapter presents work on focusing via GRIN lenses using conductive copper coils. The gradient of material properties required to achieve optimized focusing and the extent of this effect is calculated through an anisotropic Hamiltonian ray-tracing analysis. Full-wave simulation further highlights the focusing behavior. With the proper initial gradient determined, a composite is created using coils of opposite handedness to eliminate chiral effects. Such effects may be explored in future work.

6.2   GRIN Lens Design: Electromagnetic Simulation

The design of the tunable lens can be divided into two parts: the relationship between material index and performance, and the relationship between material index and pitch. The former is determined through a ray-trace analysis conducted in MATLAB. The ideal index gradient is then translated into a corresponding pitch gradient through the use of a full-wave HFSS analysis.

6.2.1   Relationship between Material Index and Performance

6.2.1.1   Ray-Trace Theory

Ray tracing examines the behavior of individual waves at an interface as well as the behavior inside a medium. The low computational complexity required for this type of model allows for rapid iteration of design choices and enables quick optimization. Although the discrete nature of ray-tracing ignores higher-order effects, it efficiently provides guidance for the expected

performance of the test sample. The present case, adapted from Sluijter et al. [20], considers an anisotropic material with a gradient index of refraction in two dimensions. A MATLAB code is developed from the theory and included in the Appendix for reference.

First, consider Maxwell's equations in the general form with no electric charge:

$$\nabla \times \boldsymbol{E} = -\frac{\partial \boldsymbol{B}}{\partial t} \tag{6.1}$$

$$\nabla \times \boldsymbol{H} = \frac{\partial \boldsymbol{D}}{\partial t} \tag{6.2}$$

$$\nabla \cdot \boldsymbol{D} = 0 \tag{6.3}$$

$$\nabla \cdot \boldsymbol{B} = 0 \tag{6.4}$$

For a linear medium, $\boldsymbol{D}$ and $\boldsymbol{B}$ have the following form:

$$\boldsymbol{D} = \varepsilon_0 \varepsilon \boldsymbol{E} \tag{6.5}$$

$$\boldsymbol{B} = \mu_0 \mu \boldsymbol{H} \tag{6.6}$$

where ε and μ denote relative permittivity and permeability, respectively, and ε_0 and μ_0 denote the permittivity and permeability of free space. If we assume quasi-plane waves for the electromagnetic fields and combine the previous two equations, we can write the eikonal equation as:

$$ME = 0 \tag{6.7}$$

where:

$$M = \boldsymbol{k} \times \boldsymbol{k} \left(\frac{1}{\mu}\right) + \varepsilon \tag{6.8}$$

and $\boldsymbol{k}$ is the wave vector. A trivial solution to the eikonal equation is avoided by setting the determinant of M equal to zero. The resulting matrix is termed the Hamiltonian, or H. For a uniaxial dielectric material in an orthogonal coordinate system with an index of refraction defined by:

$$n^2 = \begin{bmatrix} n_\perp^2 & 0 & 0 \\ 0 & n_\parallel^2 & 0 \\ 0 & 0 & n_\perp^2 \end{bmatrix} \tag{6.9}$$

where $n^2 = \varepsilon\mu$ and with a wave vector matrix defined as:

$$K = k_o \begin{bmatrix} -(k_y^2 + k_z^2) & k_x k_y & k_x k_z \\ k_x k_y & -(k_x^2 + k_z^2) & k_y k_z \\ k_x k_z & k_y k_z & -(k_x^2 + k_y^2) \end{bmatrix} \tag{6.10}$$

the Hamiltonian reduces to:

$$H = k_0(k_x^2 + k_y^2 + k_z^2 - \varepsilon_\perp \mu_\parallel)(k_y^2 \varepsilon_\parallel \mu_\perp + (k_x^2 + k_z^2 - \varepsilon_\parallel \mu_\perp)\varepsilon_\perp \mu_\parallel) \tag{6.11}$$

The material fabrication technique dictates that the material be uniform in the y-direction, so we can assume the waves remain in the xz-plane, H can therefore be simplified to obtain:

$$H = k_0(k_x^2 + k_z^2 - \varepsilon_\perp \mu_\parallel)(k_x^2 + k_z^2 - \varepsilon_\parallel \mu_\perp)\varepsilon_\perp \mu_\parallel \tag{6.12}$$

Equation 6.12 can be further reduced by considering the polarization of the incident ray. Due to the nature of the coils, we require a nonzero E-field in the y-direction. Hence the Hamiltonian reduces to:

$$H = (k_x^2 + k_z^2 - \varepsilon_\parallel \mu_\perp)k_0 \tag{6.13}$$

The ray trajectories can then be calculated using Hamilton's equations, which relate the position and wave energy of each path:

$$\frac{d\mathbf{r}}{d\tau} = \nabla_k \mathrm{H} \tag{6.14}$$

$$\frac{d\mathbf{k}}{d\tau} = -\nabla_r \mathrm{H} \tag{6.15}$$

where $\mathbf{r}$ is the position vector; $\mathbf{k}$ is the wave vector; H is the Hamiltonian given above; and τ parameterizes the ray path.

The extent of the focusing ability depends on the phase of the wave. If the waves are in-phase, constructive interference enhances the focus. Destructive interference occurs when the waves are out of phase and cancel. Equations 6.14 and 6.15 can be transformed to calculate the change in phase by multiplying each right-hand side by a constant, α. Its value should be chosen such that $d\tau = d\varphi$ at the final boundary. This simplifies the calculation of the overall phase change as the phase shift is accumulated along the path of the ray. Given the dispersion relation and the phase change within the material, α takes the following value:

$$\alpha = \pm \frac{1}{|\mathrm{H}_o||\nabla_k \mathrm{H}_e||k|} \tag{6.16}$$

where the subscripts o and e correspond to the ordinary and extraordinary parts of the Hamiltonian (H = $\mathrm{H}_o\mathrm{H}_e$), respectively. The insertion of equation 6.16 into equations 6.14 and 6.15 results in a revised set of Hamilton's equations:

$$\frac{d\mathbf{r}}{d\phi} = \pm \frac{\nabla_k \mathrm{H}_e}{|\nabla_k \mathrm{H}_e||k|} \tag{6.17}$$

$$\frac{d\mathbf{k}}{d\phi} = \mp \frac{\nabla_r \mathrm{H}_e}{|\nabla_k \mathrm{H}_e||k|} \tag{6.18}$$

Note that H_o cancels in the transformation from $d\tau$ to $d\varphi$.

By expanding the right-hand sides of these equations, taking the derivative with respect to Cartesian coordinates, and simplifying, the above system can be rewritten as:

$$\frac{dx}{d\phi} = \pm \frac{k_x}{\varepsilon_{||}\mu_{\perp}k_0} \tag{6.19}$$

$$\frac{dy}{d\phi} = 0 \tag{6.20}$$

$$\frac{dz}{d\phi} = \pm \frac{k_z}{\varepsilon_{||}\mu_{\perp}k_0} \tag{6.21}$$

$$\frac{dk_x}{d\phi} = \pm \frac{1}{2\varepsilon_{||}\mu_{\perp}k_0} \frac{d(\varepsilon_{||}\mu_{\perp})}{dx} \tag{6.22}$$

$$\frac{dk_y}{d\phi} = 0 \tag{6.23}$$

$$\frac{dk_z}{d\phi} = \pm \frac{1}{2\varepsilon_{||}\mu_{\perp}k_0} \frac{d(\varepsilon_{||}\mu_{\perp})}{dz} \tag{6.24}$$

Once the waves exit the material, each ray will travel a different distance with respect to the central ray before reaching the focal plane. This shift can be calculated for each ray. The phase of one ray shifts by a factor of $k_0\Delta l$ assuming free space. The total phase change is then the sum of the shift accumulated in the material and the shift in free space. A value near zero indicates a stronger focus.

In order to solve this system of differential equations, we must consider the boundaries of the material. For the initial boundary between two media with impedance mismatching, incoming waves are reflected and refracted at the surface. The transmitted and reflected rays can be calculated using:

$$\boldsymbol{k}^{inc} \times \hat{\boldsymbol{n}} = \boldsymbol{k}^{ref} \times \hat{\boldsymbol{n}} = \boldsymbol{k}^{trans} \times \hat{\boldsymbol{n}} \tag{6.25}$$

$$H(\boldsymbol{k}^{trans}) = 0 \tag{6.26}$$

$$H_s(\boldsymbol{k}^{ref}) = 0 \tag{6.27}$$

where the superscripts indicate the incident wave, reflected wave and transmitted wave, respectively, H_s is the Hamiltonian of the surrounding medium, and H is the Hamiltonian of the lens. The second boundary condition results in two possible solutions for the z-component of the transmitted wave, one of which results in a non-zero electric field in the y-direction. Since the current setup requires a non-zero y-component of the electric field, this particular value for the transmitted wave was selected. In the code, reflected rays are neglected.

Inside the material, Hamilton's equations are solved at each step along each ray path. The MATLAB code employs ode45, a Runge-Kutta solver, to carry out this task.

Hamilton's equations do not apply outside the material as the surrounding medium is free space. Therefore, the equations must only be solved within the material. To ensure that this is the case, an event is created for each boundary. In MATLAB's ode45 implementation an event is triggered once the value parameter changes signs. This informs the program that the ray has exited the medium and to stop solving Hamilton's equations.

At the final interface between two non-impedance-matched media, the waves are either reflected back into the material or transmitted and refracted. The transmission and reflection are calculated in a similar manner to the first boundary:

$$\boldsymbol{k}^{inc}\times\widehat{\boldsymbol{n}} = \boldsymbol{k}^{ref}\times\widehat{\boldsymbol{n}} = \boldsymbol{k}^{trans}\times\widehat{\boldsymbol{n}} \tag{6.28}$$

$$\mathrm{H}\big(\boldsymbol{k}^{ref}\big) = 0 \tag{6.29}$$

$$\mathrm{H}_s\big(\boldsymbol{k}^{trans}\big) = 0 \tag{6.30}$$

Once the position and wave vector are known at the final boundary, the ray is projected into the final medium. Since the surrounding material is free space, this projection is valid. In code form only real rays are plotted and the ray vector is created.

This code is then repeated for each ray. A simple script can be written to run this code over a range of initial x values. For the purposes of this work, a code was written to optimize the initial gradient for maximum focal strength and minimum phase shift. While longer focal distances showed stronger focal points due to the phase shift, test setup limitations required focusing within one meter from the lens.

6.2.1.2 Lens Design Finalization

Initial ray-tracing results demonstrated the feasibility of designing a lens using a material with an index of refraction gradient along its width, i.e. the x-direction. The results indicated that while a focal spot may be detected, the strength of that focus may be weak due to phase shifts. The work presented in this section attempts to minimize phase shift by incorporating a z-component into the gradient profile from the previous section.

By extending the gradient profile, we have more control over the permittivity in the material. The focal strength can be enhanced by reducing the phase shift at the focus. This is accomplished using the method described in the previous section. The introduction of spatial variance in the z-direction allows for finer adjustment of the permittivity, which should increase the strength of the focus.

For an effective lens, the gradient profile must provide maximum focal strength for the sample dimensions. Due to experimental space restrictions, the profile should focus incident waves within 1m of the sample surface. The optimal profile must also limit pitch variation, as spring constant increases with pitch. A large variance could inhibit axial strain uniformity. Using the code developed in the previous section along with these requirements, the initial gradient profile is then optimized to the following gradient (shown in Figure 6.1a):

$$\varepsilon_{\parallel}\mu_{\perp} = n^2 = 0.8801\left(1 - \frac{x^2}{0.047263} + \frac{z^2}{0.012905}\right) \tag{6.31}$$

For a slab of material measuring 174mm in the x-direction and 72mm in the z-direction, this profile focuses 47.4% of incident rays with near-zero phase shift at 12.1GHz (see Figure 6.1b-c). Naturally, a thicker block (i.e. larger z-dimension) could yield a near-perfect theoretical focus due to greater flexibility in the gradient. Such a block, however, would be too awkward for presentation and practical purposes.

To demonstrate the tunability of the lens, the fabricated sample will be uniformly stretched up to 30% axial strain. At this maximum stretch level, the gradient index profile at 10.6GHz becomes:

$$\varepsilon_{\parallel}\mu_{\perp} = 0.7391\left(1 - \frac{x^2}{0.0235} + \frac{z^2}{0.006416}\right) \tag{6.32}$$

This profile has a predicted focal strength of 44.0% with near-zero phase shift.

Initial Index Gradient

(a)

(b)

(c)
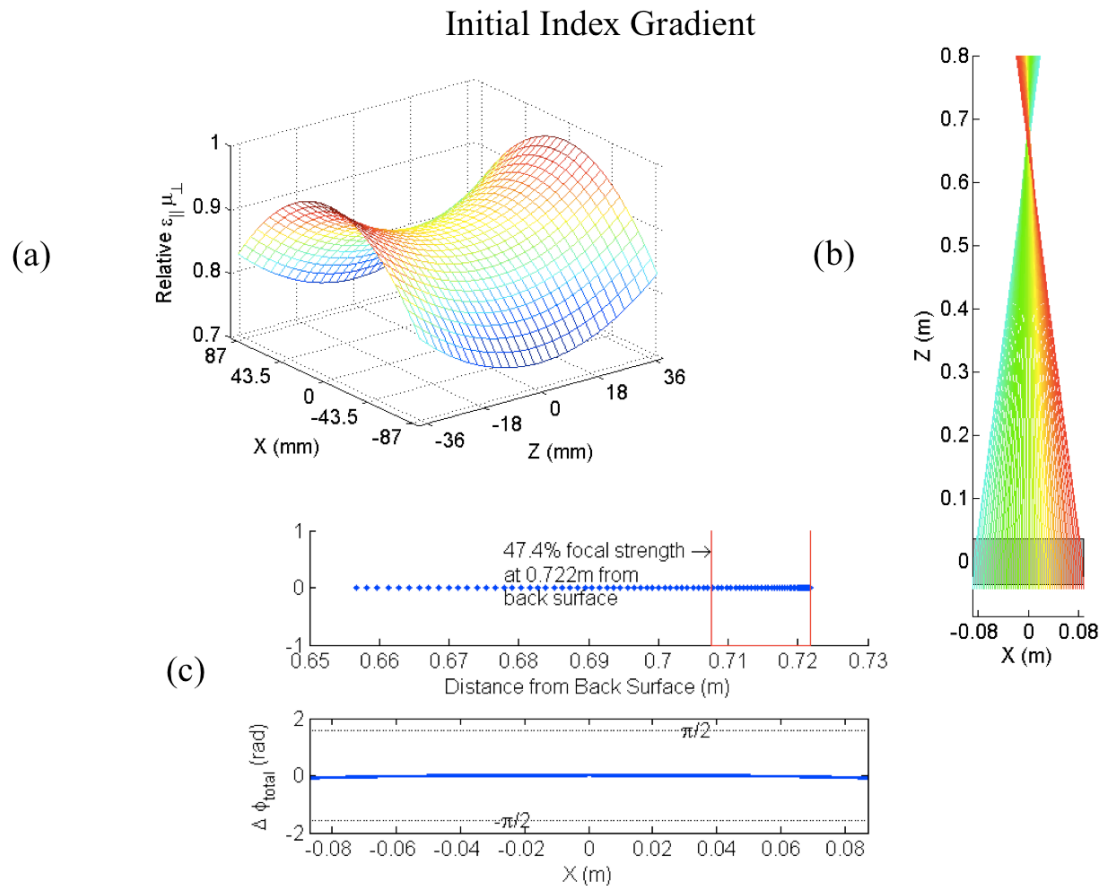
Figure 6.1: Optimized initial gradient profile: (a) gradient surface, (b) ray-trace diagram, and (c) focal strength and location with phase shift.

6.2.2 Relationship between Permittivity and Pitch

One way to determine appropriate pitch values for a specific permittivity is to perform a series of full-wave simulations using Ansoft HFSS. In this section three achiral coil setups in air are investigated with pitch values ranging from 1.5mm to 3.0mm: (1) 5 layers of copper coils in the z-direction, (2) 3 layers of copper coils in the z-direction, and (3) 3 layers of coils in the z-direction with 6mm of air on either z-side of the sample. Master-slave boundaries on the x and y faces create a periodic material. Plane waves polarized with respect to either the y- (parallel) or x-

(normal) directions are sent and received via Floquet ports on the z faces. Permittivity and permeability can be calculated from the scattering, or S, parameters obtained from the ports using a procedure detailed in Ghodgaonkar et al [21]. The theory and results are presented here.

To begin, we assume that the permittivity and permeability of the block of material are complex and that edge effects can be neglected. For S-parameters measured using de-embedded reference planes, i.e. ones not on the surface of the material, we must phase correct for the additional air in the system. The phase shift is related to the length of air on either side of the material and the propagation constant of free space. The corrected values for S_{11} and S_{21}, assuming the same de-embedded length on either side, are calculated using:

$$S_{11} = e^{-2\pi f l} S_{11}^i \tag{6.33}$$

$$S_{21} = \left(e^{-2\pi f l}\right)^2 S_{21}^i \tag{6.34}$$

where f is the frequency, l is the length of air and i indicates the initial S parameter value. These parameters can then be related to the reflection and transmission coefficients through:

$$S_{11} = \frac{\Gamma\left(1-T^2\right)}{1-\Gamma^2 T^2} \tag{6.35}$$

$$S_{21} = \frac{T\left(1-\Gamma^2\right)}{1-\Gamma^2 T^2} \tag{6.36}$$

For a material of length d with characteristic impedance Z and propagation constant γ, the reflection and transmission coefficients are given by:

$$\Gamma = \frac{(Z-1)}{(Z+1)} \tag{6.37}$$

$$T = e^{-\gamma d} \tag{6.38}$$

Both Z and γ depend on the relative permittivity and permeability of the medium:

$$Z = \sqrt{\frac{\varepsilon}{\mu}} \tag{6.39}$$

$$\gamma = \gamma_0 \sqrt{\varepsilon\mu} \tag{6.40}$$

γ_0 is the propagation constant of free space which is equal to $j2\pi/\lambda_0$, where λ_0 is the free space wavelength and $j = \sqrt{-1}$. Using the above, the reflection and transmission coefficients can be rewritten as:

$$\Gamma = K \pm \sqrt{K^2 - 1}, \ K = \frac{S_{11}^2 - S_{21}^2 + 1}{2S_{11}} \tag{6.41}$$

$$T = \frac{S_{11} + S_{21} - \Gamma}{1 - (S_{11} + S_{21})\Gamma} \tag{6.42}$$

The sign for Γ is such that $|\Gamma| < 1$. Using the following relation:

$$\sqrt{\frac{\varepsilon}{\mu}} = \frac{1+\Gamma}{1-\Gamma} \tag{6.43}$$

we can write the permittivity and permeability as functions of γ and Γ:

$$\varepsilon = \frac{\gamma}{\gamma_0}\left(\frac{1-\Gamma}{1+\Gamma}\right) \tag{6.44}$$

$$\mu = \frac{\gamma}{\gamma_0}\left(\frac{1+\Gamma}{1-\Gamma}\right) \tag{6.45}$$

If we set $T = |T|e^{j\varphi}$, the propagation constant becomes:

$$\gamma = \frac{\ln\frac{1}{|T|}}{d} + j\frac{2\pi n - \varphi}{d}, \quad for \ n = 0, \pm 1, \pm 2, \dots \tag{6.46}$$

Since we cannot easily control the permittivity and permeability separately, the material property of interest is $\varepsilon_\parallel \mu_\perp$. With the S-matrices from the HFSS simulations, $\varepsilon_\parallel \mu_\perp$ is calculated for $n=0, \pm 1$, and ± 2. An appropriate curve is selected from the results for each pitch based on

theoretical expectation of the values. The real and imaginary parts are graphed separately, see

Figures 6.2 and 6.3.
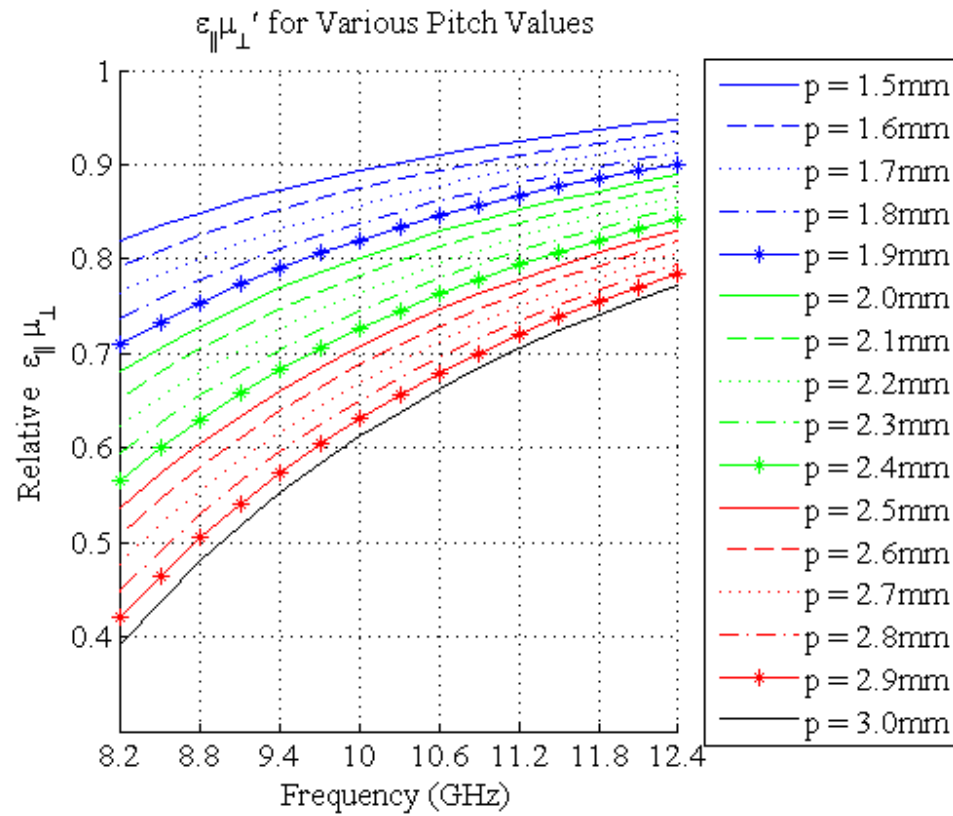
Figure 6.2: Real part of $\varepsilon_\parallel\mu_\perp$ over frequency for various pitch values
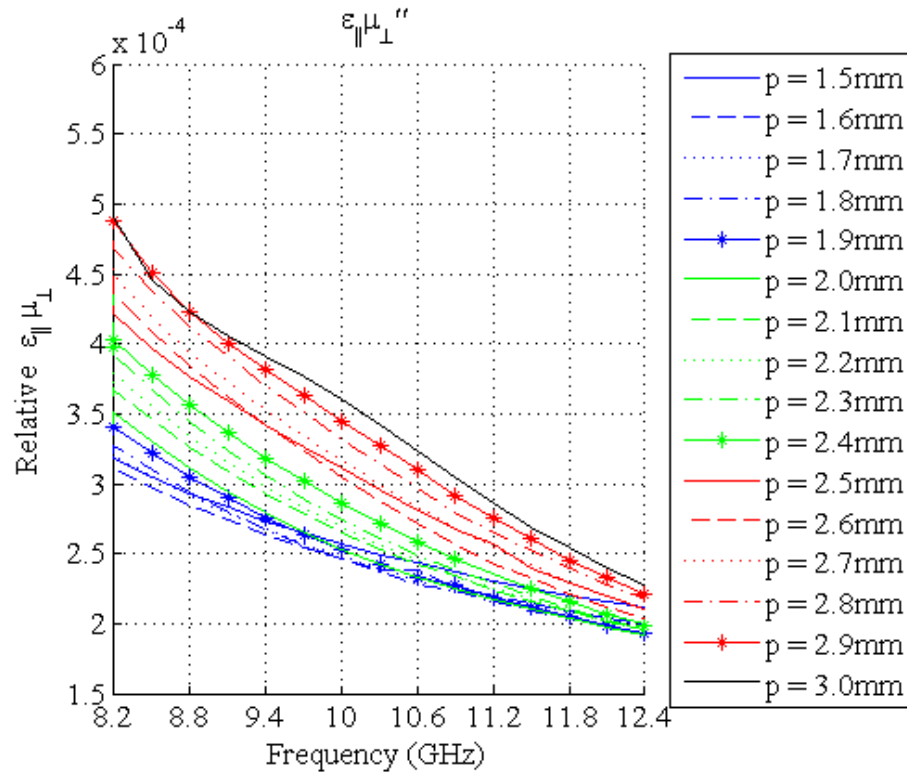
Figure 6.3: Imaginary part of $\varepsilon_\parallel \mu_\perp$ over frequency for various pitch values

Using these results, the gradient index surface plotted in Figure 6.1a was transformed to the gradient pitch surface shown in Figure 6.4.

Initial Pitch Gradient
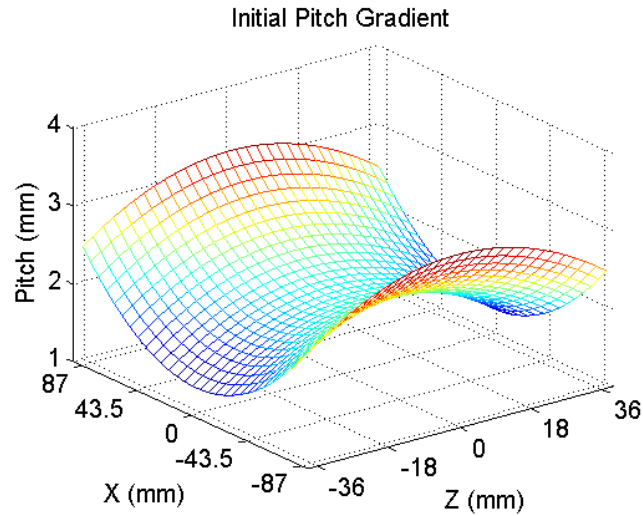
Figure 6.4: Surface plot for pitch gradient transformed from Figure 6.1a using the relationship presented in this section.

Figure 6.5 shows the relationship between $\varepsilon_{\parallel}\mu_{\perp}$ and pitch for three frequencies. This indicates that achieving a focus for multiple frequencies using a coil array is feasible.
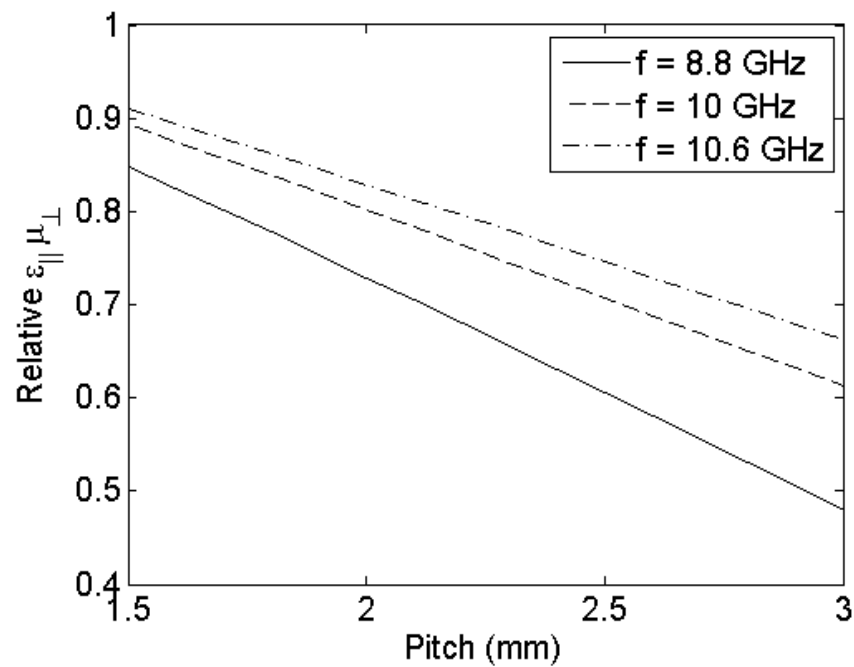
Figure 6.5: Real part of $\varepsilon_{\parallel}\mu_{\perp}$ vs pitch for 3 frequencies

6.2.3   Full-Wave Simulation

Ray-tracing allows for quick determination of the design with optimum focal abilities. However, this type of modeling assumes an ideal-case scenario. A full-wave analysis takes greater computational time, yet more accurately simulates real-world conditions. This provides an effective way to predict the actual behavior of the sample. In this section, we compare two cases corresponding to the measurement setup: frame only (Figure 6.6b) and frame with lens (Figure 6.6c). Each case includes an air box and is periodic in the y-direction. The vertically periodic wooden blocks approximately simulate a wooden frame with or without the lens in place. The size and placement of the simulated frame were limited by the capabilities of the simulating computer. It should be noted that these models neglect the polycarbonate beams present in the fabricated sample, as they are not periodic in the y-direction. Future work could improve the accuracy of the full-wave simulations. The lens consists of 6x6x6mm cubes with spatially-dependent permittivity tensors corresponding to the optimized gradient. Permeability is assumed to be equal to unity. PML boundary conditions are applied to the x- and z- directions to absorb radiation and minimize reflection. The air box is over 2 wavelengths wider than the simulated frame to further minimize reflection. Parallel plane waves incident on one z-face propagate in the z-direction; see Figure 6.6 for model parameters.
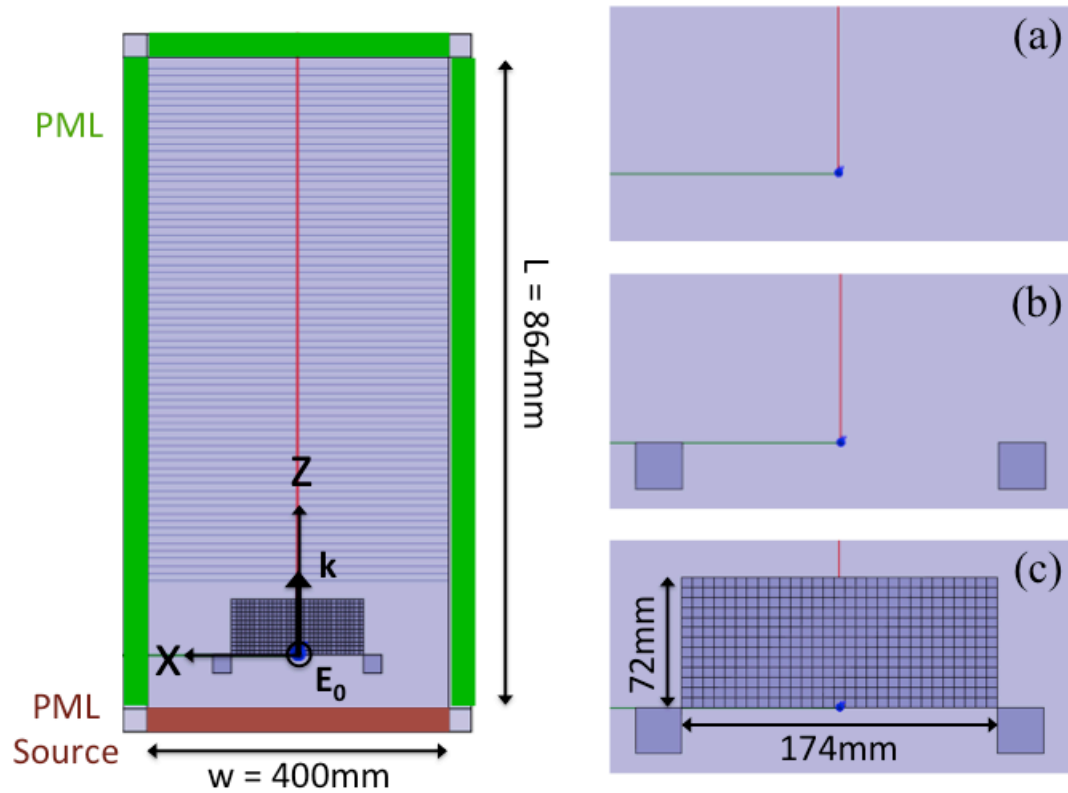
Figure 6.6: Schematic of full-wave simulations showing direction of propagation (k) and orientation of electric field (E_0). Cases are: (a) air, (b) air with frame, and (c) lens in air.

Both the initial and 30% axial strain configurations of the lens are compared to the frame-only case. Transmission results for the initial case are shown in Figure 6.7. When compared to air alone (i.e. free space), the insertion of the lens into the field yields a gain of 8.11dB.
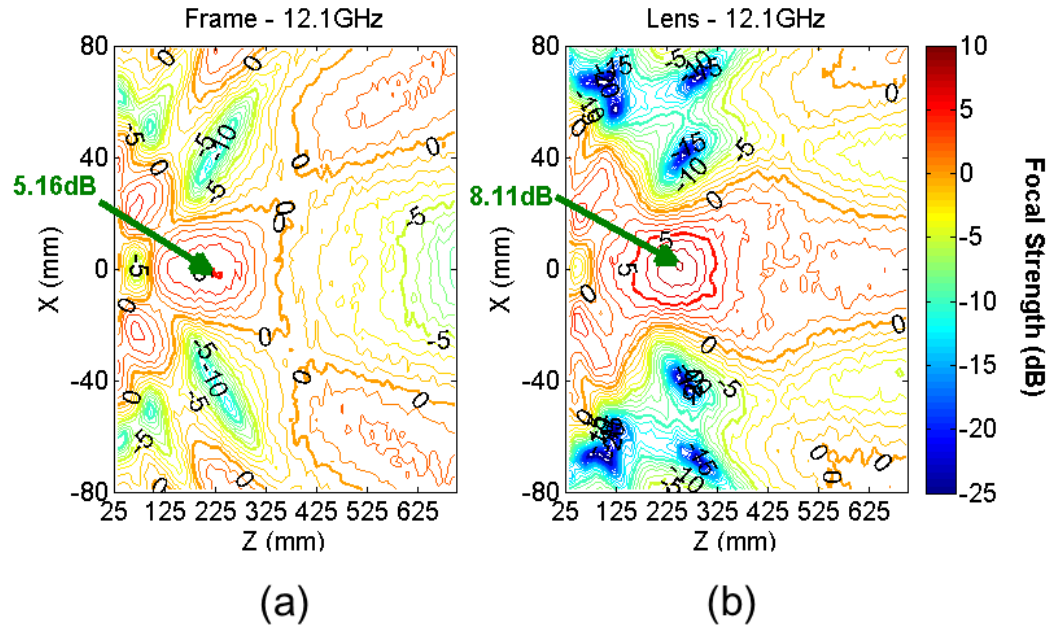
Figure 6.7: Contour plots of the complex magnitude in dB with respect to air for the simulated initial index gradient: (a) air with wood, (b) lens. Contours are spaced 1dB apart and labeled in 5dB steps.

Similar behavior is observed with the 30% axial strain case (Figure 6.8). Though not as sharp as predicted via ray-tracing, these results suggest that the fabricated lens should focus incident microwaves at a closer focal distance than previously estimated.
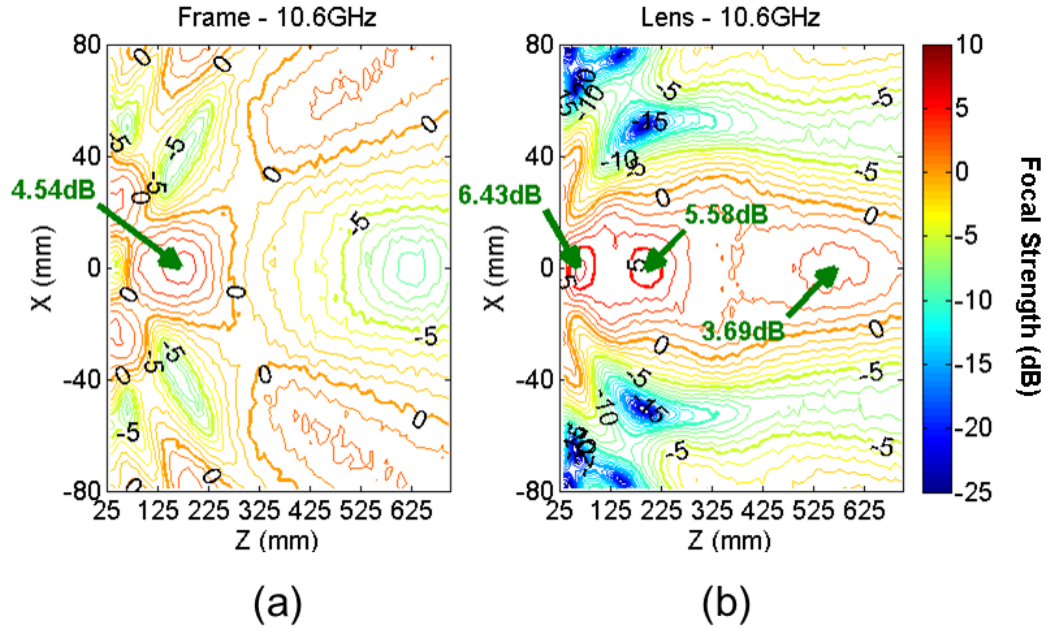
Figure 6.8: Contour plots of the complex magnitude in dB with respect to air for the simulated index gradient at 30% axial strain: (a) air with wood, (b) lens. Contours are spaced 1dB apart and labeled in 5dB steps.

6.3 Experiment

6.3.1 Sample Preparation

The sample used in the EM experiment consists of 13 rows of 29 springs each for a total of 377 springs. Each coil had a wire thickness of 0.525mm, an inner diameter of 3mm, a length of 152.4mm, and a spacing of 6mm. Pitch varied from spring to spring according to location in the array (Equation 6.31).

This gradient was determined from the ray-tracing results optimized for high focal strength and low phase shift. Beryllium-copper was chosen as the material for the springs due to its superior elasticity over plain copper wire. Each coil was wound using an Itasca 100L Programmable Coil Winder to slightly less than the final length, due to size limitations on the

winder and to keep the sample under tension during testing. Coils were wound to achieve the final inner diameter and pitch after the coil relaxed. The ends were then bent to form loops to facilitate mounting in the test frame. The coils were arranged such that handedness alternates across the array, as shown in Figure 6.9.
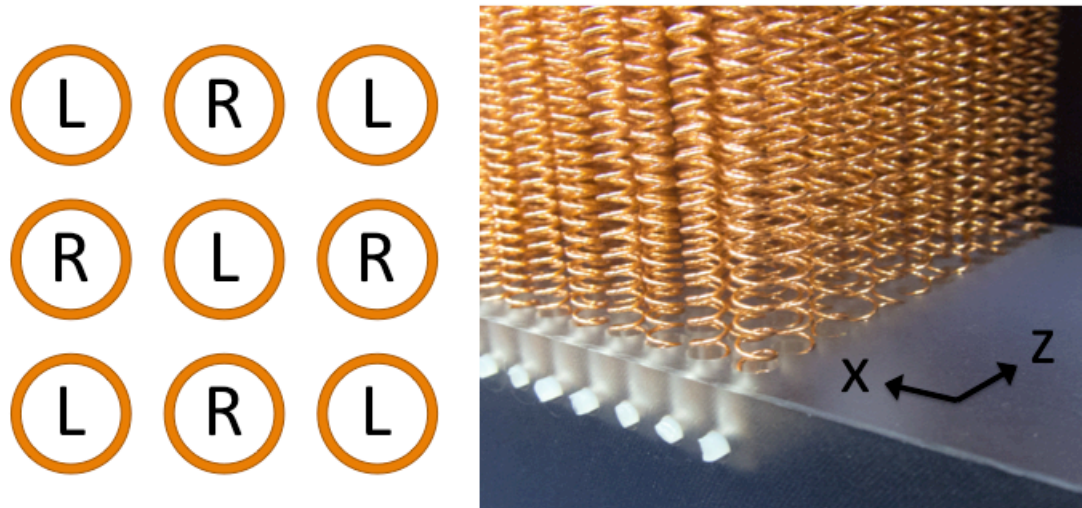
Figure 6.9: Diagram (left) of coil array illustrating arrangement of alternate handedness in sample (right)

With these parameters, the 174x152.4x72mm sample was expected to initially focus incident plane waves at a frequency of 12.1GHz.

6.3.2 Test Frame

Since the springs are extended during testing, they must be mounted in a frame that can survive repeated compressive loads. Metal cannot be used due to its reflective nature. As a result, wood was used to construct the frame surrounding the coils. Each coil was attached to the frame through nylon pins inserted in a polycarbonate base. The top of each coil was attached in a similar manner to a polycarbonate cross-head. This beam raises and lowers with the aid of two threaded

nylon rods and nuts. Additional threaded rod attached to the beam runs along grooves in the frame to maintain planar movement. Polycarbonate was chosen for the supports due to its fracture toughness and superior strength over Plexiglas. The completed lens is shown in Figure 6.10.
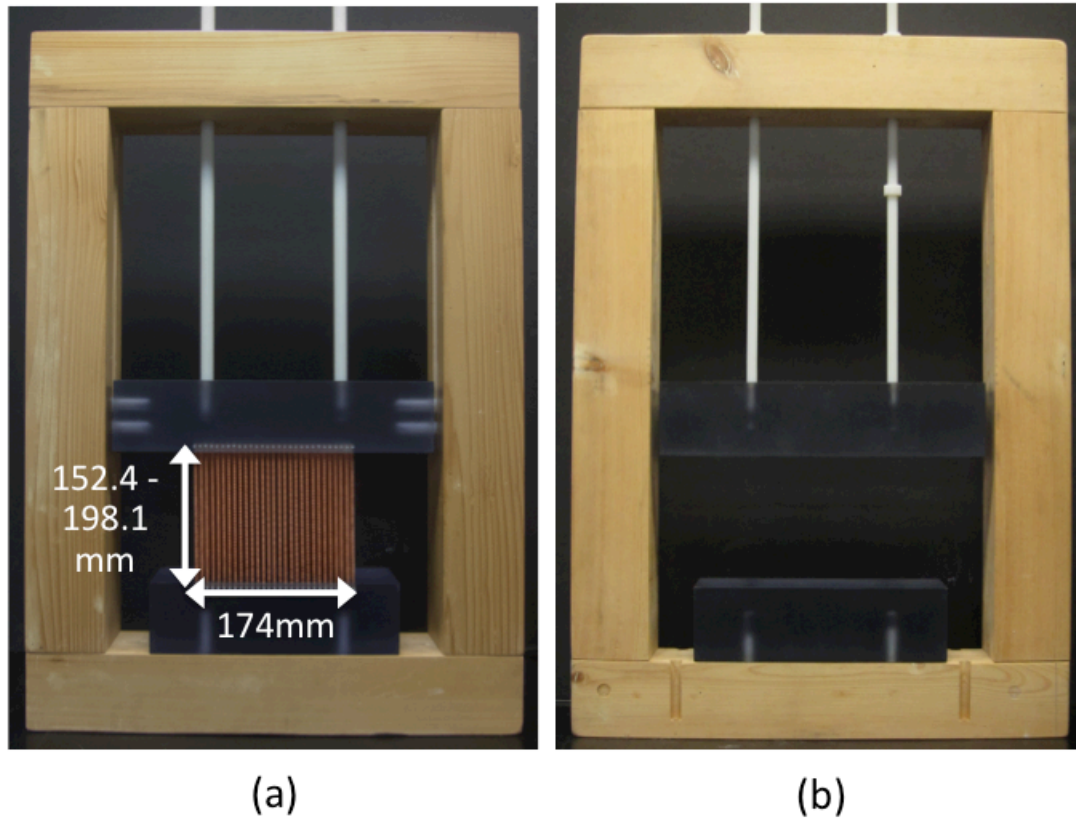
Figure 6.10: Frames used for measurements: (a) with lens, (b) without lens

6.3.3 Test Setup

To approximate a parallel plane wave source, an off-axis reflector was used in conjunction with a horn antenna oriented such that the electric field was polarized parallel to the vertical axis. The dish was positioned close to 1.4m away from the scanned space. A dipole detector placed on an XYZ robot scanned the 160 x 900mm test area in the x- and z-directions,

starting 25mm away from the front surface of the sample. For clarification, the back surface refers to the side facing the reflector; the front surface indicates the side facing the detector. Due to the gradient existing solely in the x- and z-dimensions, very little variation was both expected and observed in the y-direction. Figure 6.11 illustrates the test setup.
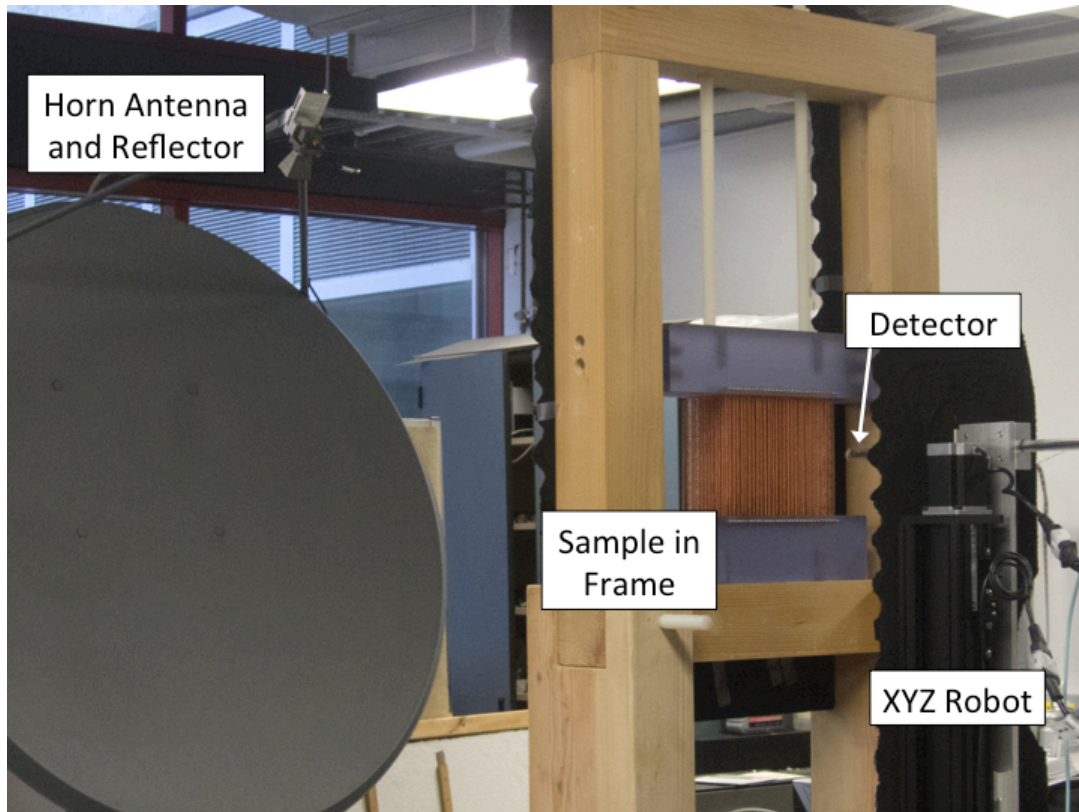
Figure 6.11: Parallel plane wave measurement setup: horn antenna with off-axis reflector and detector

A Python-generated graphic user interface (GUI) controlled the scanning robot and communicated with the Agilent 8510C VNA. Both the source antenna and the detector were connected to the VNA where the signals originated and returned. At each point in the test area, the VNA measured the transmission component of the scattering matrix, S_{21}, over the range of frequency values. The data was then collected into a MATLAB file on the computer via Python.

6.3.4   Experimental Procedure

Each test was performed at an absolute power output of 15dBm with 5% smoothing, which corresponds to a 21-point continuous linear moving average across the frequency band. Two averaging methods were used in a separate set of tests to minimize noise: block linear averaging of 16 readings at each frequency point and 1% (4-point) smoothing. However, the difference between the two sets of data was negligible. The robot scanned the test area with 33 points covering 160mm in the x direction and 91 points covering 900mm in the z-direction over 401 frequency points in the 8.2 to 12.4GHz range. The VNA sent the source signal to the transmitting horn antenna. Through the Python-generated GUI, S_{21} signals received by the detector corresponding to the transmission from port 1 to port 2 were recorded and saved in a MATLAB data file.

Tests were conducted without the frame or lens, then with the frame, then with the frame and lens. Absorbing foam was applied to the back of each frame to minimize reflection in the measurement. Upon completion of a test including the frame, the cross-head on each frame was raised by 6% of its initial length, or 9.14mm. This process continued to a maximum value of 30% axial strain, or a 45.72mm increase, for a total of 6 configurations.

6.4   Results and Discussion

In the results presented in this section, the influence of the lens is seen as normalized gain of the transmitted field with respect to that of a free space measurement, i.e. without lens or frame. A comparison of the simulations and measurements for the initial frame-only and lens configurations (0% axial strain) is shown in Figure 6.12. The measurements generally agree with the full-wave simulations, with slightly less gain observed in the tests. While the frame has an

effect on the transmitted field, the insertion of the lens at 12.1GHz yields a focus of about 6.4dB

over free space around 375mm from the front surface.

Figure 6.12: Contour plots of the gain with respect to free space (no frame) for the initial pitch gradient: (a) frame only simulation and measurement, (b) lens simulation and measurement. Contours are spaced 1dB apart and labeled in 5dB steps.

Similar patterns are observed at the 30% maximum axial strain value achieved in the tests (see Figure 6.13). At 10.6GHz, a maximum focal gain of 8.33dB occurs around 125mm away from the front surface.
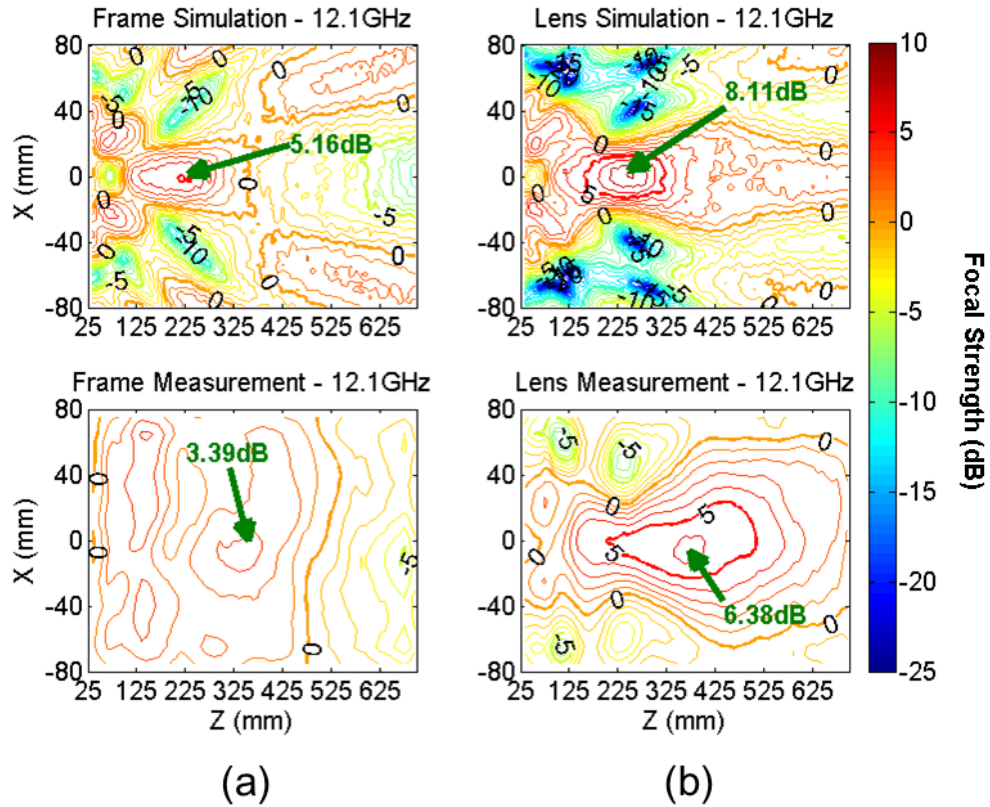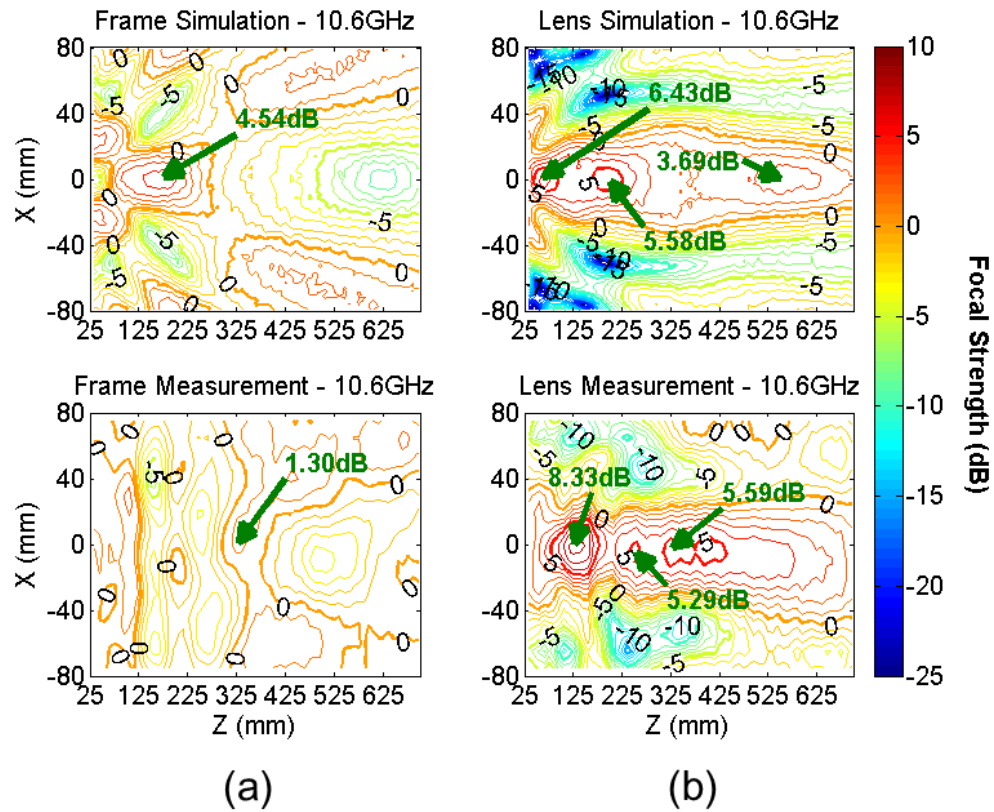

Figure 6.13: Contour plots of the gain with respect to free space (no frame) for the pitch gradient at 30% axial strain: (a) frame-only simulation and measurement, (b) lens simulation and measurement. Contours are spaced 1dB apart and labeled in 5dB steps.

Figure 6.14 displays the focal distance and measured gain with respect to free space over axial strain for three frequencies: 10.1GHz, 10.6GHz, and 12.1GHz. The first frequency corresponds to the maximum focal strength of all stretch values. The second and third correspond to the focal frequencies predicted in the ray-trace analysis. As the coils stretch, focal distance increases; however, focal strength decreases. Multiple focal peaks form at the higher strain positions. This leads to foci closer to the front surface.

Figure 6.14: Measured (a) focal distance, and (b) focal gain with respect to free space (no frame) for each of three frequencies.

Figure 6.15 better illustrates this multiple-peak behavior. At 10.1GHz, the maximum focal gain is around 12.6dB with the initial gradient and around 11.1dB with 30% axial strain. The transmitted gain remains relatively constant. From Figure 6.14, it is clear that the focal distance increases with increasing strain. However, the formation of a second, stronger peak closer to the lens surface causes an apparent decrease in focal distance (Figure 6.15).
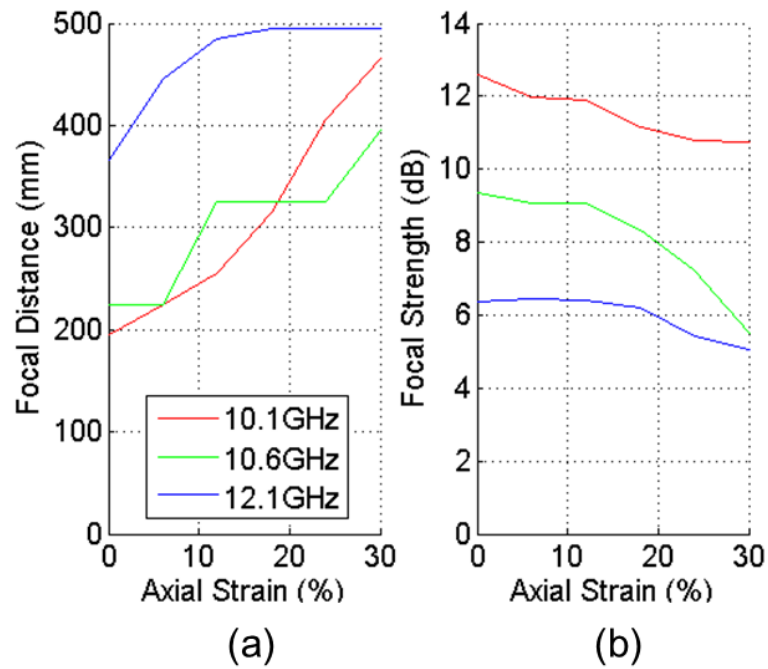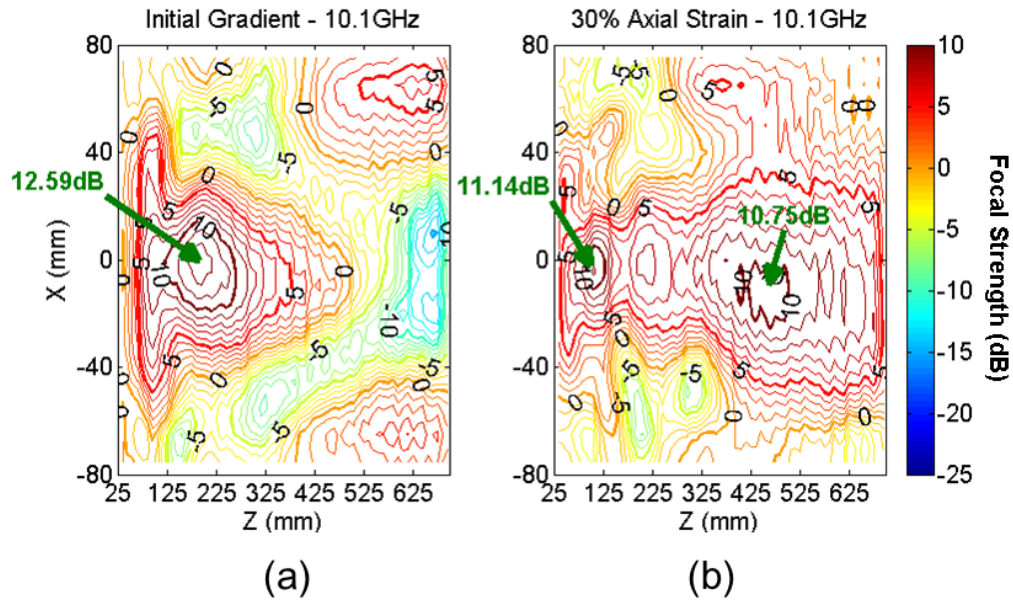

Figure 6.15: Contour plots of gain with respect to free space (no frame) measurement at 10.1GHz for: (a) initial pitch gradient, and (b) pitch gradient at 30% axial strain. Contours are spaced 1dB apart and labeled in 5dB steps.

Using the ray-trace analysis, the initial configuration was designed to focus at 12.1GHz at a distance of 722mm from the front surface of the sample. At 30% axial strain, ray-tracing predicted focusing at 10.6GHz at a distance of 400mm. However, both the full-wave simulation and experimental measurements indicate that the sharpest focusing occurs around the center of the frequency band (10.1GHz) at a distance of less than 225mm. A closer look at the optimized design presented in Section 6.2.1.2 shows that the focal strength increases while frequency and focal distance decrease (see Figure 6.16). Once the material is stretched by 30%, both the focal

strength and focal distance decrease from those of the initial configuration. This confirms the behavior seen in the simulation and measurement.
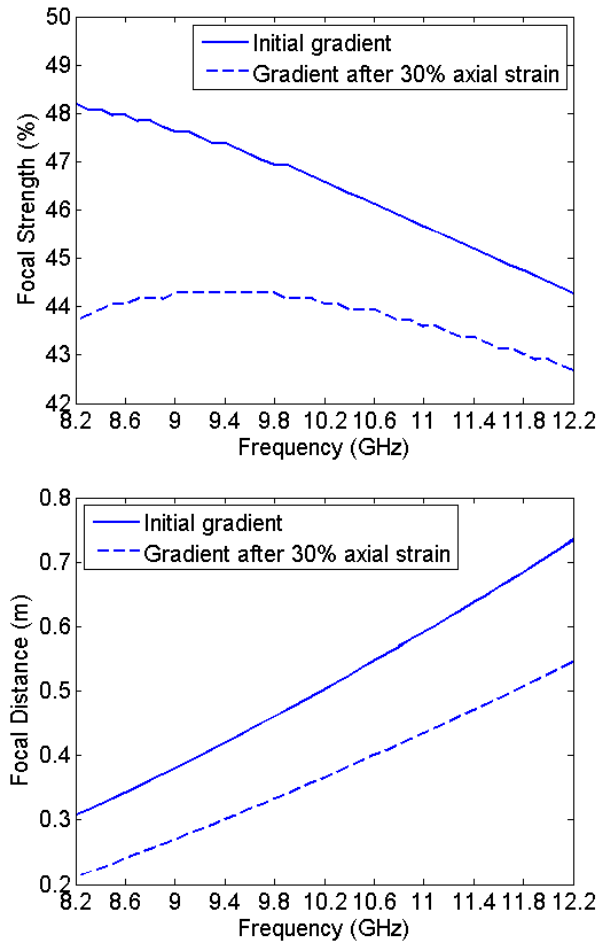
Figure 6.16: Focal strength over frequency (top), and focal distance over frequency (bottom) for the initial and 30% stretched configurations

The quality and strength of the focus, however, differs and the behavior is more complex than predicted with ray-tracing. As mentioned earlier, the ray-trace program represents an ideal case. As such, real world effects including reflections are not considered, which may affect the results. For one, the relationship between pitch and index presented in Section 6.2.2 neglected to take diameter into account as the material stretches. As the pitch increases, the inner diameter decreases. Figure 6.17 shows the relationship between pitch and refractive index as the material

stretches (an increase in pitch in this case indicates axial strain). If we examine this effect (Figure 6.18), we see that the 4% decrease in diameter at 30% axial strain causes an index decrease of nearly 16% at the lower range of the frequency band when compared to the constant diameter case. Though the effect is quite large, the sample was created using the optimized ray-trace values for the initial configuration, which is identical in both cases.
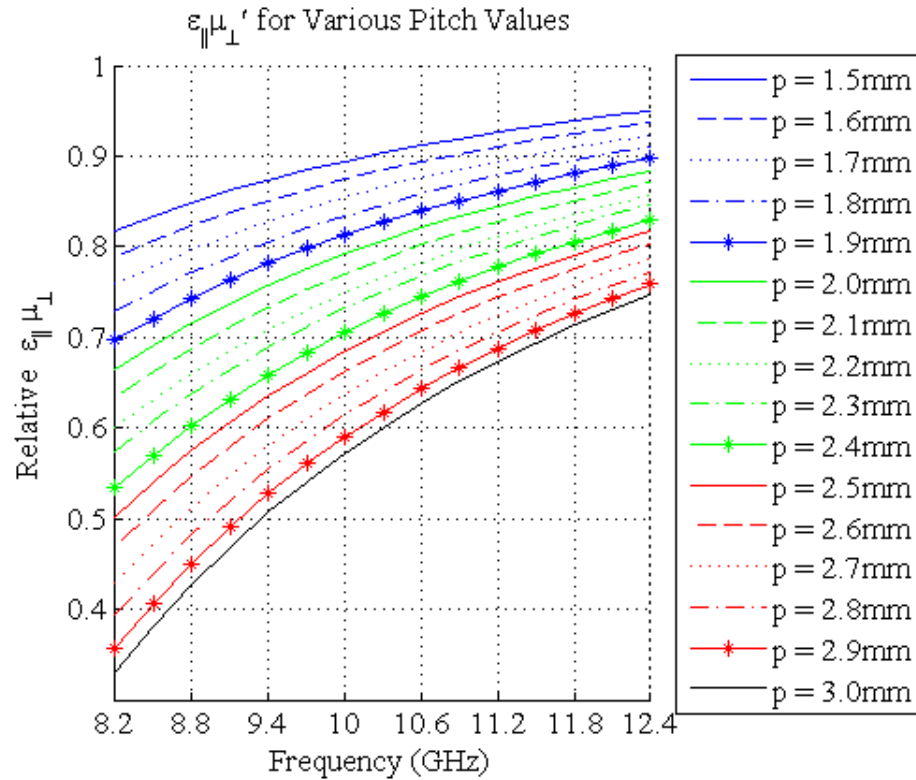

Figure 6.17: Relationship between pitch and refractive index as pitch increases (diameter decreases)
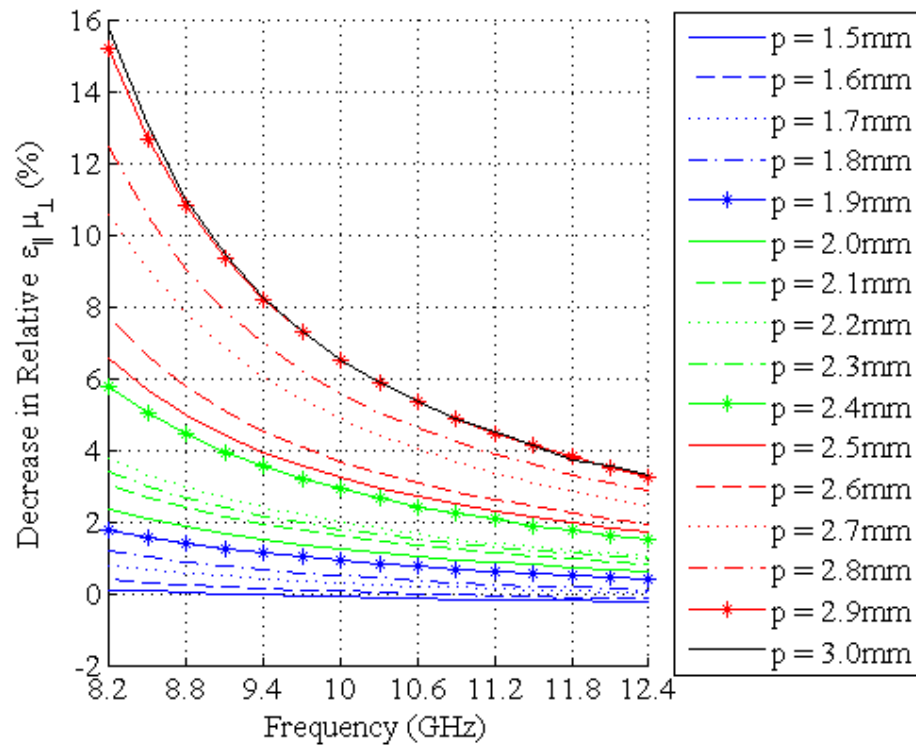
Figure 6.18: Percent decrease in refractive index due to diameter decrease as pitch increases

Other factors may have contributed to the discrepancies between the ray-trace results and those of the simulation and experiment. The ray-trace program assumes a continuous gradient along x and z, while the pitch gradient in the constructed lens is discontinuous due to the discrete number of unit cells. The code also neglects other dielectrics present in lens construction, namely the wooden frame and the polycarbonate. As shown earlier, the frame distorts the field even before the lens in inserted. The incorporation of reflections and additional lens components into the ray-trace program are left for future work.

Differences between full-wave simulation and measurement may also be due to the differences in test frames. The simulation assumed two 25.4x25.4mm vertical wooden blocks whereas the physical test frame consisted of two nearly 100x100mm vertical blocks with two horizontal blocks holding the frame together. Neither polycarbonate nor absorbing foam were

included in the simulation, which could affect the results. There may also be some slight chiral effects from the coils due to the spatial gradient, which are not considered in the simulations.

In order to obtain results closer to the ray-trace performance, the pitch needs to have near 0.0001mm precision. The gradient was limited to the 0.01mm precision allowed by the coil winder, yielding an approximate index gradient. In addition, placement of the coils into the test frame required slight rotations of the loops on each end. This translates to a variation of roughly +/- one-quarter turn from the ideal value. Future work could attempt to minimize these inconsistencies either by individually adjusting each coil in the frame or by introducing varactor diode tuning. With the latter, an individual coil could be tuned to the precise index required in the gradient by varying the voltage across the corresponding varactor.

6.5 Conclusions

An achiral coil array with a mechanically tunable gradient index of refraction was presented for use as a microwave lens. The initial pitch gradient was determined using a Hamiltonian ray-trace analysis. Full-wave simulations indicate a gain of ~8.1dB with the initial pitch gradient at a focal distance of ~250mm. Field measurements taken with a lens composed of copper coils in a wood and polycarbonate frame generally agree with the full-wave results, though they show a lower gain of roughly 6.4dB. Greater precision in sample preparation could improve the focal strength of the lens. Improved insulation from ambient reflections could enhance the measured performance. Extending the gradient to an indefinite medium or embedding this lens in an elastomer may have interesting effects on the performance and are left for future work. The results presented here demonstrate mechanically tunable microwave focusing with a gradient index coil array.

6.6   Acknowledgements

6.7   References

[1] Driscoll, T., Basov, D.N., Starr, A.F., Rye, P.M., Nemat-Nasser, S., Schurig, D., Smith, D.R., "Free-space microwave focusing by a negative-index gradient lens," Applied Physics Letters, 88, 081101, 2006.

[2] Liu, R., Cheng, Q., Chin, J.Y., Mock, J.J., Cui, T.J., Smith, D.R., "Broadband gradient index microwave quasioptical elements based on non-resonant metamaterials," Optics Express, 17 No. 23, 21030-21041, 2009.

[3] Smith D.R., Schurig D., Mock J.J., Kolinko P., Rye P., "Partial focusing of radiation by a slab of indefinite media". Applied Physics Letters. 84 No. 13, 2244-2246, 2004.

[4] Pochiraju, T., Malyuskin, O., Fusco, V., "Tunable near-field subwavelength microwave imaging," Microwave and Optical Technology Letters, 53 No. 6, 1229-1231, 2011.

[5] Lee, J., Lee, K., Park, H., Kang, G., Yu, D.H., Kim, K., "Tunable subwavelength focusing with dispersion-engineered metamaterials in the terahertz regime," Optics Letters, 35 No. 13, 2254-2256, 2010.

[6] Lee, J., Lee, K., Park, H., Kang, G., Yu, D.H., Kim, K., "Tunable subwavelength focusing with slit-groove-based metamaterials in THz," Proceedings of SPIE, 7754, 77541I, 2010.

[7] Neu, J., Krolla, B., Paul, O., Reinhard, B., Beigang, R., Rahm M., "Metamaterial-based gradient index lens with strong focusing in the THz frequency range," Optics Express, 18 No. 26, 27748-27757, 2010.

[8] Wellems, L.D., Huang, D., Leskova, T.A., Maradudin, A.A., "Wavelength-tunable focal length of a nanopatterned metallic planar lens with strong focusing capability," *Proceedings of SPIE,* **7792**, 77920S, 2010.

[9] Lin, H.C., Lin, Y.H., "An electrically tunable focusing liquid crystal lens with a built-in planar polymeric lens," *Applied Physics Letters,* **98,** 083503, 2011.

[10] Cui, Y., Tamma, V.A., Lee, J.B., Park, W., "Mechanically Tunable Negative-Index Photonic Crystal Lens," *IEEE Photonics Journal*, **2** No. 6, 1003-1012, 2010.

[11] Cui, Y., Tamma, V.A., Lee, J.B., Park, W., "Mechanically tunable photonic crystal lens," *Proceedings of SPIE*, **7756,** 77561A, 2010.

[12] Beadie, G., Sandrock, M.L., Wiggins, M.J., Lepkowicz, R.S., Shirk, J.S., Ponting, M., Yang, Y., Kazmierczak, T., Hiltner, A., Baer, E., "Tunable polymer lens," *Optics Express,* **16** No. 16, 11847-11857, 2008.

[13] Schurig, D., Smith, D.R., "Sub-diffraction imaging with compensating bilayers," *New Journal of Physics*, **7** No. 162, 2005.

[14] Fang, A., Koschny, T., Soukoulis, C.M., "Optical anisotropic metamaterials: Negative refraction and focusing," *Physical Review B*, **79**, 245127, 2009.

[15] Wheeland, S., Amirkhizi, A.V., Nemat-Nasser, S., "Soft-focusing in anisotropic indefinite media through hyperbolic dispersion" *Progress in Electromagnetics Research,* **132**, 389-402, 2012.

[16] Ramakrishna, S.A., Pendry, J.B., Schurig, D., Smith, D.R., Schultz, S., "The asymmetric lossy near-perfect lens," *Journal of Modern Optics,* **49** No. 10, 1747-1762, 2002.

[17] Nemat-Nasser, S., Nemat-Nasser, S.C., Plaisted, T., Starr, A., Amirkhizi, A.V., [BIOMIMETICS: Biologically Inspired Technologies], Edited by Yoseph Bar-Cohen, CRC Press, 309-341 (2005).

[18] Schuil, C.J., Amirkhizi, A.V., Bayatpur, F., Nemat-Nasser, S., "Composites with Mechanically Tunable Plasmon Frequency," *Smart Materials and Structures*, **20**, 115012, 2011.

[19] Wheeland, S., Bayatpur, F., Amirkhizi, A.V., Nemat-Nasser, S., "Elastomeric composites with tuned electromagnetic characteristics. *Smart Materials and Structures,* **22,** 015006, 2013.

[20] Sluijter, M., de Boer, D.K.G., Braat, J.J.M., "General polarized ray-tracing method for inhomogeneous uniaxially anisotropic media," *J. Opt. Soc. Am. A*, **25** No. 6, 1260-1273, 2008.

[21] Ghodgaonkar, D.K., Varadan, V.V., Varadan, V.K., "Free-Space Measurement of Complex Permittivity and Complex Permeability of Magnetic Materials at Microwave Frequencies ," *IEEE Transactions on Instrumentation and Measurement*, **39** No. 2, 387-394, 1990.

APPENDIX

Polymer-Helix Mathematica Code

```
uxi = Import["C:\\Users\\Sara\\Desktop\\Non-periodic\\Xdispall.csv", {"Data", 2, {1, 2, 3, 4}}];

xi = Import["C:\\Users\\Sara\\Desktop\\Non-periodic\\Xcoorall.csv", {"Data", 2, {1, 2, 3, 4}}];

uyi = Import["C:\\Users\\Sara\\Desktop\\Non-periodic\\Ydispall.csv", {"Data", 2, {1, 2, 3, 4}}];

yi = Import["C:\\Users\\Sara\\Desktop\\Non-periodic\\Ycoorall.csv", {"Data", 2, {1, 2, 3, 4}}];

uxf = Import["C:\\Users\\Sara\\Desktop\\Non-periodic\\Xdispall.csv", {"Data", 5001, {1, 2, 3, 4}}];

xf = Import["C:\\Users\\Sara\\Desktop\\Non-periodic\\Xcoorall.csv", {"Data", 5001, {1, 2, 3, 4}}];

uyf = Import["C:\\Users\\Sara\\Desktop\\Non-periodic\\Ydispall.csv", {"Data", 5001, {1, 2, 3, 4}}];

yf = Import["C:\\Users\\Sara\\Desktop\\Non-periodic\\Ycoorall.csv", {"Data", 5001, {1, 2, 3, 4}}];

m1 = {{1, 0, -yi[[1]], xi[[1]], yi[[1]], 0}, {0, 1, xi[[1]], 0, xi[[1]], yi[[1]]}, {1, 0, -yi[[2]], xi[[2]], yi[[2]], 0}, {0, 1, xi[[2]], 0, xi[[2]], yi[[2]]}, {1, 0, -yi[[3]], xi[[3]], yi[[3]], 0}, {0, 1, xi[[3]], 0, xi[[3]], yi[[3]]}, {1, 0, -yi[[4]], xi[[4]], yi[[4]], 0}, {0, 1, xi[[4]], 0, xi[[4]], yi[[4]]}};

b1 = {{uxi[[1]]}, {uyi[[1]]}, {uxi[[2]]}, {uyi[[2]]}, {uxi[[3]]}, {uyi[[3]]}, {uxi[[4]]}, {uyi[[4]]}};

MatrixForm[m1]

MatrixForm[b1]

ti = LeastSquares[m1, b1]

m = {{1, 0, -yf[[1]], xf[[1]], yf[[1]], 0}, {0, 1, xf[[1]], 0, xf[[1]], yf[[1]]}, {1, 0, -yf[[2]], xf[[2]], yf[[2]], 0}, {0, 1, xf[[2]], 0, xf[[2]], yf[[2]]}, {1, 0, -yf[[3]], xf[[3]], yf[[3]], 0}, {0, 1, xf[[3]], 0, xf[[3]], yf[[3]]}, {1, 0, -yf[[4]], xf[[4]], yf[[4]], 0}, {0, 1, xf[[4]], 0, xf[[4]], yf[[4]]}};

b = {{uxf[[1]]}, {uyf[[1]]}, {uxf[[2]]}, {uyf[[2]]}, {uxf[[3]]}, {uyf[[3]]}, {uxf[[4]]}, {uyf[[4]]}};

MatrixForm[m]

MatrixForm[b]

tf = LeastSquares[m, b]

Export["C:\\Users\\Sara\\Desktop\\Non-periodic\\solutions.csv", {ti, tf}]
```

GRIN Lens Ray-Trace Code

For a slab of material with $\varepsilon_{\parallel}\mu_{\perp} = \varepsilon_{\parallel}\mu_{\perp c}(1+s_x x^2/a_x^2+s_z z/a_z)$ in which s_x and s_z denote sign, a_x and a_z are constants and $\varepsilon_{\parallel}\mu_{\perp c}$ is the value at the center of the slab, the ray-trace program can be written as:

```matlab
function ddt = equations(t, sol)
    rx = sol(1);
    ry = sol(2);
    rz = sol(3);
    kx = sol(4);
    ky = sol(5);
    kz = sol(6);

    G = [(1/e1)*kx, 0, (1/e1)*kz];

    % Hamilton's Equations, if statement ensures correct dot product
sign
    if dot(G,[kx, 0, kz]) > 0
        ddt = zeros(6,1);
        ddt(1) = (1/(e1*k0))*kx;
        ddt(2) = 0;
        ddt(3) = (1/(e1*k0))*kz;
        ddt(4) = (1/(2*e1*k0))*(alpha*rx);
        ddt(5) = 0;
        ddt(6) = (1/(2*e1*k0))*(beta*rz);
    elseif dot(G,[kx, 0, kz]) < 0
        ddt = zeros(6,1);
        ddt(1) = -(1/(e1*k0))*kx;
        ddt(2) = 0;
        ddt(3) = -(1/(e1*k0))*kz;
        ddt(4) = -(1/(2*e1*k0))*(alpha*rx);
        ddt(5) = 0;
        ddt(6) = -(1/(2*e1*k0))*(beta*rz);
    else
        error('Error with ray - dot product equals zero');
    end

ktx = kix;
ktz = sqrt(e1 - ktx^2);
kt = [ktx,0,ktz];

options = odeset('RelTol',1e-3,'AbsTol',[1e-6 1e-6 1e-6 1e-6 1e-6
1e-6],'Events',@events);
[tau,sol] = ode45(@equations,tau_in,sol0,options);

function [value, isterminal, direction] = events(t,y)
    value = [y(3) + d/2 + 1e-12, y(3) - d/2];
    isterminal = [1, 1];
```

```
        direction = [0, 0];
end

kixf = sol(end,4);
ktxf = kixf;
if abs(ktxf) <= 1
    ktzf = sqrt(1 - ktxf^2);
    ktf = [ktxf, 0, ktzf];
    scale = d*25/ktzf;
else
    ktf = [0, 0, 0];
    scale = 0;
end

start = [x0, y0, -d/2-d/10];
finish = real(sol(end,1:3)) + ktf*scale;

ray = [start; real(sol(:,1:3)); finish];
```